



This is to certify that the

dissertation entitled

An Investigation of the Feasibility of Using $\underline{\text{In}}$ $\underline{\text{Situ}}$ ATR FTIR Spectroscopy in the Measurement of Crystallization Phenomena for Research and Development of Batch Crystallization Processes

presented by

Dilum D. Dunuwila

has been accepted towards fulfillment of the requirements for

Ph.D. degree in <u>Chemical Engineering</u>

Major professor



PLACE IN RETURN BOX to remove this checkout from your record. TO AVOID FINES return on or before date due.

DATE DUE	DATE DUE	DATE DUE
111201		AUG 2 7 2003

MSU is An Affirmative Action/Equal Opportunity institution

AN INVESTIGATION OF THE FEASIBILITY OF USING IN SITU ATR FTIR SPECTROSCOPY IN THE MEASUREMENT OF CRYSTALLIZATION PHENOMENA FOR RESEARCH AND DEVELOPMENT OF BATCH CRYSTALLIZATION PROCESSES.

Вy

Dilum D. Dunuwila

A Dissertation

Submitted to
Michigan State University
in partial fulfillment of the requirements for the degree of

Doctor of Philosophy

Department of Chemical Engineering

1996

AN INVESTIGATION OF THE FEASIBILITY OF USING IN SITU ATR
FTIR SPECTROSCOPY IN THE MEASUREMENT OF
CRYSTALLIZATION PHENOMENA FOR RESEARCH AND
DEVELOPMENT OF BATCH CRYSTALLIZATION PROCESSES.

Bv

Dilum D. Dunuwila

Bulk Crystallization from solution is one of the most widely used unit operations in the food, pharmaceutical and chemical industries. However, a systematic approach to process development and control of crystallization processes has not been presented due to the lack of a technique capable of measuring crystallization phenomena such solubility supersaturation, in situ. ATR FTIR (Attenuated Total Reflection Fourier transform infrared) spectroscopy provides a unique configuration in which the infrared spectrum of a liquid phase can be obtained in a slurry without phase separation. Initially, the feasibility of the technique itself was investigated using a Micro CIRCLE® Open Boat Cell equipped with a ZnSe (zinc selenide) ATR rod. Experiments conducted with aqueous citric acid proved that ATR FTIR spectroscopy can be successfully employed to determine solubility and supersaturation.

Subsequently, establishing the technical feasibility of in situ ATR FTIR spectroscopy for the measurement of crystallization phenomena was

undertaken. The viability of the technique for in situ measurements was investigated using a DIPPER[®] 210 immersion probe manufactured by Axiom Analytical, Inc., of Irvine, California. Initial experiments conducted using aqueous maleic acid proved that ATR FTIR spectroscopy can be successfully employed to measure supersaturation, solubility and the metastable limit, in situ, with sufficient accuracy and precision.

Infrared spectra provide information about the chemical nature and the molecular structure of chemical systems. Changes in molecular structure are reflected in numerous ways in the IR spectrum. Consequently, the full potential of FTIR spectroscopy as a tool to both understand crystallizing systems and measure crystallization parameters was explored. As such the broad scope of *in situ* ATR FTIR spectroscopy in the field of crystallization is demonstrated.

In this investigation, the versatility of in situ ATR FTIR spectroscopy is demonstrated by its applicability in research and development of batch crystallization processes and by its use for the elucidation of molecular structures in supersaturated solutions in aid of understanding crystallization phenomena. However, its potential for implementation in control of crystallization processes, although promising, remains to be proven. A methodology for the development of a control strategy is provided along with other recommendations for further investigations.

To **Savi**

Hydrocortisone crystallization

A practice in sleep deprivation

It tested his grit

But, he now fears to sit

Lest he sleeps through his own presentation

Peter W. Burke
Pharmacia & Upjohn Company (1995)

ACKNOWLEDGMENTS

I would like to thank my advisor, Dr. Kris A. Berglund, for the opportunities, the freedom and the guidance he provided toward my professional growth during my tenure as a graduate student.

I am grateful to my wife, Savi, for her patience and support. I am also grateful to my parents, Mallika and Robert Keerthi, and my sister, Vishani, for all the encouragement I received over the years.

A special acknowledgment is due to my sister-in-law, Shirani Perera, her husband, Dr. Priyantha Perera, and their daughter, Dilshani Perera, for their hospitality and help extended to me during my early years in the United States of America.

Many thanks to my colleagues, Dr. David Gagliardi, Dr. Everson Miranda, Dr. Borlan Pan, Leslie Carroll II, Sanjay Yedur, Marketta Uusi-Penttila, Chris Esswein, Klaus Weisphenig, Yilan Ling, Arvind Mathur, Laurie Ruiz, Dr. Tom Carter, Dr. Beatrice Torgerson, Mark Torgerson and Dr. Hasan Alizadeh, for making my tenure as a graduate student easier in numerous ways.

I would like to thank the members of my dissertation committee, Dr. Kris A. Berglund, Dr. Alec Scranton, Dr. Robert Y. Ofoli, Dr. Stanley Crouch and Dr. Clark Radcliffe for their time and effort. A special word of thanks to Dr. Clark Radcliffe for his participation in this venture.

I acknowledge the financial support from the United States Department of Agriculture and the Crop and Food Bioprocessing Center - Research Excellence Fund at Michigan State University.

Finally, I would like to thank Dr. Mike Doyle, the President of Axiom Analytical. Inc., for his continuing support for this venture.

TABLE OF CONTENTS

LIST OF TABLES	ix
LIST OF FIGURES	x
CHAPTER 1	
INTRODUCTION	1
1.1 Identification and Significance of the Investigation	1
1.2 References	8
CHAPTER 2	
AN INVESTIGATION OF THE APPLICABILITY OF ATR FTIR	
SPECTROSCOPY FOR MEASUREMENT OF SOLUBILITY AND)
SUPERSATURATION IN SLURRIES	10
2.1 Background	10
2.2 Materials and Methods	13
2.2.1 Construction of the Calibration Curves	15
2.2.2 Measurement of Solubility Using Slurries	16
2.3 Results and Discussion	17
2.4 Conclusions	30
2.5 References	31
CHAPTER 3	
AN INVESTIGATION OF THE FEASIBILITY OF ATR FTIR	
SPECTROSCOPY FOR IN SITU MEASUREMENT OF	
CRYSTALLIZATION PHENOMENA	32
3.1 Background	32
3.2 Materials and Methods	33
3.2.1 Measurement of Solubility In Situ	35
3.2.2 Measurement of Supersaturation In Situ	35
3.2.3 Measurement of CSD	35
3.2.4 Construction of the Calibration Curves	36

3.3 Results and Discussion	36
3.3.1 Measurement of Solubility In Situ	38
3.3.2 Measurement of the Metastable Limit In Situ	39
3.3.3 Measurement of Supersaturation In Situ	44
3.3.4 Calibrations	52
3.4 Conclusions	54
3.5 References	55
CHAPTER 4	
IDENTIFICATION OF FTIR SPECTRAL FEATURES	
RELATED TO SOLUTION STRUCTURE FOR UTILIZATION IN	
MEASUREMENT OF CRYSTALLIZATION PHENOMENA	56
4.1 Background	56
4.1.1 Identification of the Vibrations of the Carboxyl Group	58
4.2 Materials and Methods	59
4.2.1 Measurement of Solubility in Slurries	60
4.2.2 Construction of the Calibration Curves	60
4.2.3 Data Processing	60
4.3 Results and Discussion	61
4.4 Conclusions	93
4.5 References	93
CHAPTER 5	
CONTINUING INVESTIGATIONS	95
5.1 Background	95
5.1.1 Control Strategy	95
5.1.2 Solution Structure	110
5.1.3 Effect of impurities	112
5.2 Conclusions	114
5.3 References	114
APPENDIX	116

LIST OF TABLES

Table 2.1	Comparison of experimental solubility measureme	nts of
	citric acid in water to literature values [5]. The give	en
	solubilities are based on % (w/w)	28
Table A1	Data for Figure 2.4	116
Table A2	Data for Figures 2.5 and 2.6	117
Table A3	Data for Figures 2.7 and 2.8	118
Table A4	Data for Figures 3.3 and 3.5	119
Table A5	Data for Figure 3.6	12 0
Table A6	Data for Figure 3.7	121
Table A7	Data for Figure 3.8	122
Table A8	Data for Figure 3.9	123
Table A9	Data for Figure 3.10	124
Table A10.1	Data for Figure 3.11	125
Table A10.2	Data for Figure 3.11	126
Table A10.3	Data for Figure 3.11	127
Table A10.4	Data for Figure 3.11	128
Table A10.5	Data for Figure 3.11	129
Table A10.6	Data for Figure 3.11	130
Table A11	Data for Figure 4.5	131
Table A12	Data for Figure 4.6	132
Table A13	Data for Figure 4.10	133
Table A14	Data for Figure 4.11	134
Table A15	Data for Figure 4.12	135
Table A16	Data for Figure 4.13	136
Table A17	Data for Figure 4.17	137
Table A18	Data for Figure 4.18	138
Table A19	Data for Figure 5.4	139

LIST OF FIGURES

Figure 1.1	Comparison of cooling profiles for batch crystallization. These
	profiles are not specific to any system. They are presented to
	demonstrate the distinction between the three operating
	policies6
Figure 1.2	Projected supersaturation profiles as a consequence of
	applying cooling profile given for batch crystallization7
Figure 2.1	A schematic diagram of the operation of internal reflection
	spectroscopy. Infrared radiation is totally reflected at the
	media interface and is propagated as a transverse wave. The
	evanescent field generated by infrared radiation penetrates
	into the rarer medium in the z -direction as an exponentially
	decaying wave. It is composed of electric vector components in
	all spatial directions. IRE stands for internal reflection
	element [1]11
Figure 2.2	The cross section of the Micro CIRCLE® Open Boat Cell
	(Spectra-Tech) and its optical schematic. ATR stands for
	attenuated total reflection [4]14
Figure 2.3	IR spectra of citric acid in water compared to the IR spectrum
	of water. The arrows indicate the directions of change of the
	spectrum as the concentration of citric acid in water is
	increased. Spectra recorded here were taken at 35 °C.
	Spectra at both 10 °C and 30 °C also followed the same
	trend

Figure 2.4	Calibration of RT_1 . RT_1 is the transmittance ratio of the
	transmission band at 3277 cm ⁻¹ to that at 2610 cm ⁻¹ . The
	solubilities indicated in the figure are literature values [5].
	They were superimposed on the experimental calibrations to
	demonstrate the extension of RT_1 into the supersaturated
	region21
Figure 2.5	Calibration of RT_2 at 10 °C. RT_2 is the transmittance ratio of
	the transmission band at 3277 cm ⁻¹ to that at 1220 cm ⁻¹ . The
	solubility indicated in the figure is the literature value [5]. It
	was superimposed on the experimental calibration to
	demonstrate the extension of RT_2 into the supersaturated
	region
Figure 2.6	Calibration of RT_2 at 30 °C. RT_2 is the transmittance ratio of
	the transmission band at 3277 cm ⁻¹ to that at 1220 cm ⁻¹ . The
	solubility indicated in the figure is the literature value [5]. It
	was superimposed on the experimental calibration to
	demonstrate the extension of RT_2 into the supersaturated
	region23
Figure 2.7	Plot of RT_1 of slurries at equilibrium as a function of
	temperature. RT_1 is the transmittance ratio of the
	transmission band at 3277 cm ⁻¹ to that at 2610 cm ⁻¹ . Each
	data point represents the average of measurements made
	using three different samples25
Figure 2.8	Plot of RT_2 of slurries at equilibrium as a function of
	temperature. RT_2 is the transmittance ratio of the
	transmission band at 3277 cm ⁻¹ to that at 1220 cm ⁻¹ . Each
	data point represents the average of measurements made
	using three different samples 26

Figure 3.1	A schematic of the experimental setup.
	a = spectrometer, b = ATR immersion probe, c = Crystallizer,
	d = Chiller, e = Crystallizer temperature relay,
	f = Product holding tank, g = Temperature controlled bath,
	h = Buchner funnel, I = vacuum34
Figure 3.2	ATR FTIR spectra of aqueous maleic acid as the maleic acid
	concentration (% w/w) was increased (a=50%, b=60%, c=65%
	maleic acid in water). The arrows indicate the direction of peak
	intensity movement with increase in maleic acid concentration.
	The thick arrows indicate the peaks chosen for the
	transmittance ratio, T_R .
	transmittance at 3394 cm ⁻¹
	$T_R = \frac{\text{transmittance at } 3394 \text{ cm}^{-1}}{\text{transmittance at } 1172 \text{ cm}^{-1}}$
Figure 3.3	Solubility of maleic acid with respect to T_R measured in situ, in
	a slurry.
	transmittance at 3394 cm ⁻¹
	$T_R = \frac{\text{transmittance at } 3394 \text{ cm}^{-1}}{\text{transmittance at } 1172 \text{ cm}^{-1}}$ 40
Figure 3.4	Simulated desupersaturation profiles, (a), of cooling batch
	crystallization. The desupersaturation profiles 1, 2 and 3
	correspond to parabolic, linear and natural cooling profiles, (b),
	respectively41
Figure 3.5	The metastable limit of maleic acid, (Y_i) , measured at a cooling
	rate of 1.3 °C/min. and a stirring rate of 420 rpm. The result of
	one experiment is given for illustration purposes. For the given
	experiment, point X denotes the initial conditions and point Y_1
	denotes spontaneous nucleation. All points, Y_i , were extracted
	from similar experiments.
	$T_R = \frac{\text{transmittance at } 3394 \text{ cm}^{-1}}{\text{transmittance at } 1172 \text{ cm}^{-1}}43$
Figure 3.6	Experimental cooling profiles. Profiles 1 and 2 are parabolic
	cooling profiles and profile 3 is a linear cooling profile46

Figure 3.7	The desupersaturation profile corresponding to cooling profile 1
	given in Figure 3.6.
	$T_R = \frac{\text{transmittance at } 3394 \text{ cm}^{-1}}{\text{transmittance at } 1172 \text{ cm}^{-1}}$ 47
Figure 3.8	The desupersaturation profile corresponding to cooling profile 2
9	given in Figure 3.6.
	$T_R = \frac{\text{transmittance at } 3394 \text{ cm}^{-1}}{\text{transmittance at } 1172 \text{ cm}^{-1}}$ 48
Figure 3.9	The desupersaturation profile corresponding to cooling profile 3
	given in Figure 3.6.
	$T_R = \frac{\text{transmittance at } 3394 \text{ cm}^{-1}}{\text{transmittance at } 1172 \text{ cm}^{-1}}49$
Figure 3.10	Mass based product crystal size distributions (CSD). The
	CSDs 1, 2 and 3 correspond to desupersaturation profiles 1, 2
	and 3, respectively. The arrows indicate the mass based
	average sizes of each size distribution51
Figure 3.11	Calibrations of the transmittance ratio, T_R , with respect to
	temperature and maleic acid concentration (% w/w maleic acid
	in water). The constant concentration lines were extracted
	from the given experimental data.
	$T_R = \frac{\text{transmittance at } 3394 \text{ cm}^{-1}}{\text{transmittance at } 1172 \text{ cm}^{-1}}$
Figure 4.1	Self association of carboxylic acids via H-bonding57
Figure 4.2	First, second, third and fourth derivatives of a Gaussian
	peak63
Figure 4.3	In situ, slurry ATR FTIR spectra of aqueous maleic acid at
	saturation in the low frequency region64

Figure 4.4	First derivative profiles of the $\nu(C=O)$ vibrational mode from
	Figure 4.3. BL1=0.005 and BL2=-0.012 were the baselines
	used for PIR_1 and PIR_2 , respectively.
	$PIR_1 = (DA \text{ at } 1740 \text{ cm}^{-1} - a)/(DA \text{ at } 1720 \text{ cm}^{-1} - a)$
	PIR_2 =(DA at 1740 cm ⁻¹ + b)/(DA at 1692 cm ⁻¹ + b)
	a=0.005 and $b=0.012$ are the baseline adjustments,
	DA=derivative absorbance66
Figure 4.5	Solubility and concentration lines of maleic acid with respect to
	PIR_1 measured in situ. In addition, solubility was measured in
	a slurry.
	$PIR_1 = (DA \text{ at } 1740 \text{ cm}^{-1} - a)/(DA \text{ at } 1720 \text{ cm}^{-1} - a)$
	DA=derivative absorbance
	a=0.005 is the baseline adjustment67
Figure 4.6	Solubility and concentration lines of maleic acid with respect to
	PIR_2 measured in situ. In addition, solubility was measured in
	a slurry.
	$PIR_2 = (DA \text{ at } 1740 \text{ cm}^{-1} + b)/(DA \text{ at } 1692 \text{ cm}^{-1} + b)$
	DA=derivative absorbance
	b=0.012 is the baseline adjustment69
Figure 4.7	Isolated second derivative profiles of the v(C=O) vibrational
	mode of aqueous maleic acid at saturation71
Figure 4.8	First derivative profiles of the $\delta(O-H)$ in-plane deformation
	vibrational mode from Figure 4.373
Figure 4.9	Bond distances and angles for the maleic acid molecule.
	Bond distances are given in Å and the angles are italicized for
	clarity74
Figure 4.10	Solubility and concentration lines of maleic acid measured with
	respect to the peak shift of the $v(C=O)$ vibrational mode, in
	situ. In addition, solubility was measured in a slurry. Absolute
	peak positions at two conditions are shown for reference
	purposes

Figure 4.11	Solubility and concentration lines of maleic acid measured with
	respect to the peak shift of the $v(C-O)$ vibrational mode, in situ
	In addition, solubility was measured in a slurry. Absolute peak
	positions at two conditions are shown for reference
	purposes
Figure 4.12	Solubility and concentration lines of maleic acid measured with
	respect to the peak shift of the $v(C=C)$ vibrational mode, in
	situ. In addition, solubility was measured in a slurry. Absolute
	peak positions at two conditions are shown for reference
	purposes79
Figure 4.13	Solubility and concentration lines of maleic acid measured with
	respect to the peak shift of the $\delta(\text{O-H})$ vibrational mode, in situ
	In addition, solubility was measured in a slurry. Absolute peak
	positions at two conditions are shown for reference
	purposes81
Figure 4.14	In situ, slurry ATR FTIR spectra of aqueous maleic acid at
	saturation in the high frequency region82
Figure 4.15	Gaussian components of the $v(O-H)$ region. Due to the
	closeness of the fit the original spectral profile (normalized and
	baseline corrected spectrum at saturation at 30.75 °C from
	Figure 4.14) and the six component Gaussian function used for
	the fit are superimposed84
Figure 4.16	Peak shift of the component near 3150 cm ⁻¹ from
	Figure 4.1586
Figure 4.17	Solubility and concentration lines of maleic acid measured with
	respect to the peak shift of the v(O-H) vibrational mode, in situ
	In addition, solubility was measured in a slurry87
Figure 4.18	Solubility of maleic acid in water with respect to % maleic acid
	(w/w)91

Figure 5.1	Control policy projected to maximize the mean size of a crystal
	size distribution from a cooling batch crystallization process.
	The policy is based on maintaining a constant supersaturation
	defined by the IR parameters given by $\Delta(P_{IR})$ or $\delta(P_{IR})$.
	$\Delta(P_{IR}) = P_{IR} - P_{IR,sol} \text{ and }$
	$\delta(P_{IR}) = \frac{P_{IR}}{P_{IR,sol}}$
	where P_{IR} is any parameter discussed in Chapters 2, 3 and 4 in
	the context of measurement of supersaturation and solubility
	and $P_{IR,sol}$ is the solubility with respect to P_{IR} 98
Figure 5.2	A simple schematic of a batch crystallizer and the primary
	components of the envisioned control system.
	T_i = Inlet coolant temperature of the jacketed crystallizer,
	T_o = Outlet coolant temperature, w = Coolant flow rate,
	$\Delta(P_{IR})$ = Supersaturation, E = Primary controller,
	B = Heat removal system, D = Secondary controller,
	\dot{H} = Heat flux from the crystallizer measured by
	T_i , T_o and w
Figure 5.3	Block diagrams of the cascade control system. The normalized
	heat removal secondary loop is illustrated in (b) 101
Figure 5.4	A supersaturation profile of aqueous citric acid represented in
	terms of TIR.
	$TIR = \frac{\text{transmittance at } 3284 \text{ cm}^{-1}}{\text{transmittance at } 1190 \text{ cm}^{-1}} \dots 103$

INTRODUCTION

1.1 Identification and Significance of the Investigation

Crystallization from solution is a widely used unit operation in the food, pharmaceutical, and chemical industries. Along with separation and purification, production of a specified crystal size distribution (CSD) is one of the primary goals of a crystallization process. The CSD affects the cost of operation of down-stream units such as filtration equipment and dryers. These are often the limiting steps in chemical manufacturing processes and significant cost reductions can be realized by creating CSDs that have favorable filtration and drying properties. Supersaturation is the driving force for both crystal nucleation and growth and, as such, controls the rate of crystallization and the resulting CSD [1, 2]. Therefore, control of crystallization processes requires in situ measurement and subsequent control of supersaturation. However, a technique that is suitable for in situ measurements has not been fully developed.

In today's competitive environment, there is a need to implement control strategies that provide a quantitative output that can be either used by an operator or implemented in an automatic control scheme. A primary impetus for improved control comes from the pharmaceutical industry wherein nearly all products are crystallized at some point in their production. Pharmaceutical processing is usually done in a batch mode,

which is often more difficult to control than continuous processes primarily because batch processes are nonsteady state operations. Another consideration is batch-to-batch fluctuations, which can cause considerable variation in the crystallization process resulting in final product divergence. Reworking a batch that does not meet specifications incurs additional costs and opens the opportunity for contamination.

Clearly, there is a need for the development of an *in situ* measuring device for the dynamic parameters of crystallization processes. Numerous analytical techniques for the measurement of solubility and supersaturation of solutes in liquids have been proposed [3]. They range from simple residual weight determinations to radioactive tracer methods. The primary difficulty in using conventional analytical techniques (refractometry, interferometry, viscometry, density calibrations, etc.) is the procurement of a sample which truly reflects the dynamic process composition at process conditions. Generally, the separation of the saturated or the supersaturated solution from the crystals is required prior to analysis. Percolation, decantation and filtration are common methods used for this separation. During separation and subsequent transportation and analysis special care must be taken to maintain process conditions, primarily temperature, and to avoid adsorption of solute on any of the sampling and analytical equipment. In addition, the analytical techniques themselves pose some difficulties. For example, in refractometry, changes in the refractive index as a function of temperature and/or composition are small and often occur in the fourth decimal point. Interferometry, on the other hand, poses considerable procedural complexities.

This investigation presents a novel method for the measurement of crystallization phenomena. The proposed technique, which is ATR FTIR (Attenuated Total Reflection Fourier transform infrared) spectroscopy [4], provides a unique sampling configuration in which the infrared spectrum of the liquid phase of a slurry (a mixture composed of a solution saturated or supersaturated with a solute in contact with a dense suspension of the undissolved particles of the solute) can be obtained without phase separation. In ATR FTIR spectroscopy, the spectrum is characteristic of the vibrational structure of the material in intimate contact with the ATR apparatus. With regard to a slurry, the proposed approach is predicated on the assumption that effective contact can be limited to that between the liquid phase of the slurry and the ATR apparatus, thus allowing the spectroscopic investigation of the liquid phase without its separation from the suspended particles. The method has the potential to minimize difficulties encountered in sampling and analysis through in situ measurement. Separation of the solution from the crystals is completely avoided.

Initially, the feasibility of the technique itself was investigated using a Micro CIRCLE[®] Open Boat Cell equipped with a ZnSe (zinc selenide) ATR rod. Experiments conducted with aqueous citric acid proved that ATR FTIR spectroscopy can be successfully employed to determine solubility and supersaturation in slurries. The results are presented in Chapter 2.

Subsequently, establishing the technical feasibility of *in situ* ATR FTIR spectroscopy for the measurement of crystallization phenomena was undertaken. The approach was aimed at exploiting recent developments in

ATR FTIR spectroscopy for in situ measurement of supersaturation for the purposes of analysis and control of crystallization processes. The results of in situ measurement of supersaturation, solubility and the metastable limit of aqueous maleic acid are presented in Chapter 3. In addition, a simple way to extract the transient slurry density is outlined. The ATR apparatus used in this study was the DIPPER® 210 immersion probe manufactured by Axiom Analytical, Inc. of Irvine California, USA.

Infrared spectra provide information about the chemical nature and the molecular structure of chemical systems [5]. Infrared active molecular vibrations absorb infrared radiation, thus generating a characteristic IR spectrum. Reactions, changes in composition, introduction of new species and temperature affect the molecular vibrational structure of a chemical system. These changes are reflected in numerous ways in the IR spectrum. the most prominent being peak intensity changes generally associated with composition [6, 7]. Changes in molecular vibrational structure are manifested in more subtle spectral features such as shifts in peak positions These features, in addition to providing valuable insight to the [8]. organization of solute and solvent molecules in supersaturated solutions, can be extremely useful as a tool for measuring crystallization parameters. This is particularly true with systems that have overlapping IR bands where intensity changes are difficult to isolate.

The discussion in Chapter 4 focuses on methods available to identify and isolate subtle effects of IR spectra toward elucidation of solution structure in supersaturated solutions and toward utilization in measurement of crystallization parameters. Both derivative spectroscopy [9] and deconvolution [9] of overlapping bands were used to isolate IR absorption bands arising from various vibrational modes of maleic acid sensitive to reorganizations in solution structure. Several parameters suitable for measurement of solubility and supersaturation were identified and the results are presented. In addition, some insight to the organization of aqueous maleic acid in supersaturated solutions is provided.

Batch crystallizers operated under natural cooling are known to produce a supersaturation peak at the onset of nucleation leading to high rates of nucleation and excessive fines formation [1, 10]. This phenomenon leads to fouling problems, reduced product yields and problems in downstream product handling and processing that can be extremely detrimental to the productivity of the process. The conventional method for circumventing this phenomenon is to use programmed cooling methods [1, 10, 11, as illustrated in Figure 1.1, where the crystallizing system responds to a programmed cooling profile. The predicted time course of the corresponding supersaturation profiles are given in Figure 1.2 [10]. However, this is an open-loop control method, in that, it does not allow intervention to optimize the output through control of supersaturation, which is the driving force for crystal nucleation and growth. In large scale batch-to-batch industrial variations notwithstanding. processes. supersaturation can undergo random fluctuations due to minor changes in operating conditions. What is desired is a closed-loop control scheme that responds to fluctuations in supersaturation by adjusting the rate of cooling and/or the rate of evaporation to maintain optimal conditions during the operation. ATR FTIR spectroscopy provides an opportunity to investigate

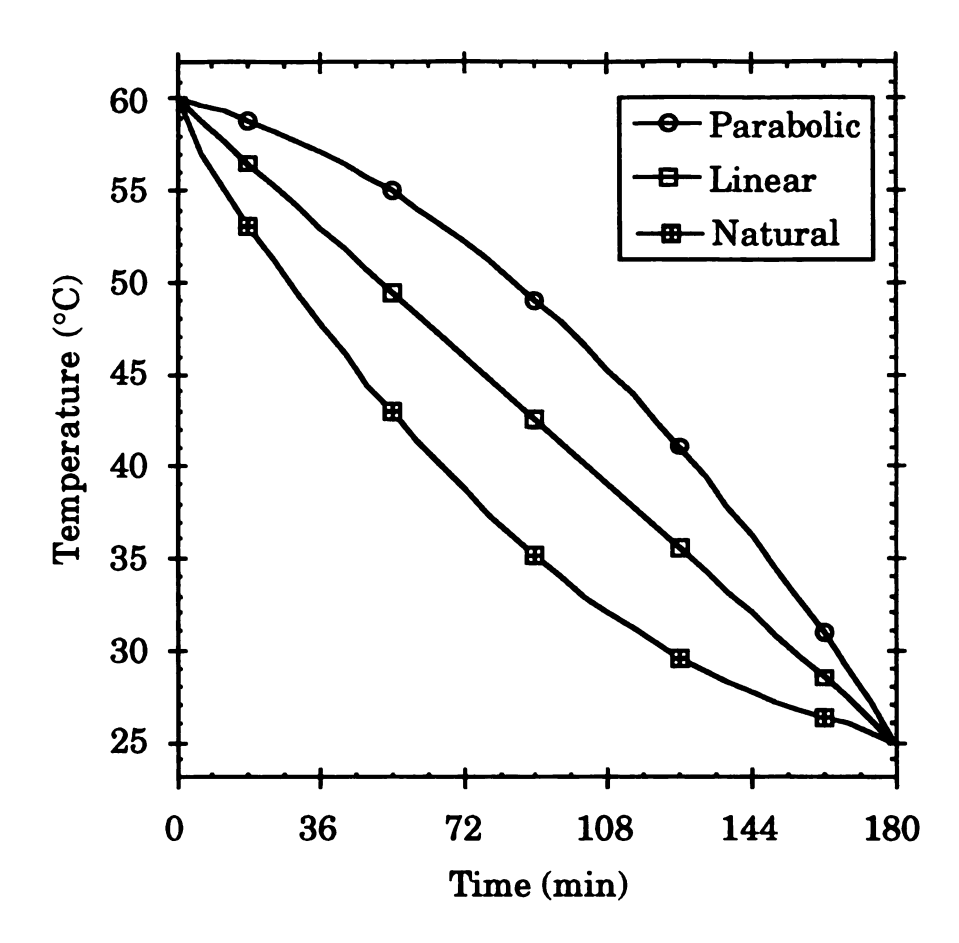


Figure 1.1 Comparison of cooling profiles for batch crystallization. These profiles are not specific to any system. They are presented to demonstrate the distinction between the three operating policies.

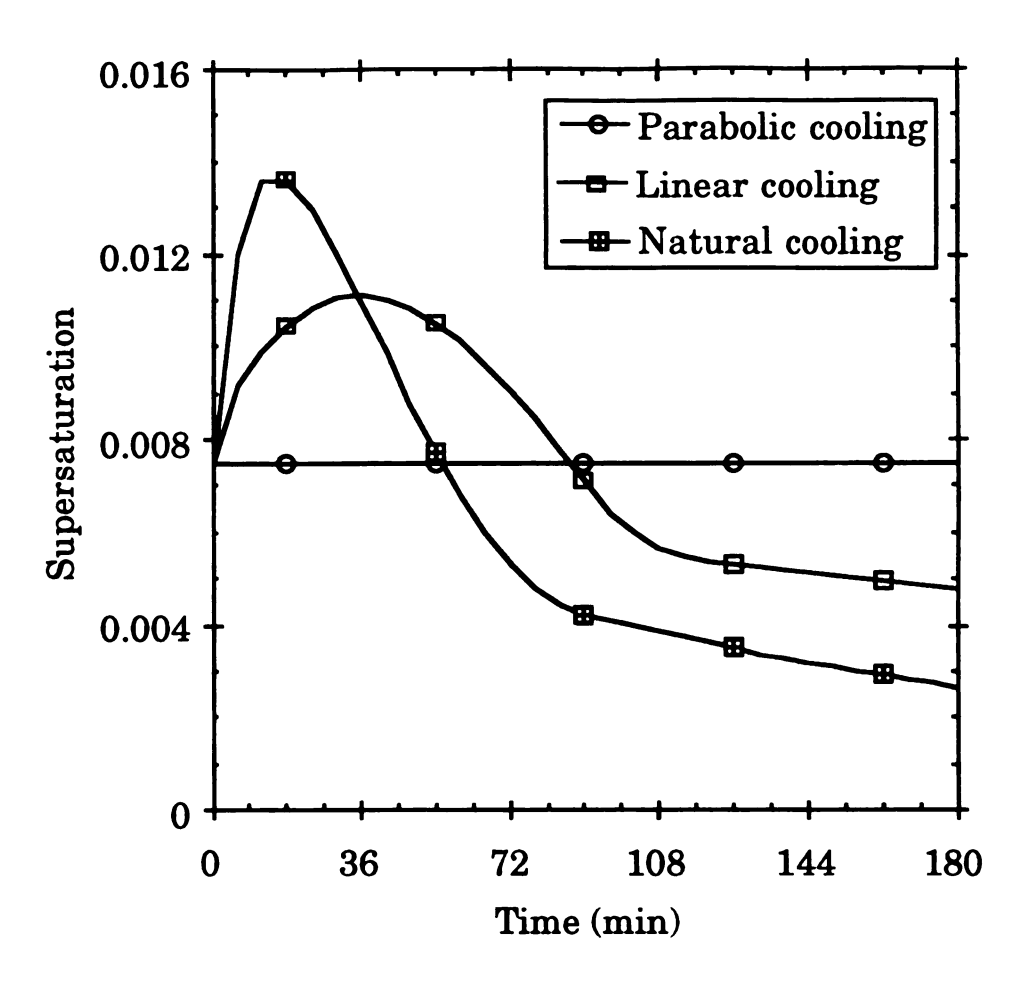


Figure 1.2 Projected supersaturation profiles as a consequence of applying cooling profile given for batch crystallization.

the possibility of using in situ measurement of supersaturation in closed-loop control schemes for industrial crystallizers. An outline for a possible control strategy is presented in Chapter 5.

At this time development of a control strategy for batch crystallization is recommended. The impetus for the focus on batch crystallization is derived from the following considerations; the unsteady state operation of batch crystallizers requires more robust control, current trends in the competitive specialty chemical industry call for the development of batch crystallization and the lack of attention batch crystallization has received in general over time.

The scope of *in situ* ATR FTIR spectroscopy in crystallization is not limited to its use in measurement of crystallization parameters. IR spectra can provide valuable information to deduce the solution structure of supersaturated solutions of various systems. A discussion on this topic is given in Chapter 4 and is continued in Chapter 5. In addition, its potential to study effects of impurities on various systems is discussed.

1.3 References

- 1. Mullin, J. W., "Crystallization", Butterworth-Heinemann, Oxford, England, (1993).
- 2. Randolph, A. D.; Larson, M. A., "Theory of Particulate Processes", Academic Press, New York, USA., (1988).
- 3. Zimmerman, H. K., Chemical Reviews, **51** (1952) 25.
- 4. Mirabella, Jr., F. M., Ed., "Internal Reflection Spectroscopy", Marcel Dekker, Inc., New York, USA., (1993).
- 5. Ingle Jr., J. D., Crouch, S. R., "Spectrochemical Analysis", Prentice Hall, Englewood Cliffs, New Jersey, (1987).

- Dunuwila, D. D., Carroll II, L. B., Berglund, K. A., J. Cryst. Growth,
 137, (1994), 561.
- 7. Dunuwila, D. D., Berglund, K. A., Revised for publication in *Ind. Eng. Chem. Fundamentals*, (1995).
- 8. Avram, M., Mateescu, GH. D., "Infrared Spectroscopy:Applications in Organic Chemistry", Wiley-Interscience, New York, New York, (1966), Ch.7.
- 9. Perkin Elmer IR Data Manager, User's Manual, (1991).
- 10. Jones, A. G., Mullin, J. W., Chem. Eng. Sci., 29, (1974), 105.
- 11. Mullin, J. W., Nyvlt, J., Chem. Eng. Sci., 26, (1971), 369.

AN INVESTIGATION OF THE APPLICABILITY OF ATR FTIR SPECTROSCOPY FOR MEASUREMENT OF SOLUBILITY AND SUPERSATURATION IN SLURRIES

2.1 Background

Attenuated total reflection spectroscopy is based on the presence of an evanescent field in an optically rarer medium (lower refractive index) in contact with an optically denser medium (higher refractive index) within which radiation is propagated due to total internal reflection [1]. Figure 2.1 is a schematic of this phenomenon. The placement of an absorbing optically rarer medium in contact with the denser propagating medium facilitates the interaction between the evanescent field and the absorbing The evanescent wave is a component of the propagating medium. electromagnetic radiation. Electromagnetic radiation conveys information characteristic of matter interacting with its components. This is the basis of most spectroscopic techniques regardless of the mode of operation (transmission, internal reflection, etc.). Consequently, information characteristic of the absorbing medium is conveyed by the propagating radiation. For the current application, propagating infrared radiation generates the characteristic infrared spectrum of the absorbing medium.

Dunuwila, D. D., Carroll II, L.B., Berglund, K. A., J. Cryst. Growth, 137, (1994), 561.

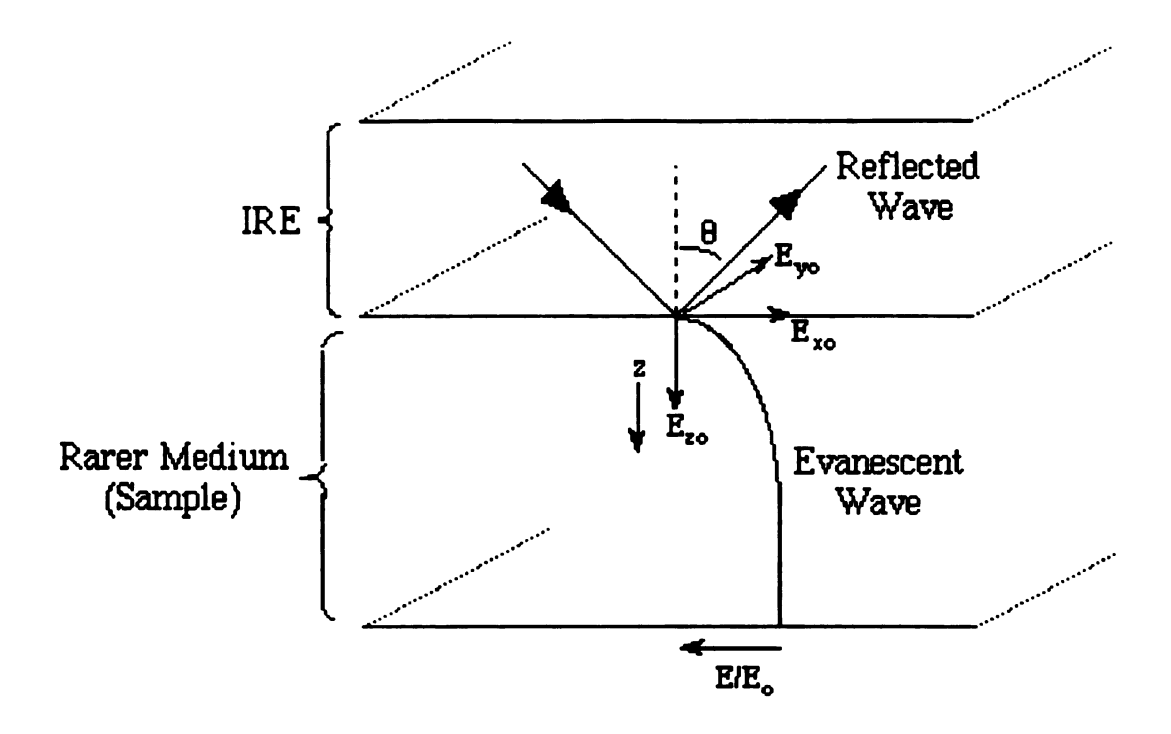


Figure 2.1 A schematic diagram of the operation of internal reflection spectroscopy. Infrared radiation is totally reflected at the media interface and is propagated as a transverse wave. The evanescent field generated by infrared radiation penetrates into the rarer medium in the z-direction as an exponentially decaying wave. It is composed of electric vector components in all spatial directions. IRE stands for internal reflection element [1].

The evanescent field decays exponentially in the z-direction and therefore its effect is confined to the immediate vicinity of the media interface (2-5 μ m). It follows that intimate contact between the medium subjected to analysis and the propagating medium is essential for reliable spectral analysis. The penetration of the exponentially decaying energy field is assessed by a parameter called the depth of penetration (d_p) [2]. The depth of penetration is related to the angle of incidence (θ) of the propagating radiation on the internal reflection element (IRE), the wavelength (λ) and the refractive index of the analyte medium relative to the denser propagating medium (n_{2l}) as follows;

 d_p decreases as θ increases

 $d_{\scriptscriptstyle p}$ decreases as λ decreases

 d_p decreases as n_{21} decreases $(n_{21}<1)$

The extension of this technology for the measurement of crystallization phenomena in slurries was based on the expectation that there will be minimal contact between the crystals of a slurry and the IRE. Minimal contact between the crystals of a slurry and the IRE minimizes the interaction between the crystals and the evanescent field allowing the accumulation of solution phase properties without phase separation with little or no interference from the crystals. It could be postulated that the interaction of the evanescent field is limited to the solution phase that wets the IRE which in turn serves as a minute solution phase barrier that hinders close contact between the crystals and the IRE. In this scenario,

the thickness of the wetting solution phase film is expected to be greater than the depth of penetration of the evanescent field. In addition, d_p can be decreased by manipulating θ , λ and n_{21} . For example, an alternate ATR configuration that has a more favorable angle of incidence can be used. Also spectral analysis can be conducted at lower wavelengths and/or an IRE with a higher refractive index can be utilized.

2.2 Materials and Methods

The applicability of ATR technology toward determination of solubility and supersaturation of solutes in solution using slurries was investigated using a Micro CIRCLE® Open Boat Cell equipped with a ZnSe ATR rod manufactured by Spectra Tech Inc., Stamford, CT, USA. A schematic of the CIRCLE® cell is given in Figure 2.2. This configuration was particularly suited for preliminary experiments due to its open boat construction into which solutions or slurries can easily be dispensed. Temperature control was accomplished using a stainless steel heating jacket designed to specifications that provide best contact between the CIRCLE® cell and the jacket. The heating jacket was incorporated into the structure of the Perkin-Elmer base plate designed specifically for the use of the CIRCLE® cell. The jacket was constructed at the machine shop of the Division of Engineering Research, Michigan State University. The heating jacket was connected to a Lauda Brinkmann Refrigerating Circulator RC6. The infrared spectrometer was a Perkin-Elmer 1750

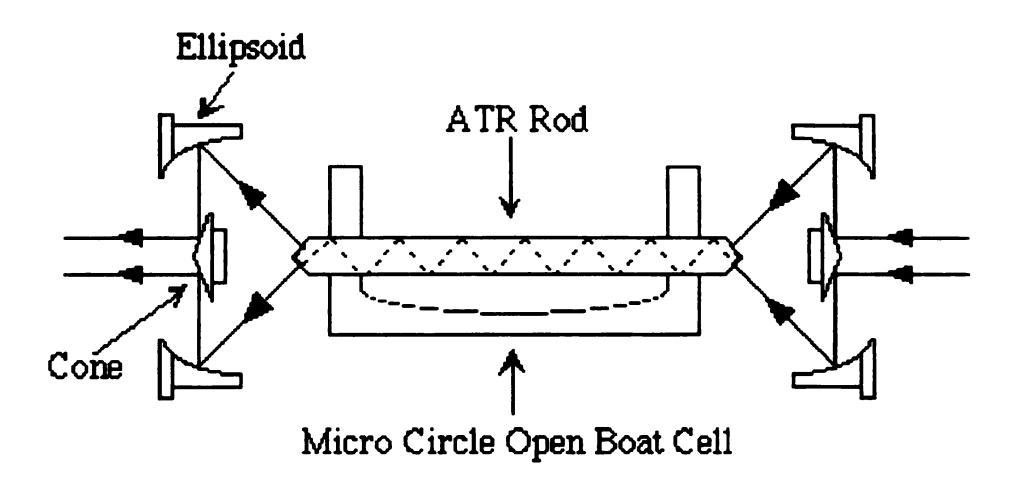


Figure 2.2 The cross section of the Micro CIRCLE® Open Boat Cell (Spectra-Tech) and its optical schematic. ATR stands for attenuated total reflection. [4].

Infrared Fourier Transform Spectrometer connected to a Perkin-Elmer 7700 Professional Computer.

The solute-solvent system of choice was citric acid in water.

Crystalline citric acid monohydrate was obtained from Columbus Chemical

Industries Inc., Columbus, WI, USA..

2.2.1 Construction of the Calibration Curves

Appropriate amounts (weight) of citric acid monohydrate and distilled water were placed in 20 ml Kimble disposable scintillation vials. The mixtures were gently heated with a Master Heat Gun and stirred with a Vortex Genie 2 Mixer, alternately, to homogeneous solutions. The CIRCLE® cell was heated to the set temperature (10 °C and 30 °C) in the heating jacket. The cell and the light transfer optics were aligned to obtain an optimum energy throughput. The spectrum due to the empty cell was scanned and stored as the background. Consequently, the sample spectrum appears free of the background spectral information. The solutions were dispensed into the cell using Pasteur pipettes. Solutions were left standing in the cell for about 10 minutes to allow the solution temperature to equilibrate with the set temperature (jacket temperature). It was noted however, that less than 5 minutes was required for the temperatures to come in to equilibrium. It was also noted that, at thermal equilibrium, for all practical purposes, there was no difference in temperature between the sample contained in the cell and the heating jacket. The temperature within the cell was measured using an Omega OL-703 linear response thermistor probe connected to an Omega Digicator digital readout.

Sample spectra were recorded at the set temperature. The percent transmittance at 3277 cm⁻¹, at 2610 cm⁻¹ and at 1220 cm⁻¹ were recorded over a wide range of citric acid concentrations in water (approximately 0 - 70 % (w/w)). Data were collected at set temperatures 10 °C and 30 °C. Between analysis of different samples the cell was rinsed first with distilled water and then with HPLC grade acetone (obtained from Mallinckrodt Specialty Chemical Co., Paris, KY, USA). The acetone rinse was to facilitate faster drying of the cell in preparation for the next sample analysis.

2.2.2 Measurement of Solubility Using Slurries

A 150 ml batch reactor equipped with a heating jacket connected to the Lauda Brinkmann circulator (same as that connected to CIRCLE® cell heating jacket) was used to prepare slurries of citric acid and water. The slurries were stirred with a Curtin Matheson Scientific 244-793 magnetic stirrer. Slurries at solubility were prepared by dissolving an excess amount of citric acid (an amount exceeding the anticipated solubility at a given temperature) in distilled water, heating the mixture to a homogeneous solution, cooling the solution to the set temperature to facilitate nucleation and stirring for 24 hours to provide sufficient time for growth and equilibration. The temperature settings ranged from 10 °C to 35 °C. The preparation of the FTIR spectrometer and the CIRCLE® cell was identical to the procedure described under the preceding subtitle. The slurries at equilibrium were transported to the cell with a syringe (a 10 ml disposable syringe was cut at the neck to provide a wider aperture that

facilitated easy uptake and disposal of the slurry). Three slurry samples were analyzed at each temperature.

2.3 Results and Discussion

According to the absorption law [3] the absorptance, a, can be written as:

$$a = (1 - T) = 1 - e^{-kb}$$
 (2.1)

where T is the transmittance, k is the absorption coefficient and b is the thickness of the absorbing medium. Note that Equation 2.1 is valid for both absorption at an interface or surface and absorption within a medium. Equation 2.1 can be solved to give;

$$T = e^{-kb} (2.2)$$

In ATR spectroscopy the equivalent expression for the path length, b, for absorption across an IRE interface is given by the product [4];

$$b = Nd_p \tag{2.3}$$

where N is the number of reflection points on the surface in contact with the sample and d_p is the depth of penetration.

A parameter that is often used for quantitative measurements when using spectroscopic techniques for analysis is a ratio between peaks that reflect the relative changes of the system. Peak-ratioing provides an internal standard that can effectively eliminate errors due to imprecise alignment of optical coupling attachments in analyzing subsequent samples. Errors due to instrumental drifts are also minimized. There is evidence to suggest that when peak-ratioing techniques are employed for

analysis, calibrations developed using a particular IRE and a particular angle of incidence of the radiation on the IRE, are equally valid for an alternate IRE and an angle of incidence [1].

Let T_1 be the transmittance of a characteristic infrared transmission band of a solute dissolved in a given solvent. Let T_2 be the transmittance of a characteristic infrared transmission band of the solvent. Equations 2.2 and 2.3 yield;

$$\frac{T_2}{T_1} = e^{Nd_p(k_1 - k_2)} \tag{2.4}$$

where k_1 and k_2 are the absorption coefficients of the solute and solvent bands respectively. The dependence of d_p on wavelength has been neglected for the purpose of demonstration. The relative transmittance, $RT = T_d/T_1$, given by Equation 2.4, predicts an exponential gain in RT as the concentration of the solute is increased (k_1 is proportional to the solute concentration). Therefore, RT is particularly suitable for measurement of crystallization parameters since linear changes in concentration are expressed by exponential gains in RT providing substantial signal gain for the measurement. In addition, a measurement with minimum error is provided by the peak-ratio.

In order to determine the solubility of citric acid in water it was necessary to develop a calibration curve of RT vs. concentration of citric acid in water. The calibration parameters were selected by observing the relative spectral dynamics of the solute/solvent system.

FTIR spectra of aqueous citric acid solutions are given in Figure 2.3.

The decrease in intensity of infrared transmission bands of citric acid

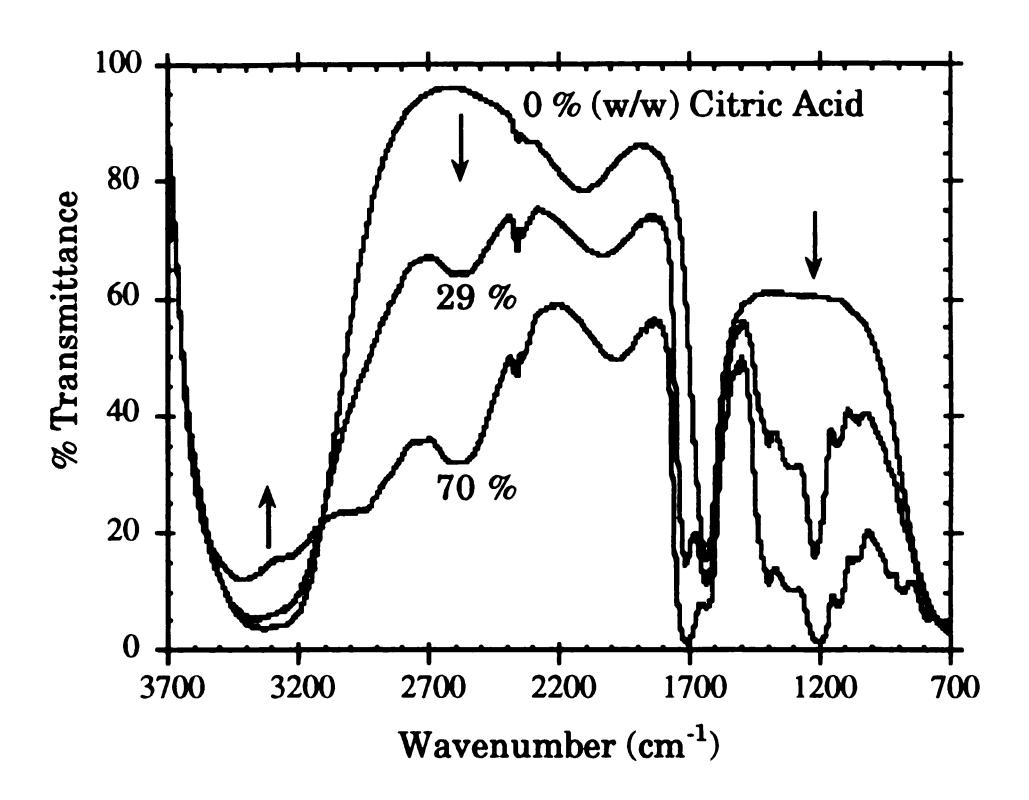


Figure 2.3 IR spectra of citric acid in water compared to the IR spectrum of water. The arrows indicate the directions of change of the spectrum as the concentration of citric acid in water is increased. Spectra recorded here were taken at 35 °C. Spectra at both 10 °C and 30 °C also followed the same trend.

relative to that of water (in the vicinity of 3300 cm⁻¹: OH stretching) is clearly evident. Spectra at 10 °C and at 30 °C resemble those at 35 °C given in Figure 2.3. Using the observed infrared spectra two calibration parameters, RT_1 and RT_2 , were defined;

$$RT_1 = \frac{\text{transmittance of the water band at 3277 cm}^{-1}}{\text{transmittance of the citric acid band at 2610 cm}^{-1}}$$

$$RT_2 = \frac{\text{transmittance of the water band at 3277 cm}^{-1}}{\text{transmittance of the citric acid band at 1220 cm}^{-1}}$$
(2.5)

As previously discussed, the depth of penetration of the evanescent field into the sample is proportional to the wavelength of the radiation. As a result, the possibility exists for the deeper penetrating energy fields at higher wavelengths to interact with the undissolved particles. Therefore, analysis at higher wavelengths could produce erratic data due to spectral contributions from the solid state. To test the consequences of the wavelength dependence of d_p , the calibration parameters given in Equation 2.5 were defined; one at a shorter wavelength, RT_1 , and the other at a longer wavelength, RT_2 .

The plots of RT_1 vs. concentration of citric acid in water are given in Figure 2.4. The temperature dependency of RT is expected due to intermolecular and intramolecular interactions such as hydrogen-bonding. The filled circles in Figure 2.4 represent literature solubilities of citric acid in water [5] and they were incorporated into the figure to illustrate the extension of the calibration curves into the supersaturated region. Figure 2.4 confirms the exponential gain in RT predicted by Equation 2.4.

Plots of RT_2 vs. concentration of citric acid in water are given in Figures 2.5 and 2.6. The two calibrations, at 10 °C and at 30 °C, are not

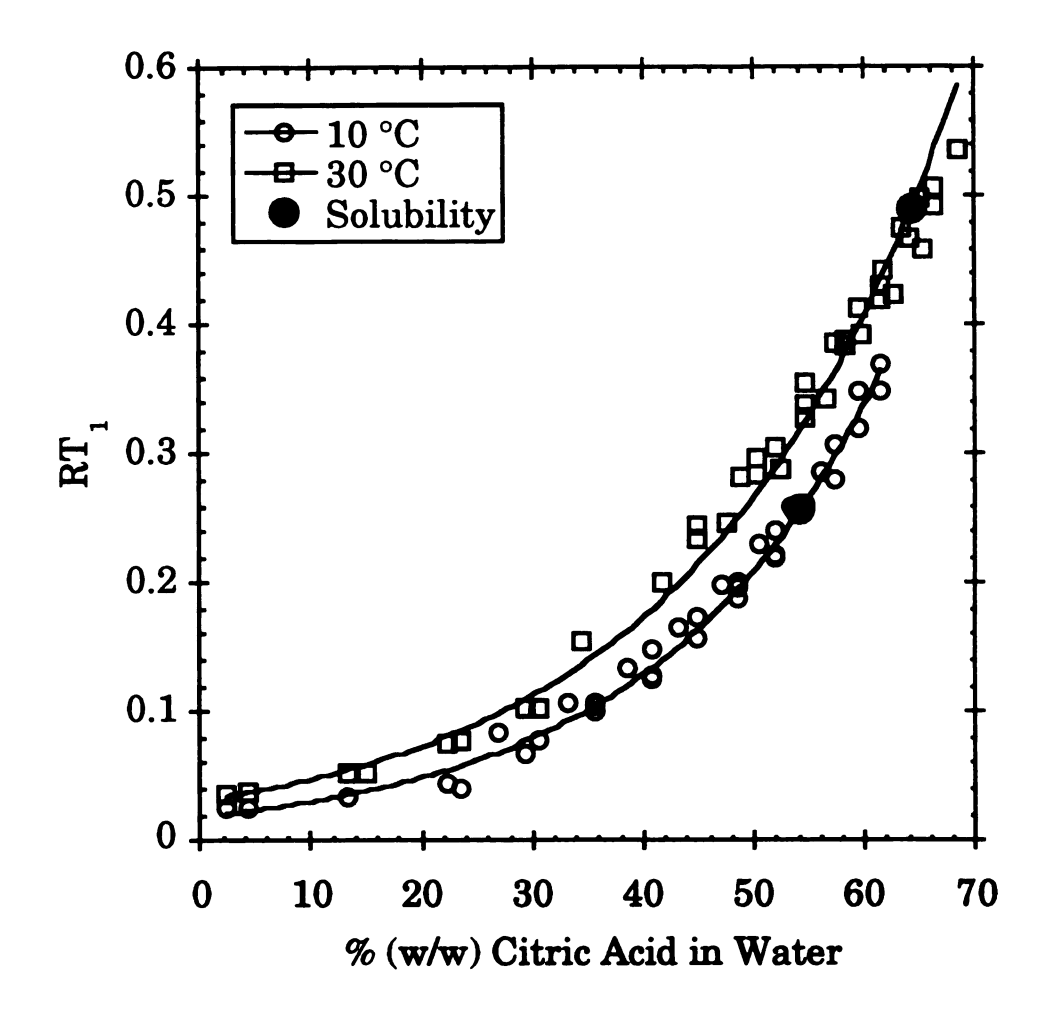


Figure 2.4 Calibration of RT_1 . RT_1 is the transmittance ratio of the transmission band at 3277 cm⁻¹ to that at 2610 cm⁻¹. The solubilities indicated in the figure are literature values [5]. They were superimposed on the experimental calibrations to demonstrate the extension of RT_1 into the supersaturated region.

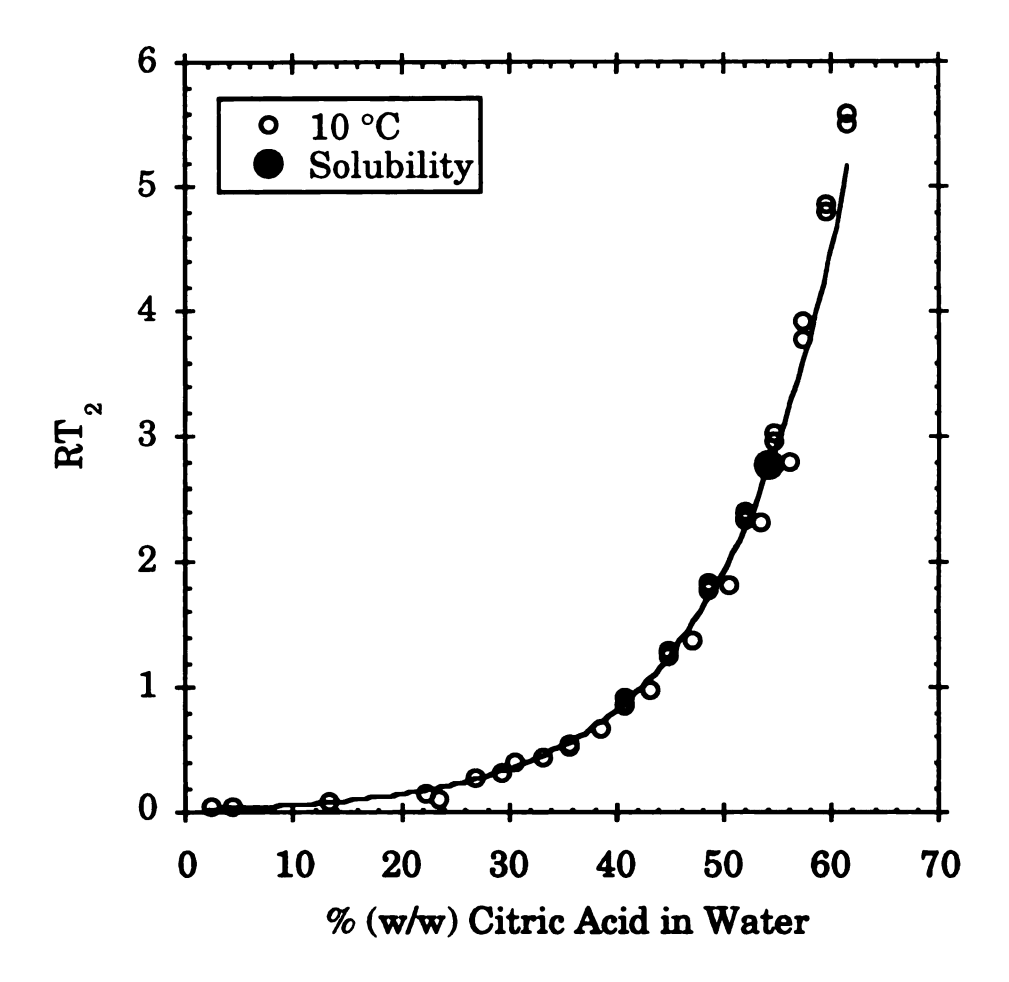


Figure 2.5 Calibration of RT_2 at 10 °C. RT_2 is the transmittance ratio of the transmission band at 3277 cm⁻¹ to that at 1220 cm⁻¹. The solubility indicated in the figure is the literature value [5]. It was superimposed on the experimental calibration to demonstrate the extension of RT_2 into the supersaturated region.

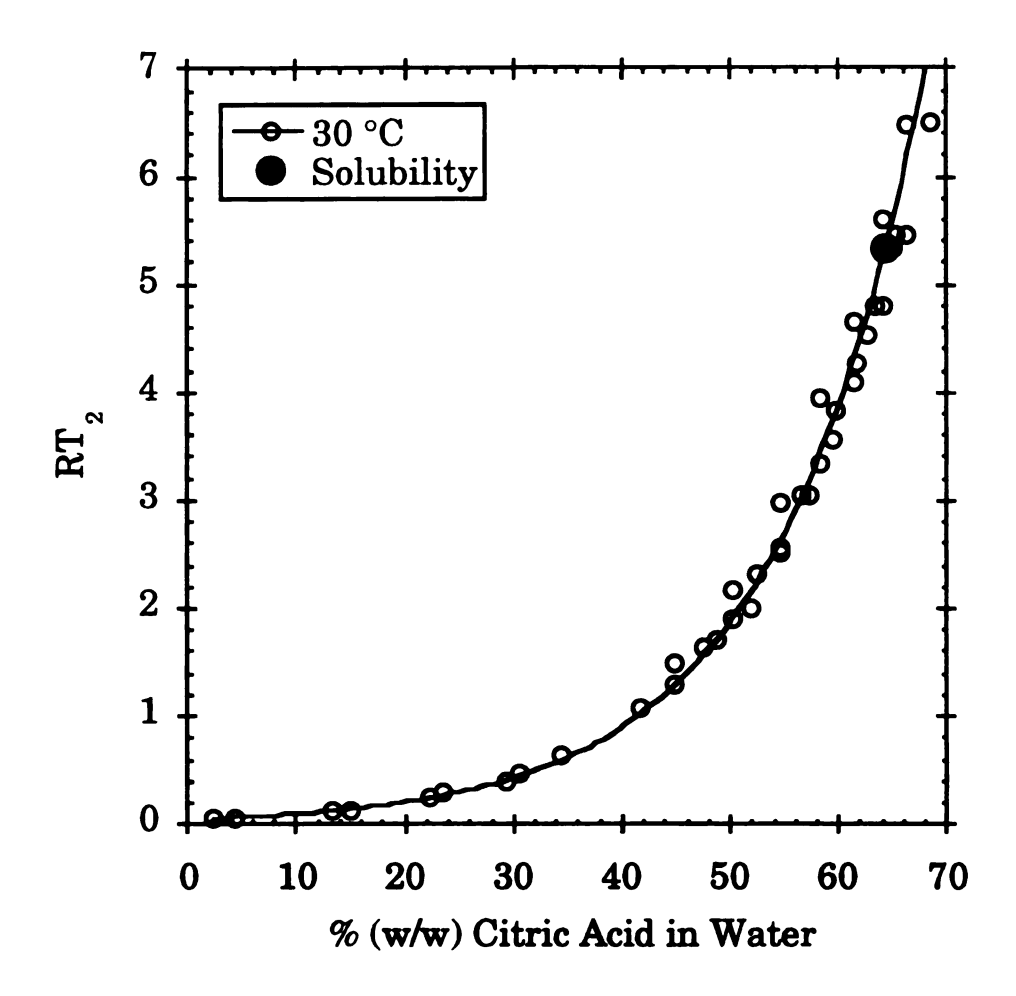


Figure 2.6 Calibration of RT_2 at 30 °C. RT_2 is the transmittance ratio of the transmission band at 3277 cm⁻¹ to that at 1220 cm⁻¹. The solubility indicated in the figure is the literature value [5]. It was superimposed on the experimental calibration to demonstrate the extension of RT_2 into the supersaturated region.

presented in the same figure due to considerable overlap of data. Here too, the data confirms the predicted exponential behavior of RT.

The reproducibility and the consistency of both calibration parameters near and above the solubility of citric acid in water makes them viable candidates for the measurement of solubility and supersaturation. In addition, the exponential gain in RT provides more gain for the measurement of supersaturation than concentration-based approaches.

The traditional solubility and supersaturation measurement techniques (refractometry, interferometry, viscometry, density calibrations, etc.) measure a single calibrated parameter. However, IR spectroscopy, which reflects the vibrational structure of the analyte, can provide more than one piece of information. For example, in addition to solubility or supersaturation, the presence of additives or impurities can be monitored. Reaction dynamics of reactive

crystallization systems can be monitored. The advantage is that necessary information can be obtained simultaneously using the same technique without resorting to multiple techniques that are variable specific. The broader scope of IR spectroscopy in crystallization is taken up in the chapters to follow.

 RT_1 and RT_2 of slurries at equilibrium were plotted against temperature in Figures 2.7 and 2.8, respectively. They are the solubility curves of aqueous citric acid with respect to RTs. The solubility of aqueous citric acid with respect to % w/w at 10 °C and at 30 °C was determined using RT_1 and RT_2 of slurries at equilibrium and the respective calibration

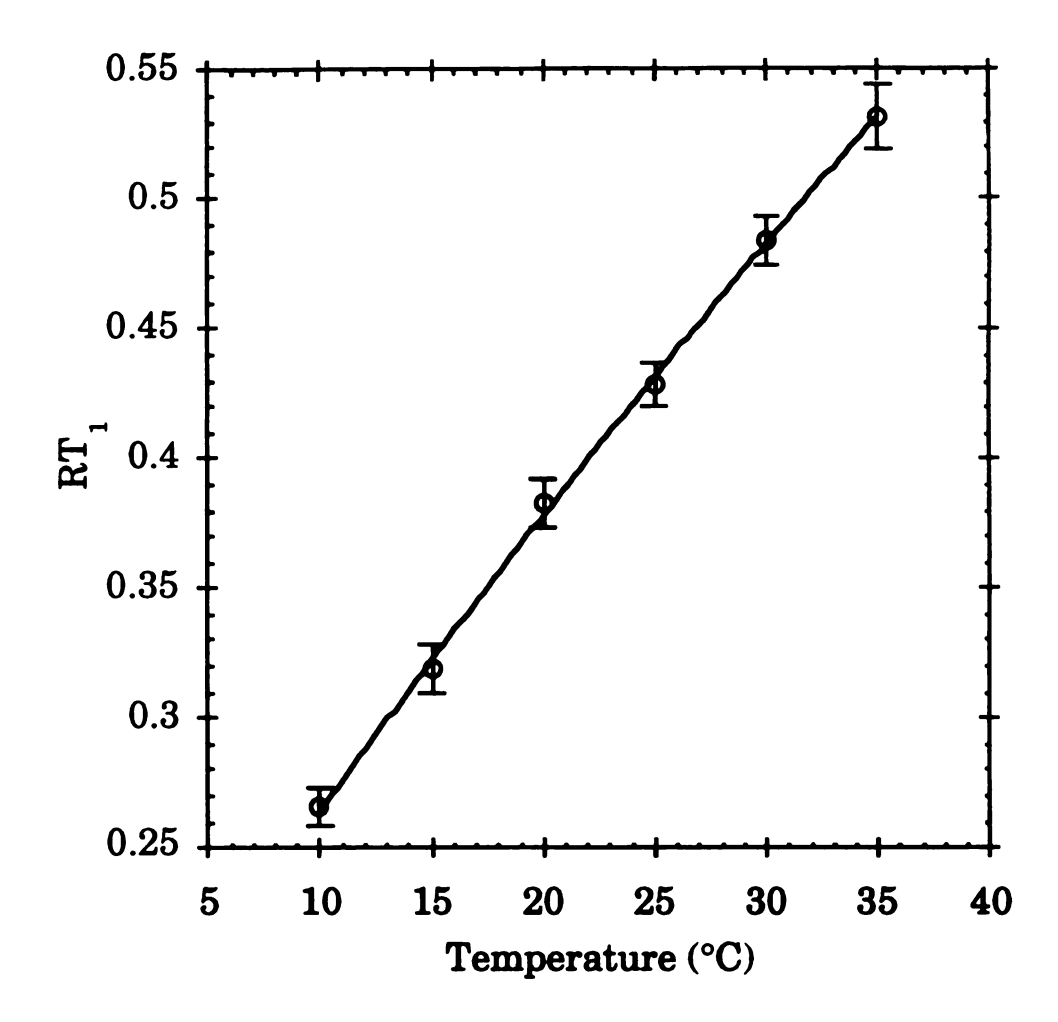


Figure 2.7 Plot of RT_1 of slurries at equilibrium as a function of temperature. RT_1 is the transmittance ratio of the transmission band at 3277 cm⁻¹ to that at 2610 cm⁻¹. Each data point represents the average of measurements made using three different samples.

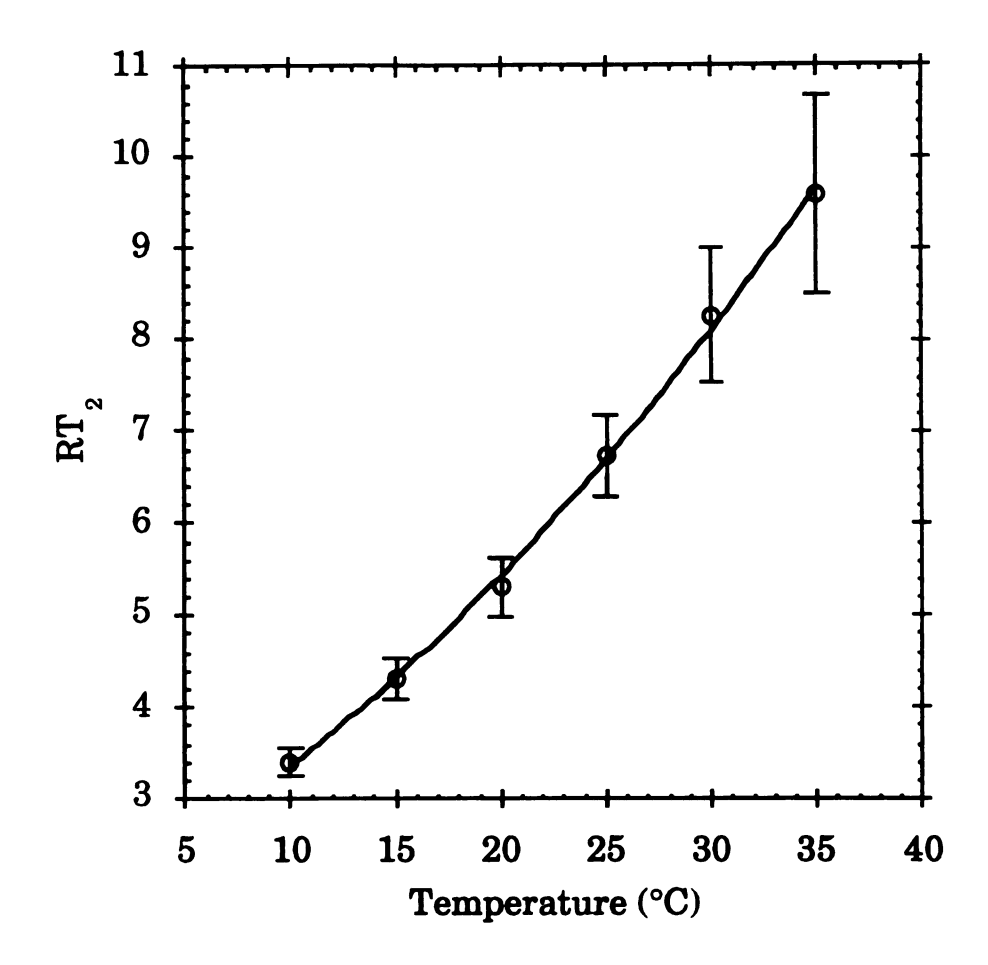


Figure 2.8 Plot of RT_2 of slurries at equilibrium as a function of temperature. RT_2 is the transmittance ratio of the transmission band at 3277 cm⁻¹ to that at 1220 cm⁻¹. Each data point represents the average of measurements made using three different samples.

curves at the respective temperatures. Solubilities thus determined are compared to literature values [5] in Table 2.1.

The percent deviation of the solubility determined using RT_1 from the literature value is relatively small. These deviations are most likely due to inadequate control in experimental procedure rather than due to the analytical technique. Since this investigation, at this stage, was primarily concerned with proving the viability of the concept, precise control of the experiment was not implemented. For example, disturbances due to temperature fluctuations and solute adsorption on the sampling apparatus during sampling of slurries were not controlled. A difference of 1 °C between the reactor temperature and the CIRCLE® cell temperature was observed. For these experiments the digital temperature readout of the Lauda Brinkmann circulator and the digital readout connected to the thermistor probe were not calibrated against a standard thermometer.

Such procedural inadequacies were most likely responsible for the minor deviations in measurement.

The measurement using RT_2 overestimates solubility by 3.7 % at 10 °C and by 10 % at 30 °C. It is apparent from Figure 2.8 that the solubility measured using RT_2 increasingly overestimates the solubility at higher temperatures. As discussed before, RT_2 is a parameter that probes deeper into the slurry compared to RT_1 . It is possible that significant contributions from the crystals of the citric acid slurry to the solution state spectrum could result in an overestimation. However, it is not clear why overestimation is increasingly higher at higher temperatures. Scattering

Table 2.1 Comparison of experimental solubility measurements of citric acid in water to literature values. [5]. The given solubilities are based on % (w/w).

Solubility Measurement Parameter	Temperature (°C)	Experimental Solubility	Solubility Given in the Literature	% Deviation
RT ₁	10	55.8	54.0	+ 3.3
RT_1	30	63.6	64.3	- 1.1
RT_2	10	56.0	54.0	+ 3.7
RT ₂	30	70.7	64.3	+ 10.0

of data is also increasingly higher at higher temperatures. A likely cause is not clear at this moment.

If the deeper penetration of the evanescent field into the sample was in some way responsible for the overestimation of solubility and scattering of data, the employment of a greater angle of incidence for the radiation on the IRE and an IRE with a higher refractive index (Ge and AMTIR-1 ATR elements) could help overcome such problems through the reduction of the depth of penetration. Such parametric manipulations may be absolutely necessary for solute-solvent systems that have transmission bands of utility only at higher wavelengths.

Concentrations of supersaturated solutions of citric acid in slurries were not measured using the CIRCLE® cell. The degree of control in the crude sampling procedure followed in these experiments were deemed inadequate to study the labile supersaturated region. It was a limitation imposed by the procedure and certainly not by the technology. However, in recognition of the feasibility of the technique for the measurement of supersaturation, a few comments follows. Supersaturation, S, is defined by the following equation [6];

$$S = n \ln \left\{ \frac{\gamma C}{\gamma_{eq} C_{eq}} \right\} \tag{2.6}$$

where γ is the activity coefficient, C is the concentration and n is the number of ions in a molecular unit. The subscript "eq" denotes the solute-solution equilibrium. The activity coefficient, γ , reflects nonideality of solutions. Generally, nonideal behavior is due to extensive intermolecular

and intramolecular interactions between the solute and the solvent. These interactions in turn configure the solution structure of the system. Then, it follows that the activity coefficient is reflective of the solution structure at a molecular level. Therefore, a method for determining supersaturation that is reflective of the solution structure would be inherently more accurate. However, due to practical restraints in measuring activities, conventional techniques such as refractometry, interferometry, viscometry and densitometry that measure the respective bulk properties are used along with simplifying assumptions. However, IR spectroscopy, which probes the vibrational and rotational structure of molecules is reflective of the solution structure and therefore is a more viable technique to measure supersaturation that is more reflective of activities. Recently, other solution structure based methods such as fluorescence spectroscopy have been used to measure supersaturation in aqueous systems [7, 8].

2.4 Conclusions

This investigation clearly demonstrates the feasibility of ATR FTIR spectroscopy toward measurement of solubility and supersaturation in slurries. The exponential gain of the defined parameters, RT_1 and RT_2 , with increasing solute concentrations provides increased signal gain for more accurate data analysis. The capability to carry out measurements using slurries certainly eliminates the separation of phases required by other measurement techniques. The feasibility of extending ATR FTIR spectroscopy for *in situ* measurement of crystallization phenomena such as solubility and supersaturation is explored in the following chapter. The

noted inconsistency in solubility measured using RT_1 and RT_2 is addressed in Chapter 4.

2.5 References

- 1. Mirabella, Jr., F. M., in: "Internal Reflection Spectroscopy", Ed. F. M. Mirabella, Jr., Marcel Dekker, Inc., New York, USA., (1993), ch. 2.
- 2. Harrick, N. J., duPre, F. K., Appl. Opt., 5, (1966), 1739.
- 3. Ingle, Jr., J. D., Crouch, S. R., "Spectrochemical Analysis", Prentice Hall, Englewood Cliffs, USA., (1988), ch. 3.
- 4. Coates, J. P., in: "Internal Reflection Spectroscopy", Ed. F. M. Mirabella, Jr., Marcel Dekker, Inc., New York, USA., (1993), ch. 3.
- 5. The Merck Index, Ed. S. Budavari, Merck and Co., Inc., Rahway, USA., (1989), 11th edition.
- 6. Garside, J., Chem. Engng. Sci., 40:1, (1985), 3.
- 7. Chakraborty, R., Berglund, K. A., AIChE Symp. Ser., 83:284, (1991), 114.
- 8. Chakraborty, R., Berglund, K. A., J. Cryst. Growth, 125, (1992), 81.

AN INVESTIGATION OF THE FEASIBILITY OF ATR FTIR SPECTROSCOPY FOR IN SITU MEASUREMENT OF CRYSTALLIZATION PHENOMENA

3.1 Background

Numerous analytical techniques for the measurement of supersaturation of solutes in liquids have been proposed [1, 2, 3, 4, 5, 6]. They range from simple residual weight determinations to radioactive tracer methods. The primary difficulty in using most conventional analytical techniques for the measurement of supersaturation is the requirement of phase separation for analysis. Both the presence of a slurry and the slurry density can adversely affect the measurement. Consequently, such techniques are not adequately suited for *in situ* measurement.

ATR FTIR spectroscopy [7] provides a unique sampling configuration in which the infrared spectrum of the liquid phase of a slurry can be obtained without phase separation. The approach was predicated on the assumption that effective contact can be limited to that between the liquid phase of the slurry and the ATR apparatus. The validity of the assumption was verified in the study presented in Chapter 1 [8]. Substantial evidence for the feasibility of ATR FTIR spectroscopy for the measurement of

Dunuwila, D. D., Berglund, K. A., (in review) Ind. Eng. Chem. Fundamentals, (1995).

open Boat Cell used in the study presented in Chapter 2 was not configured for in situ measurements. Therefore, the focus of this chapter is establishing the technical feasibility of ATR FTIR spectroscopy for in situ measurement of crystallization phenomena. This continuing effort was inspired by recent developments in ATR FTIR technology in the form of various flexible radiation transfer systems and ATR configurations particularly suited for in situ measurements. One such device is the DIPPER® 210 immersion probe manufactured by Axiom Analytical, Inc. of Irvine California, USA that was used in this investigation.

3.2 Materials and Methods

In situ measurements of supersaturation, solubility and the metastable limit were performed using a DIPPER[®] 210 ATR FTIR immersion probe equipped with an AMTIR-1 conical internal reflection element manufactured by Axiom Analytical, Inc. of Irvine, California, USA. A simple schematic of the experimental setup is given in Figure 3.1. Temperature control of the 2L baffled and jacketed glass crystallizer was accomplished by a Lauda Brinkmann Refrigerating Circulator, model RC6. The crystallizer was purchased from Lab Glass, Inc. Stirring was provided by a 2^m polystyrene marine impeller powered by a Fisher Scientific StedFast™ stirrer, model SL600. The infrared spectrometer was a Perkin-Elmer 1750 Infrared Fourier transform spectrometer connected to a

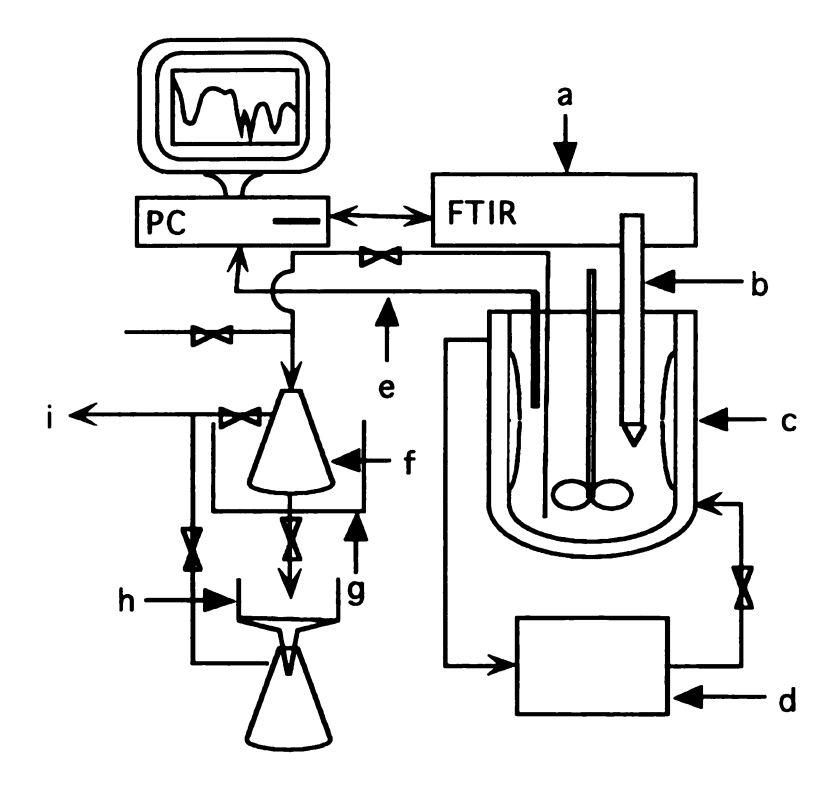


Figure 3.1 A schematic of the experimental setup.

a = spectrometer, b = ATR immersion probe,

c = Crystallizer, d = Chiller, e = Crystallizer temperature relay,

f = Product holding tank, g = Temperature controlled bath,

h = Buchner funnel, I = vacuum

Gateway 2000 486DX2-50V micro computer and the spectrometer was supported by Perkin-Elmer IRDM software. The slurry temperature was recorded using an Omega RD-TEMP-XT temperature logger and monitored using an Omega OL-703 linear response thermistor probe connected to a Omega DIGICATOR® digital readout.

The solute-solvent system studied was maleic acid in water and maleic acid was purchased from the Aldrich Chemical Company.

3.2.1 Measurement of Solubility In Situ

Solubility was measured in a slurry at temperatures ranging from 50°C to 67°C. At each temperature, solubility was approached both from supersaturation and undersaturation in order to insure accuracy of the measurements. At least five spectra were scanned per setting (i.e., at least 10 spectra at each temperature setting since solubility was approached both from supersaturation and undersaturation).

3.2.2 Measurement of Supersaturation In Situ

A 63% (w/w) maleic acid solution (total weight was 2 kg) was slightly supersaturated by cooling to 63°C, seeded and cooled by applying predetermined cooling profiles. Two grams of 463 micron seeds were used. Three distinct cooling profiles were used. The product crystals were collected at 56°C. ATR FTIR spectra were accumulated every 20 seconds.

3.2.3 Measurement of CSD

The product crystals were vacuum filtered and washed with ethyl ether under vacuum immediately. The product was dried overnight at 45°C in a Fisher Scientific ISOTEMP programmable oven, model 818F, before subjecting to sieve analysis. Sieve analysis was done using a Tyler RX-86

sieve shaker.

3.2.4 Construction of the Calibration Curves

Appropriate amounts (weight) of maleic acid and distilled water were placed in the crystallizer and heated to a homogeneous solution. The solution was cooled while accumulating solution ATR FTIR spectra, in situ, every 2 minutes until maleic acid spontaneously nucleated. A series of such experiments ranging from 59 to 65 % (w/w) maleic acid was conducted. At each weight percent, experiments were conducted in duplicate.

3.3 Results and Discussion

ATR FTIR spectra of aqueous maleic acid solutions are given in Figure 3.2. The decrease in intensity of infrared transmission bands of maleic acid relative to that of water (in the vicinity of 3400 cm⁻¹: OH stretching) as the maleic acid concentration is increased from 50 to 65 %(w/w) is clearly evident.

In Chapter 2, the merits of using a transmittance intensity ratio between a solvent band and a solute band as the entity that reflects crystallization parameters were discussed and results that justify the use of a transmittance ratio were presented [8]. Accordingly, we used a transmittance intensity ratio for *in situ* measurement of supersaturation, solubility and the metastable limit. Technically, it is plausible to use any of the maleic acid bands that appear in Figure 3.2 as the denominator of the transmittance ratio. However, upon closer observation it was noted that the band at 1172 cm⁻¹ is more sensitive to changes in solute concentration than are the bands at 1222 cm⁻¹ and 1707 cm⁻¹. Therefore, the

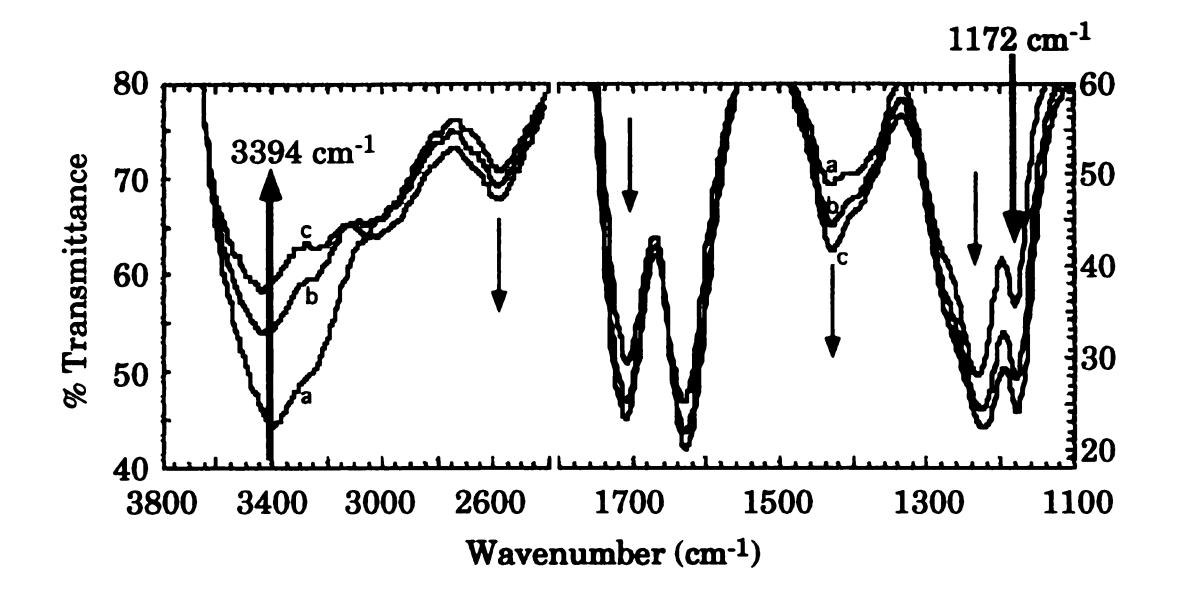


Figure 3.2 ATR FTIR spectra of aqueous maleic acid as the maleic acid concentration (% w/w) was increased (a=50%, b=60%, c=65% maleic acid in water). The arrows indicate the direction of peak intensity movement with increase in maleic acid concentration. The thick arrows indicate the peaks chosen for the transmittance ratio, T_R .

 $T_R = \frac{\text{transmittance at } 3394 \text{ cm}^{-1}}{\text{transmittance at } 1172 \text{ cm}^{-1}}$

transmittance ratio, T_R , was defined as;

$$T_R = \frac{\text{transmittance at 3394 cm}^{-1}}{\text{transmittance at 1172 cm}^{-1}}$$
(3.1)

In the following discussion, we have chosen to represent solubility, supersaturation and the metastable limit in terms of T_R since T_R , which is a function of concentration and temperature, reflects these parameters implicitly. Alternatively, crystallization parameters can be represented in terms of concentration. In doing so, however, the useful signal gain provided by the exponential gain in T_R is sacrificed.

3.3.1 Measurement of Solubility In Situ

Achievement of equilibrium poses a significant problem in measurement of solubility. Often, prolonged agitation at constant temperature is necessary for systems to reach equilibrium. Contact for days and weeks is not uncommon for some highly viscous solutions and systems at relatively low temperatures. Substances of low solubility may also require long contact times. Thus, the most convenient method for measurement of solubility would be one that is suitable for in situ measurements since a system approaching equilibrium can be monitored, minimizing expended time and effort. As alluded to in the previous chapter, conventional techniques do not meet these requirements. For example, it is inconvenient to monitor a system steadily approaching equilibrium using these techniques since portions of solutions have to be sampled frequently for analysis. However, continuous observation can be easily accomplished through in situ utilization of ATR FTIR spectroscopy. In order to check the accuracy of solubility determinations, it is recommended to approach equilibrium from both the undersaturated and supersaturated states. The capability of an *in situ* measuring device to continuously monitor the system dynamics make such checks easier.

The solubility of maleic acid in water measured in a slurry, in situ, is given in Figure 3.3. The data represent the average of T_R obtained upon approaching solubility from both the supersaturated state and the undersaturated state. In both approaches, when there was no significant change in T_R , the system was considered to be at or close to equilibrium. Since the measured solubility can be the average of measurements from both approaches, it is not necessary to prolong experiments until thermodynamic equilibrium is reached. Thus, the technique is convenient and time-saving. The experimental solubility data clearly demonstrate that ATR FTIR spectroscopy can be used to measure crystallization parameters in situ, in slurries, with a tolerable noise level. Certainly, these features of in situ ATR FTIR spectroscopy manifests the viability of the technique for application in process development of crystallization processes.

3.3.2 Measurement of the Metastable Limit In Situ

The metastable limit along with the solubility defines the operating zone of bulk crystallization from solution as illustrated in Figure 3.4. The metastable limit is the critical supersaturation at which point the system nucleates spontaneously (primary nucleation) [9]. Therefore, the dominating event of a system operating in the vicinity of the metastable limit is primary nucleation. Primary nucleation generates an excessive

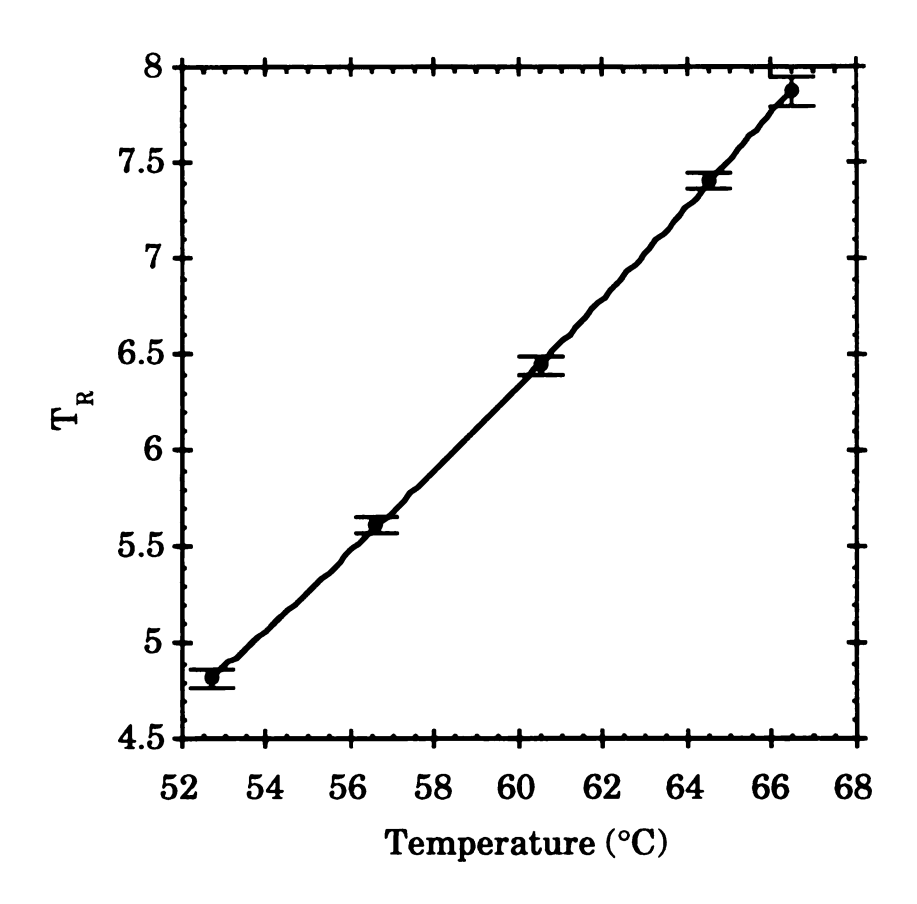


Figure 3.3 Solubility of maleic acid with respect to T_R measured in situ, in a slurry.

 $T_R = \frac{\text{transmittance at 3394 cm}^{-1}}{\text{transmittance at 1172 cm}^{-1}}$

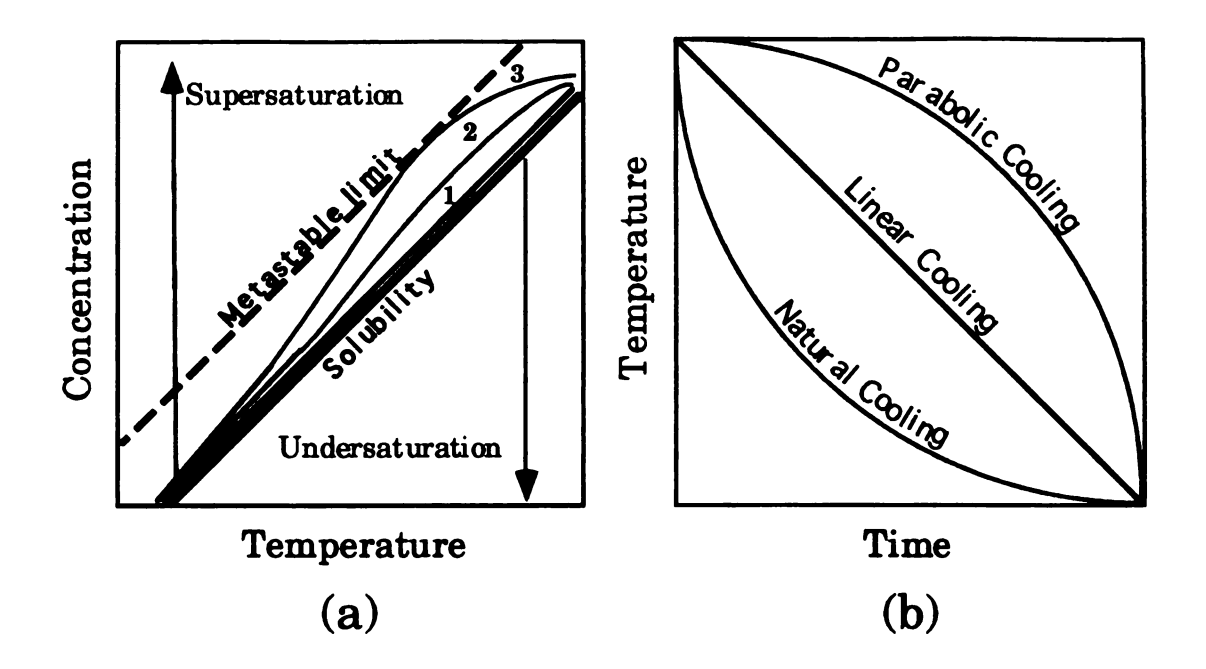


Figure 3.4 Simulated desupersaturation profiles, (a), of cooling batch crystallization. The desupersaturation profiles 1, 2 and 3 correspond to parabolic, linear and natural cooling profiles, (b), respectively.

number of nuclei. Consequently, the average sizes of CSDs resulting from desupersaturation profiles that approach the metastable limit are very small. Such distributions can be overly taxing on filtration and drying units, driving up operation costs. Away from the metastable limit and close to the solubility line, secondary nucleation (nuclei formed from collisions and shear) and growth events are prominent. In this circumstance, due to the lack of driving force, the limited number of nuclei grow slowly resulting in coarser CSDs. Therefore, to meet CSD specifications, the level and the rate of supersaturation should be maintained appropriately. The level of supersaturation corresponding to target product specifications depend on the width of the operating zone defined by the metastable limit and solubility. Therefore, the knowledge of the location of the metastable limit will give engineers a better grasp on system behavior, allowing more effective operations.

The metastable limit of a particular system depends on the supersaturation rate and the hydrodynamic conditions of the crystallizer [9]. Since the metastable limit depends on the hydrodynamic conditions of the crystallizer, it is imperative that it be measured under the same conditions that the material will be crystallized. ATR FTIR spectroscopy is a particularly convenient technique that provides the opportunity to measure the metastable limit in situ. The metastable limit can be measured easily as illustrated by experimental data in Figure 3.5. A homogeneous solution at point X can be cooled while accumulating ATR FTIR spectra $(T_R$ accumulated every 20 seconds) of the supersaturation profile. At point Y_1 , the system nucleates spontaneously and rapidly desupersaturates due to

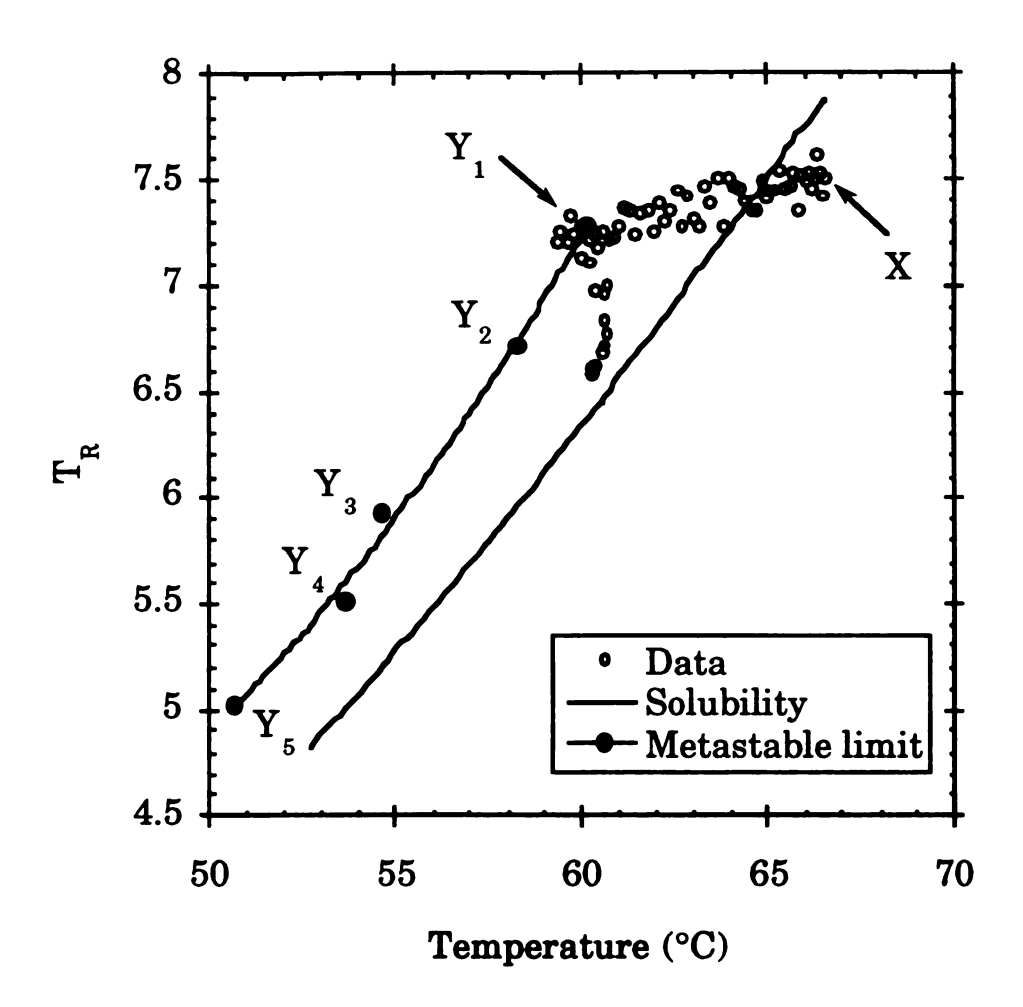


Figure 3.5 The metastable limit of maleic acid, (Y_i) , measured at a cooling rate of 1.3 °C/min. and a stirring rate of 420 rpm. The result of one experiment is given for illustration purposes. For the given experiment, point X denotes the initial conditions and point Y_1 denotes spontaneous nucleation. All points, Y_i , were extracted from similar experiments.

 $T_R = \frac{\text{transmittance at 3394 cm}^{-1}}{\text{transmittance at 1172 cm}^{-1}}$

excessive nucleation and growth. Thus, point Y_1 is one point of the periphery of the operating zone for the given system under the implemented cooling and stirring conditions. In this case, the cooling rate was 1.3 °C/min. and the stirring rate was 420 rpm. The cooling rate implemented was the maximum allowed by the capacity of the chiller. A series of experimental points, Y_i , constructs the metastable limit for the system under the given operating condition.

3.3.3 Measurement of Supersaturation In Situ

The primary impetus for measurement of supersaturation, in situ, is that it allows the estimation of kinetic parameters under hydrodynamic conditions governed by viscous properties of the system, heat and mass transfer properties and mixing patterns. The system kinetics in turn determine the process conditions. Crystallization process models indicate that, to maintain a desupersaturation profile as the one represented by profile number 1 of Figure 3.4, the temperature profile implemented should be parabolic in time [10, 11]. The initial rate of cooling corresponding to a parabolic cooling profile is very low and it increases progressively over the course of the batch time. On the other extreme, a natural cooling profile (uncontrolled cooling) leads to a supersaturation profile (profile number 3) that approaches the metastable limit resulting in extremely fine CSDs. The desupersaturation profile corresponding to the linear cooling profile may follow a course as the one depicted by profile number 2. The challenge in process development of batch crystallization is to ascertain the appropriate controlled cooling profile. The profile cannot be any parabolic or linear profile because the coefficients of the profile depend significantly on the kinetics of the particular system under operating conditions. Therefore, a consistent set of kinetic parameters that adequately describe process behavior is necessary for process development leading to efficient operation of crystallization processes. Models to extract growth kinetics from batch crystallizers and models to analyze batch crystallizers have been developed [12]. However, the use of kinetic models or the application of behavior models for industrial batch crystallizers has been stymied by the unavailability of an in situ measuring device for supersaturation which is the driving force for all crystallization phenomena. In essence, the prerequisite for the determination of coefficients of controlled cooling profiles satisfying product specifications based on system kinetics is the ability to measure supersaturation in situ.

In order to demonstrate the importance of *in situ* measurement of supersaturation for process development and control purposes and the effect of small changes in supersaturation on the product CSDs, the results of three experiments are presented. Results of each of the three experiments consist of a cooling profile, the corresponding desupersaturation profile and the resulting product CSD.

The three cooling profiles are given in Figure 3.6. They are identified as parabolic, intermediate parabolic and linear cooling profiles. The corresponding desupersaturation profiles are given in Figures 3.7 (parabolic), 3.8 (intermediate parabolic) and 3.9 (linear). The differences in the course of desupersaturation corresponding to the cooling profiles are clearly evident. The generation of a supersaturation peak as in the case of the desupersaturation profiles corresponding to the intermediate parabolic and

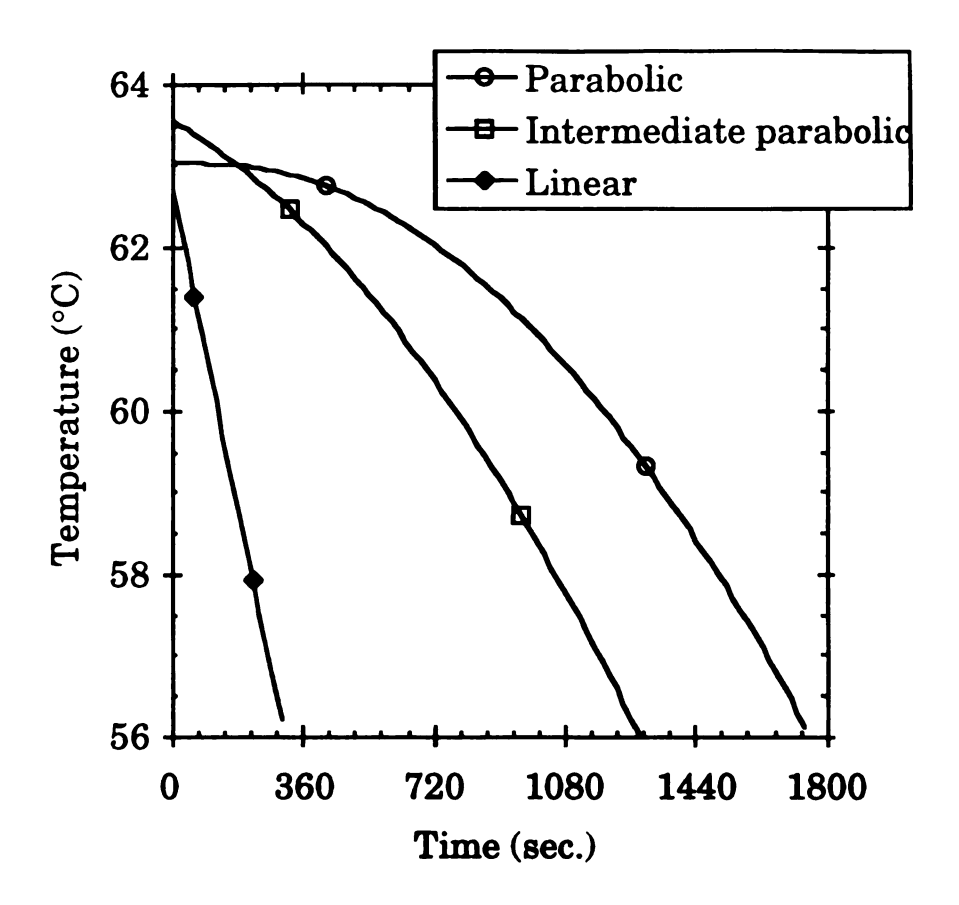


Figure 3.6 Experimental cooling profiles. They are identified as parabolic, intermediate parabolic and linear cooling profiles.

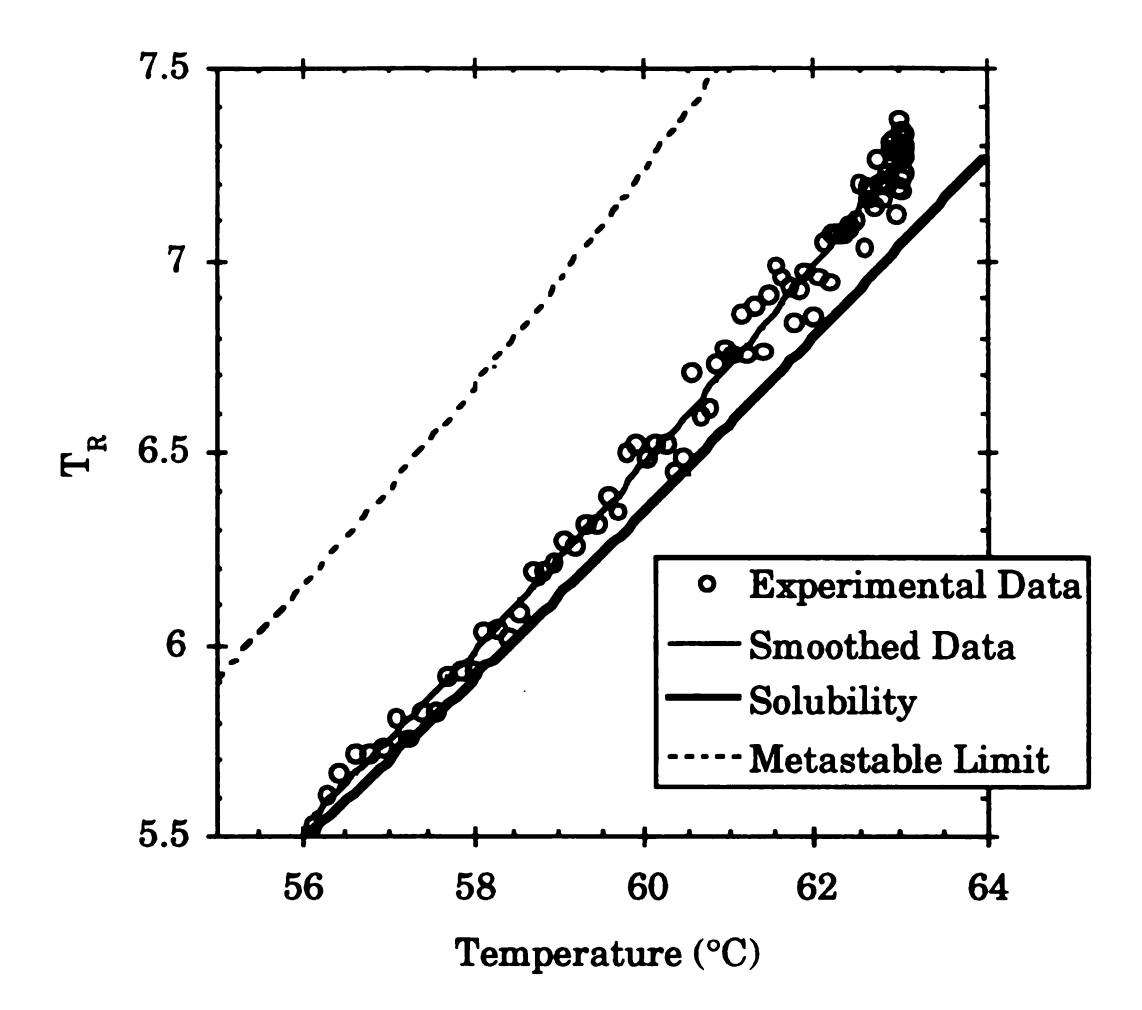


Figure 3.7 The desupersaturation profile corresponding to the parabolic cooling profile given in Figure 3.6.

$$T_R = \frac{\text{transmittance at 3394 cm}^{-1}}{\text{transmittance at 1172 cm}^{-1}}$$

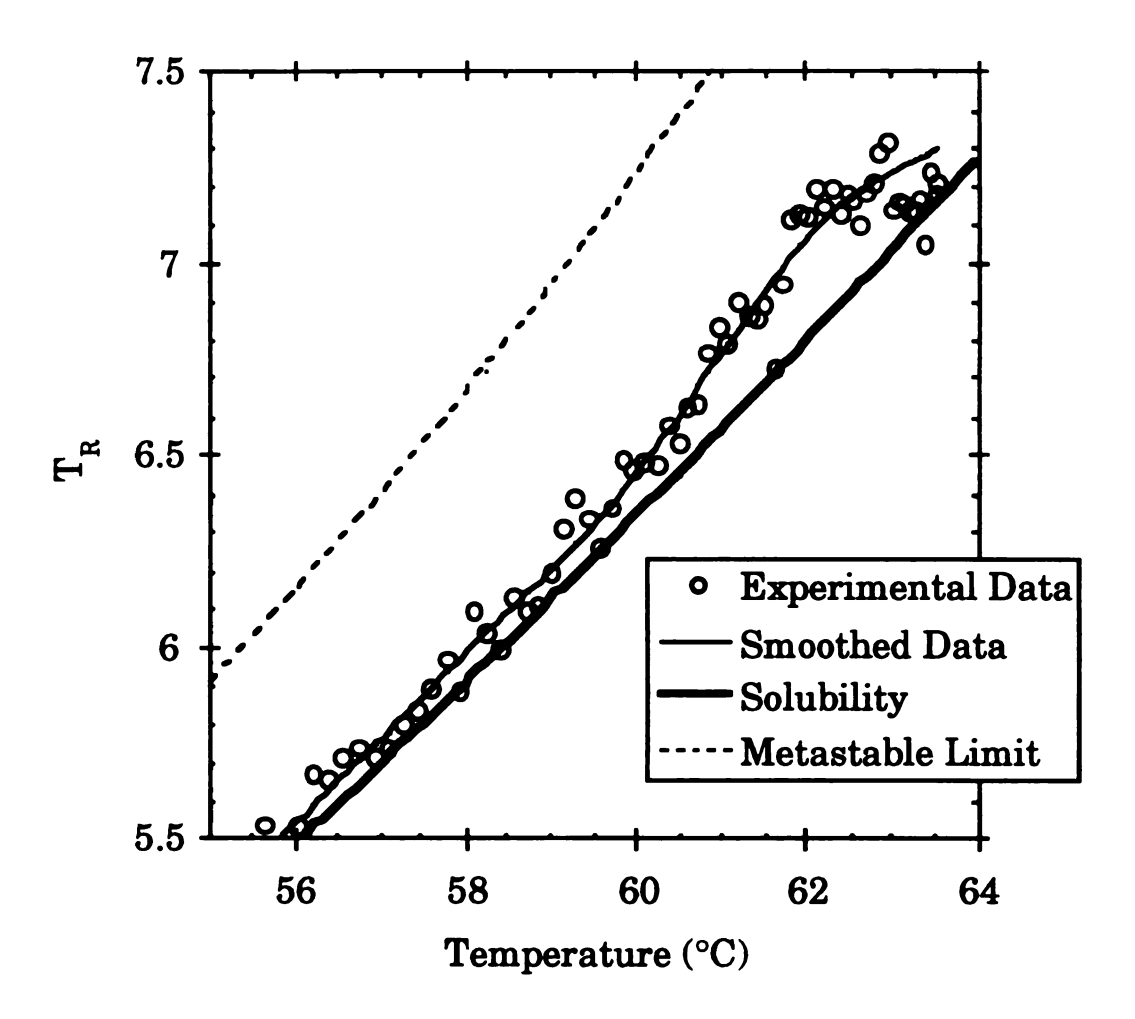


Figure 3.8 The desupersaturation profile corresponding to the intermediate cooling profile given in Figure 3.6.

$$T_R = \frac{\text{transmittance at 3394 cm}^{-1}}{\text{transmittance at 1172 cm}^{-1}}$$

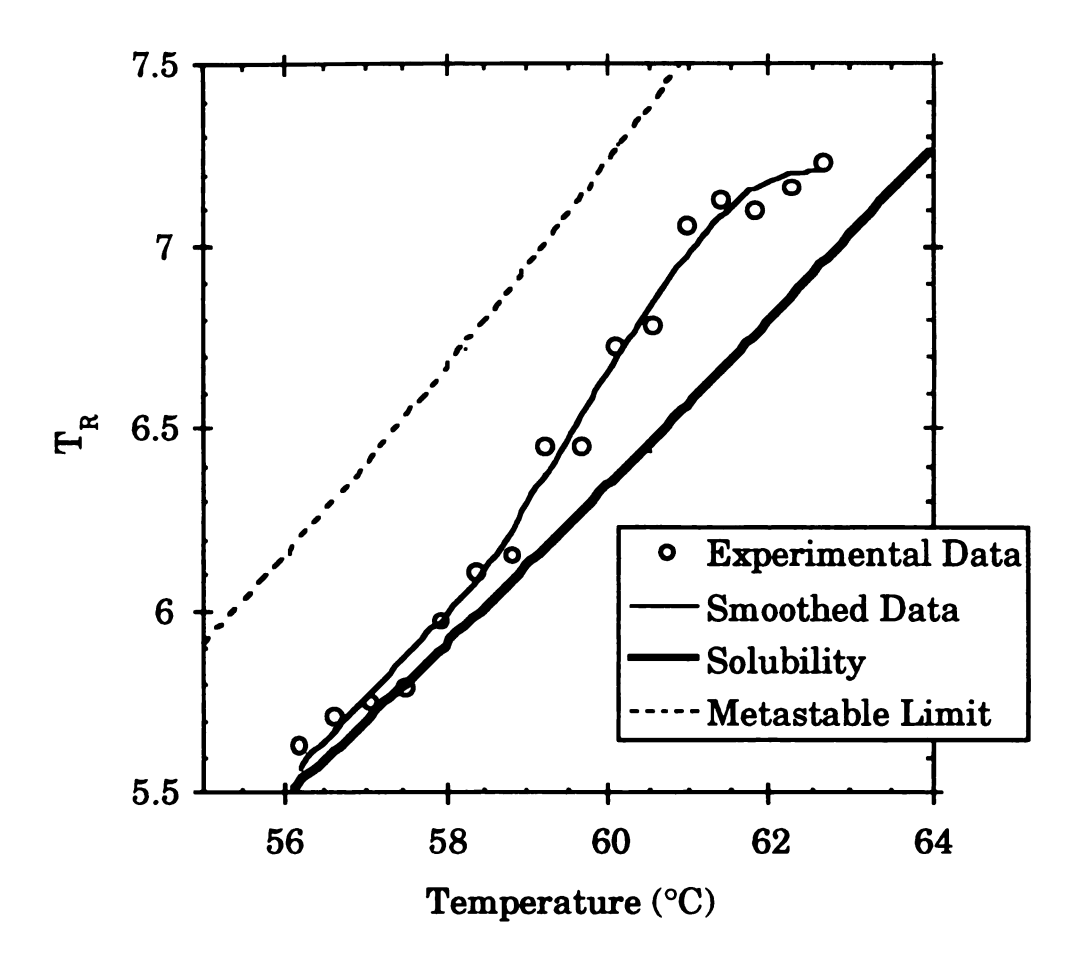


Figure 3.9 The desupersaturation profile corresponding to the linear cooling profile given in Figure 3.6.

 $T_R = \frac{\text{transmittance at 3394 cm}^{-1}}{\text{transmittance at 1172 cm}^{-1}}$

the linear cooling profiles or the lack thereof as in the case of the desupersaturation profile corresponding to the parabolic cooling profile, essentially determines the characteristics of the final product CSD [11]. The magnitude of the supersaturation peak depends on the implemented cooling profile. Thus, we emphasize the importance of extracting kinetic information from in situ measurements in order to determine the appropriate cooling profile. Consequences of implementing the wrong cooling profile can be detrimental. A faster rate of cooling will drive the system closer to the metastable limit resulting in a finer CSD than that specified causing operation problems at filtration and drying steps. On the other hand, unnecessarily slow cooling rates can stagnate the operation due to inadequate driving force resulting in unreasonably long batch times.

The experimental cooling profiles in Figure 3.6 were not based on system kinetics, rather they were chosen and implemented based on prior experience with the system to demonstrate the effect of differences in supersaturation on product CSDs. However, as part of this ongoing effort, the corresponding desupersaturation profiles will be used to extract kinetic parameters that will enable the determination of cooling profiles appropriate for specified CSDs. The subject is taken up in Chapter 5.

The mass based product CSDs resulting from desupersaturation profiles corresponding to the three cooling policies are given in Figure 3.10. The average size of the CSD resulting from the parabolic cooling profile is about 760 microns. The average size of the CSD resulting from the linear cooling profile is about 440 microns. The average size of the product resulting from the parabolic profile is nearly double in comparison to that

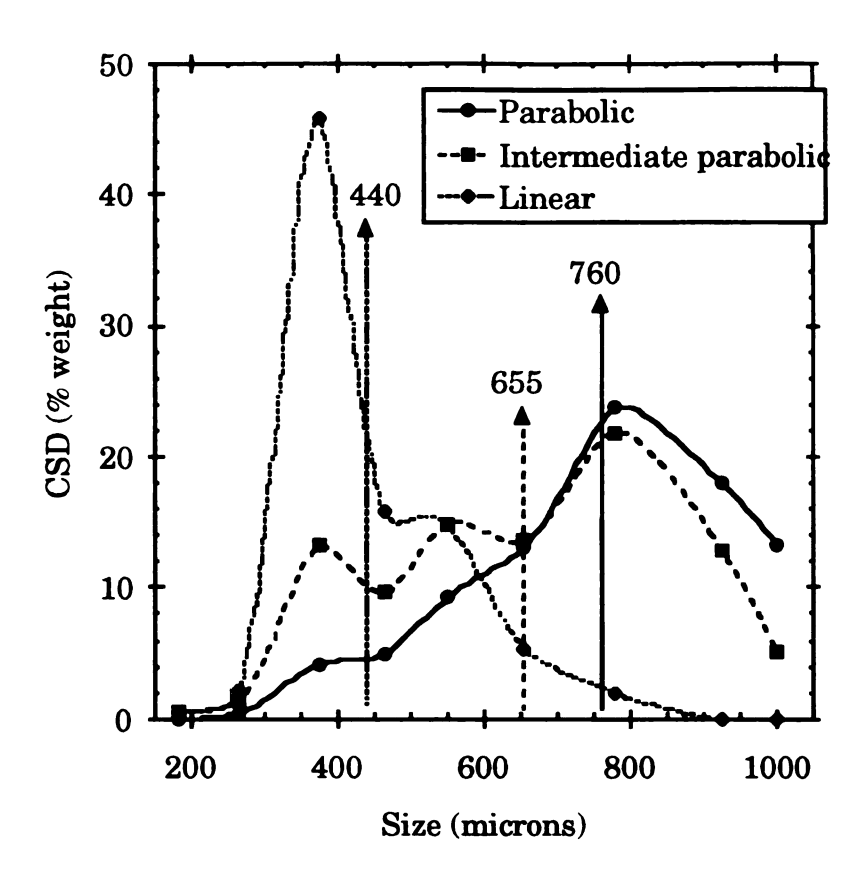


Figure 3.10 Mass based product crystal size distributions (CSD). The CSDs 1, 2 and 3 correspond to desupersaturation profiles 1, 2 and 3, respectively. The arrows indicate the mass based average sizes of each size distribution.

resulting from the linear profile. The changes in CSD characteristics are significant. This evidence underscores the importance of implementing the cooling profile befitting the specified CSD. Thus, it is anticipated that the ability to measure crystallization parameters, especially supersaturation, in situ, will have a considerable impact on the efficiency of process development and control of batch crystallization processes.

3.3.4 Calibrations

Calibrations can serve two purposes. First, they demonstrate that ATR FTIR spectroscopy, T_R , provides a true reflection of system variables. More importantly, calibrations provide the basis to extract the transient crystal slurry density. The slurry density is an explicit parameter in most batch crystallization process models [12, 13].

The calibrations of T_R for aqueous maleic acid with respect to temperature and concentration (% w/w maleic acid in water) are given in Figure 3.11. The plot consists of a three parameter grid comprising T_R , temperature and concentration on which the experimental solubility has been superimposed. Each point where the solubility line crosses the concentration lines indicates the solubility of maleic acid in water with respect to the solution concentration which is the more conventional way of representing solubility. This data is within 3% of the solubility data given in [9]. The accuracy of the current experimental data confirms that ATR FTIR spectroscopy is well suited to measure crystallization parameters.

Secondary nucleation depends on the slurry density. Therefore, slurry density is an explicit parameter in most batch crystallization process models. It is important to be able to measure the transient slurry density to

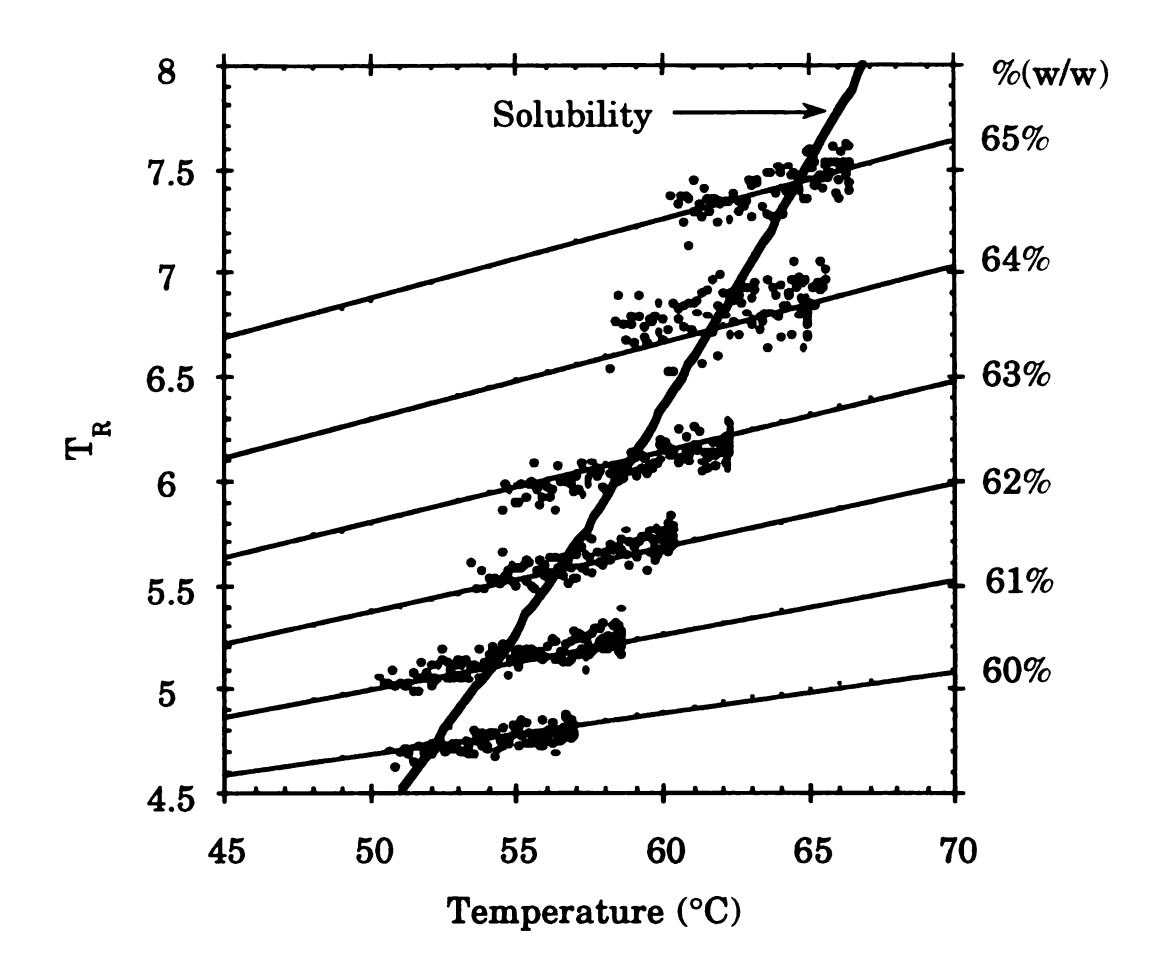


Figure 3.11 Calibrations of the transmittance ratio, T_R , with respect to temperature and maleic acid concentration (% w/w maleic acid in water). The constant concentration lines were extracted from the given experimental data.

 $T_R = \frac{\text{transmittance at 3394 cm}^{-1}}{\text{transmittance at 1172 cm}^{-1}}$

extract kinetic parameters and to accurately emulate system behavior.

The equation;

$$C = (a1 + a2 \times T + a3 \times T^{2})(b1 + b2 \times T_{R} + b3 \times T_{R}^{2})$$
 (3.2)

where T is the temperature, a1=1.079, $a2=-1.6989\times10^{-03}$, $a3=5.7812\times10^{-06}$, b1=40.39, b2=5.4039 and $b3=-2.7704\times10^{-01}$, gives the solution concentration of maleic acid in water at any point in the three parameter grid of Figure 3.11. Using this equation, the mass balance, the initial conditions and the batch volume, the transient slurry density can be easily calculated.

There is a noticeable increase in the noise level of the calibration data compared to the solubility data. This is due to the accumulation of air bubbles on the sensing head of the internal reflection element of the immersion probe. Air bubbles were a problem in the 2L crystallizer used for these experiments since its built-in baffle design is not adequate to completely avoid vortex formation. In the presence of a slurry, however, the crystals of the slurry inhibit the accumulation of air bubbles on the sensing head. Consequently, the noise level is dramatically reduced. This is clearly demonstrated by the low noise level in the solubility data that were measured in slurries. It is anticipated that air bubbles will not cause significant problems since the true measuring environment for crystallization parameters is a slurry.

3.4 Conclusions

The primary objective of this effort was to investigate the feasibility of ATR FTIR spectroscopy for *in situ* measurement of crystallization

parameters, especially supersaturation. To this end, the data have not only demonstrated that in situ ATR FTIR spectroscopy is well suited to measure supersaturation, the data have also demonstrated that ATR FTIR spectroscopy is sensitive enough to measure small changes in supersaturation that lead to significant changes in product CSDs. It is anticipated that the technique will be useful in process development and control of batch crystallization, providing for improved product quality/reproducibility and reduced energy utilization and cost of operation.

3.5 References

- 1. Zimmerman, H. K., Chem. Rev., 51, (1952), 25.
- 2. Liszi, I., Halász, S., Bodor, B., in: "Industrial Crystallization 87: Process Technology Proceedings, 6", Ed. Nyvlt, J.; Zacek, S., Elsevier, New York, USA., (1989), 399.
- 3. Ymamoto, H., Sudo, S., Yano, M., Harano, Y., in: "Industrial Crystallization 87: Process Technology Proceedings, 6", Ed. Nyvlt, J.; Zacek, S., Elsevier, New York, USA., (1989), 403.
- 4. Myerson, A. S., Rush, S., Schork, F. J., Johnson, J. L., in: "Industrial Crystallization 87: Process Technology Proceedings, 6", Ed. Nyvlt, J.; Zacek, S., Elsevier, New York, USA., (1989), 407.
- 5. Miller, S., Rawlings, J. B., AIChE J, 40:8, (1994), 1312.
- 6. Nyvlt, J., Karel, M.; Pisarik, S., Cryst. Res. Technol., 29, (1994), 409.
- 7. Mirabella, F. M., Ed., "Internal Reflection Spectroscopy", Dekker, New York, USA., (1993).
- 8. Dunuwila, D. D., Caroll II, L. B.; Berglund, K. A., J. Cryst. Growth, 137, (1994), 561.
- 9. Mullin, J. W., "Crystallization", Butterworth-Heinemann, Oxford, England, (1993).
- 10. Mullin, J. W., Nyvlt, J., Chem. Eng. Sci., 26, (1971), 369.
- 11. Jones, A. G., Mullin, J. W., Chem. Eng. Sci., 29, (1974), 105.
- 12. Tavare, N. S., Separation and Purification Methods, 22:2, (1993), 93.
- 13. Randolph, A. D., Larson, M. A., "Theory of Particulate Processes", Academic Press, New York, USA., (1988).

IDENTIFICATION OF FTIR SPECTRAL FEATURES RELATED TO SOLUTION STRUCTURE FOR UTILIZATION IN MEASUREMENT OF CRYSTALLIZATION PHENOMENA

4.1 Background

Carboxylic acids are generally characterized by vibrational modes of the carboxyl group [1]. Of the six vibrational modes of the carboxyl group, the v(C=O), v(C=O) and v(O-H) stretching vibrations and the $\delta(O-H)$ in-plane deformation vibration produce prominent fundamental IR absorbtion bands in the 1100-3000 cm⁻¹ region of the mid-IR spectrum. The nomenclature is discussed in [2]. The distinctive structure of the carboxyl group facilitates association of carboxylic acids through hydrogen bonding [1]. Association of carboxylic acids is illustrated in Figure 4.1. Formation of these dimers lowers the force constant of the v(C=O) and the v(O-H) vibrations and the frequency of the vibrations [3, 4]. The large decrease in frequency as a result of the transition from the monomeric to the associated form is evidence for the exceptional strength of hydrogen bonds. Hydrogen bonds, due to their strength, are largely responsible for the solution and crystal

Dunuwila, D. D., Berglund, K. A., Submitted to Trans. I. ChemE., (1995).

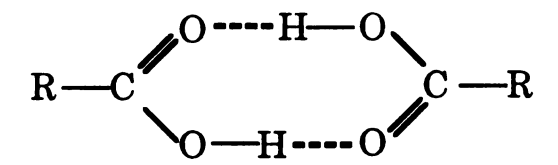


Figure 4.1 Self association of carboxylic acids via H-bonding.

structure of carboxylic acids. Consequently, any change in solution structure due to reactions, changes in composition, introduction of new species and temperature is reflected by spectral features produced by molecular vibrations affected by hydrogen bonding.

Carboxylic acids can form complexes with polar solvents via hydrogen bonds [1, 5, 6, 7]. Depending on the proton donor/acceptor strengths of polar solvents, carboxylic acids can form hydrogen bonds either by the participation of the carbonyl oxygen or the hydroxy group. However, intermolecular hydrogen bonding of dissimilar species is significantly weak compared to that of the same species.

4.1.1 Identification of the Vibrations of the Carboxyl Group

The v(O-H) Stretching Vibration: The v(O-H) vibration for monomeric carboxylic acids is observed around 3500-3570 cm⁻¹ [1, 8, 9]. The monomeric form occurs only in the vapor phase and in dilute solutions of nonpolar solvents. The broadened v(O-H) band of the associated form is observed over the range 2700-3100 cm⁻¹ [1, 3, 4, 10, 11]. The associated form, either dimeric or polymeric [9, 12], occurs almost exclusively in solid state, liquid state and in concentrated solutions. The shift of the v(O-H) band to lower frequencies upon association is characteristic of carboxylic acids. In addition, the broad band generally appears as a convoluted band made up of several bands. A simple interpretation is that the overlapping bands are due to a number of hydrogen bonds of varying lengths resulting from the complexity of associations [1]. An alternate interpretation is that this is due to coupling of the v(O-H) fundamental with several other low

frequency vibrational modes of the associated form [1, 13]. Other explanations are available [10].

The v(C=O) Stretching Vibration: The v(C=O) vibration for monomeric saturated aliphatic carboxylic acids is observed around 1780±15 cm⁻¹ [1, 3, 9]. The v(C=O) vibration for the associated form of saturated monocarboxylic acids (liquid and solid state) is found around 1710±10 cm⁻¹ [1, 3, 9, 10, 11] demonstrating the shift to lower frequencies upon association. Both the monomer (around 1760 cm⁻¹) and the dimer (around 1710 cm⁻¹) are observed in the case of many carboxylic acids in nonpolar solvents [1, 14].

The v(C-O) Stretching and the δ (O-H) In-Plane Deformation Vibrations: Coupling of the v(C-O) stretching and the δ (O-H) in-plane deformation vibrations occurring in the plane of the ring formed by the association of carboxylic acids result in two bands around 1420±20 cm⁻¹ and 1300±15 cm⁻¹ [1, 10, 11, 15]. The band at 1420 is assigned to v(C-O) and the band at 1300 is assigned to δ (O-H) [3]. These bands are reported to appear only under conditions that promote association via hydrogen bonding [1, 15]. These two bands are reported to shift in the opposite direction to that of v(C=O) and v(O-H) upon association [3, 9].

4.2 Materials and Methods

All details regarding the experimental setup and instrumentation are given in Chapter 3 and [16]. The protocols for the accumulation of solubility data and data corresponding to the constant concentration lines are outlined below. Further details are given in Chapter 3 and [16].

4.2.1 Measurement of Solubility in Slurries

Solubility was measured in a slurry, in situ, at temperatures ranging from 30°C to 70°C. At each temperature, ten spectra were scanned. Therefore, the plotted data represent the average of ten measurements. An equilibration time of about one hour was allowed for the slurry at each temperature setting. A slurry equilibration time of one hour was determined to be sufficient by monitoring the system approaching equilibrium both from supersaturation and undersaturation.

4.2.2 Construction of the Calibration Curves

Appropriate amounts (weight) of maleic acid and distilled water were placed in a 2 L crystallizer and heated to a homogeneous solution. The solution was cooled while accumulating solution ATR FTIR spectra, in situ, every 2 minutes until it spontaneously nucleated. A series of such experiments ranging from 50 to 65 percent maleic acid by weight was conducted.

4.2.3 Data Processing

Deconvolution: The spectral region between 2750-3700 cm⁻¹ was deconvoluted as follows. The given region was isolated from rest of the spectrum. The baseline of the absorbtion spectra was fixed at 3700 cm⁻¹ (that is, absorbance at 3700 cm⁻¹ was set to zero). Spectra were normalized at 3490 cm⁻¹. All spectral profiles were fitted to a function consisting of six Gaussian components using the "leastsq" least squares minimization function available in the professional version of the MATLAB optimization toolbox.

The six-component Gaussian function provided the best fit for the spectral profile. The contribution of each component to the spectral profile was generated using the adjustable parameters (peak position and standard deviation (peak width at half maximum)) of the corresponding Gaussian distribution.

Derivative Spectra: The derivative spectra of ATR FTIR absorbtion spectra were obtained. The peak positions of all the identified maleic acid vibrational modes and the useful peak intensities (intensities used to compute PIR_1 and PIR_2) were extracted from the derivative spectra and tabulated. This otherwise tedious task was simplified by using the user programmable OBEY programming utility available in the Perkin-Elmer IRDM software.

4.3 Results and Discussion

As discussed earlier, the primary focus of this paper was to investigate the methods available to identify and isolate the subtle features of IR spectra, that are susceptible to changes in solution structure, for utilization in measurement of crystallization parameters. Changes in molecular vibrational structure are manifested in spectral features such as shifts in peak positions and peak widths that may not be readily apparent [1]. Both derivative spectroscopy [17] and deconvolution [17] of overlapping bands can be used to isolate peak position and peak width shifts of IR absorbtion bands arising from reorganizations in solution structure. Derivative spectroscopy, which is a standard menu option in FTIR software, is the more straightforward method of the two and thus will be discussed

first. Although, some FTIR instrument manufacturers include a deconvolution algorithm as a standard menu option, these algorithms are designed only for peak enhancement and thus cannot resolve highly convoluted broad bands.

Spectral data can be cluttered by interferences and artifacts that appear in the form of polynomial shapes such as sloping lines or quadratic curves [17]. The derivative of the spectrum, which is one order higher than the polynomial shape, resolves some of the finer details concealed by the polynomial shapes. For example, the first derivative removes sloping lines and the second derivative removes quadratic curves and adds clarity to the spectrum. As such, derivative spectra can reveal a host of information otherwise hidden or not readily apparent in the original spectra and can be used to extract both qualitative and quantitative information. Figure 4.2 illustrates the derivative curves of a Gaussian band. The first and the third derivative curves give the precise peak position while the second and the forth derivative curves generate the inverted and the original curves, respectively. The illustrations are not intended to demonstrate the particular advantages of derivative spectroscopy, rather they demonstrate the results of taking the derivative of an ideal band up to the fourth derivative. Their utility in analyzing real spectra will be apparent shortly.

Figure 4.3 gives the ATR FTIR spectra (lower frequency window) of saturated aqueous maleic acid at various temperatures. Band assignments are indicated by the arrows [1, 3, 9, 10, 11, 14, 15]. These spectra are used to illustrate the advantages of derivative spectroscopy.

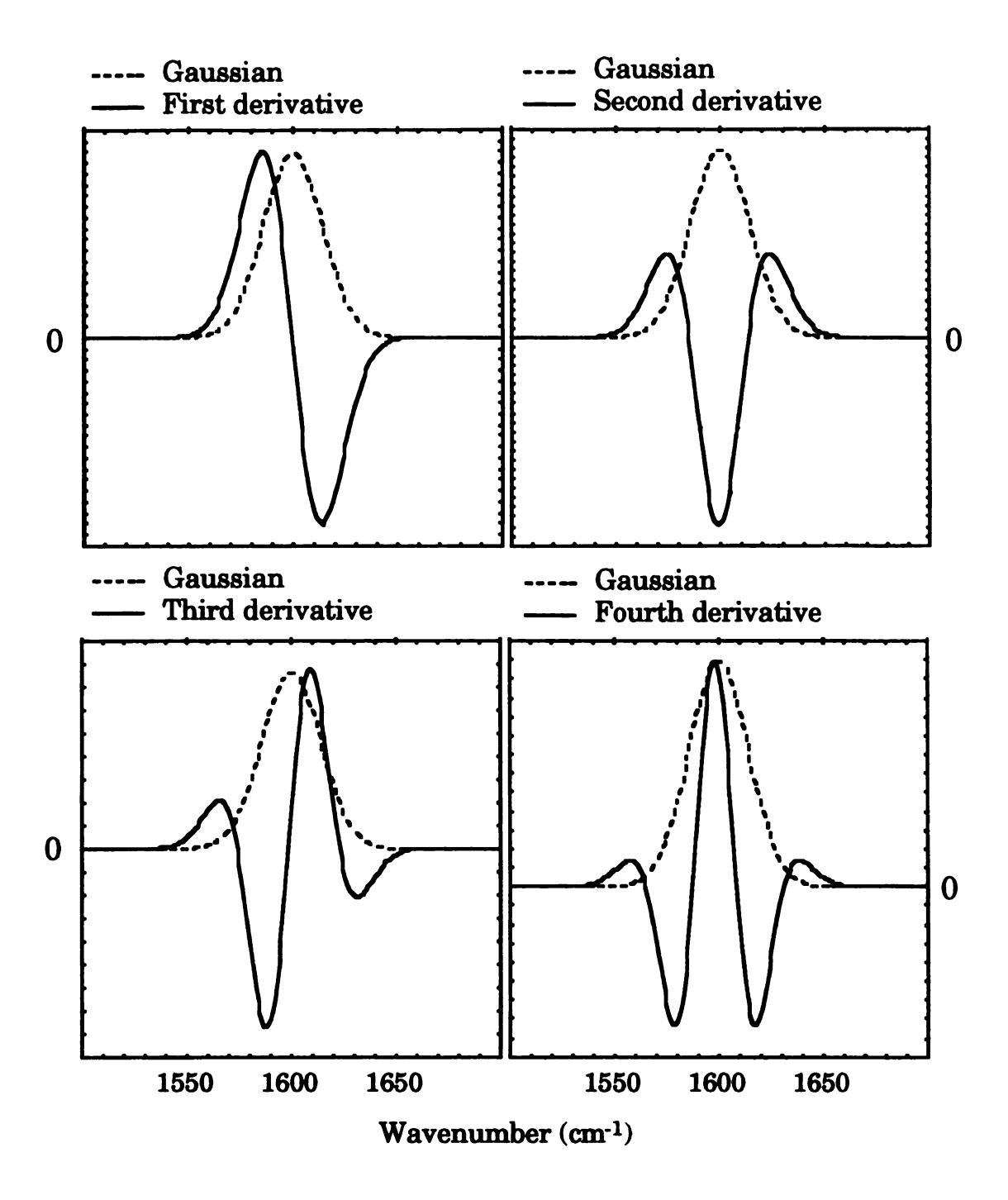


Figure 4.2 First, second, third and fourth derivatives of a Gaussian peak.

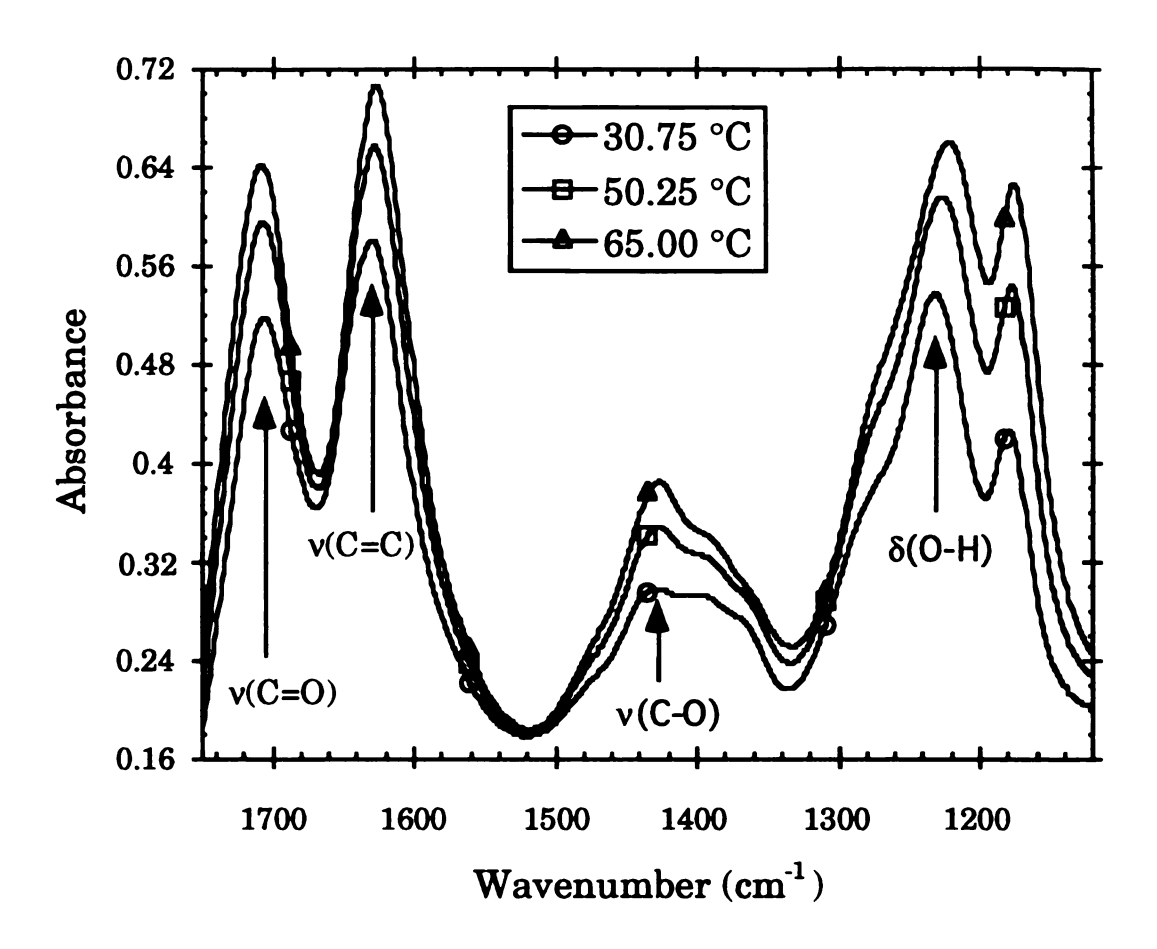


Figure 4.3 In situ, slurry ATR FTIR spectra of aqueous maleic acid at saturation in the low frequency region.

Consider the v(C=0) peak that occurs in the vicinity of 1700 cm⁻¹. It appears to be a single peak devoid of any other feature such as shoulders. However, the first derivative profile given in Figure 4.4 reveals information plausibly hidden by an artifact in the form of a polynomial shape. The most striking feature is the enhancement of a shoulder on the high frequency side of the v(C=O) peak that is manifested in the form of two peaks in the positive component of the derivative profile. A parameter can be defined based on a ratio (PIR_1) between the derivative absorbance peak intensity at 1740 cm⁻¹ to that at 1720 cm⁻¹ for the measurement of crystallization phenomena. A higher gain in PIR (peak intensity ratio) can be achieved by using an appropriate baseline as the one denoted by BL1 at 0.005. The solubility and the concentration lines of maleic acid with respect to PIR, measured in situ are given in Figure 4.5. This parameter is clearly a function of temperature and independent of concentration. Therefore, the concentration lines coincide with the solubility line. Consequently, this parameter is not suitable for the measurement of supersaturation of aqueous maleic acid. However, the results are presented to demonstrate the power of derivative spectroscopy in bringing out spectral features that may be used to measure crystallization parameters of many other systems.

Alternatively, a second parameter can be defined using the features of the first derivative of the v(C=0) mode. The defined parameter is the ratio (PIR_2) between the derivative absorbance peak intensity at 1740 cm⁻¹ to that at 1692 cm⁻¹ with the baseline adjusted to -0.012 (BL2) as indicated in Figure 4.4. Essentially, this parameter reflects the relative changes

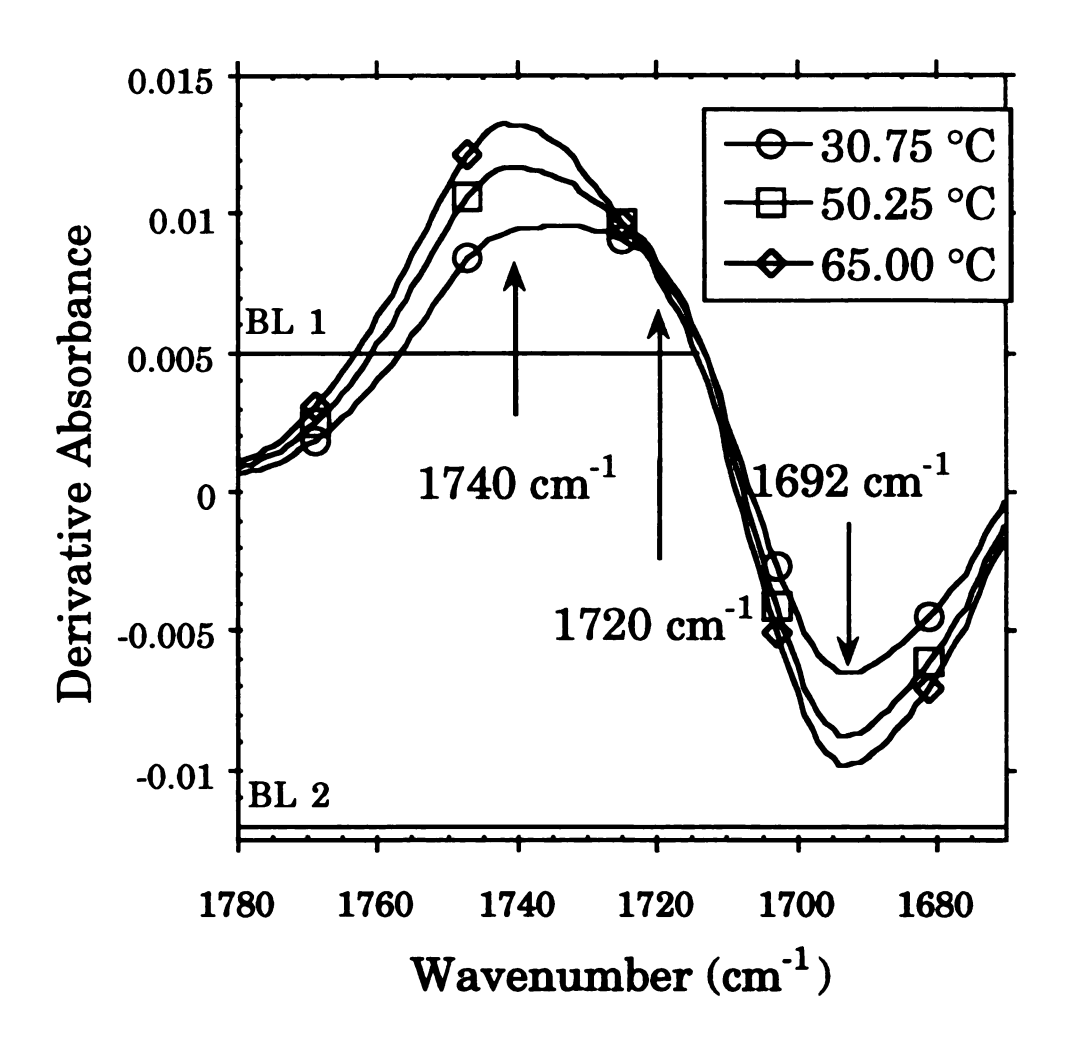


Figure 4.4 First derivative profiles of the v(C=O) vibrational mode from Figure 4.3. BL1=0.005 and BL2=-0.012 were the baselines used for PIR_1 and PIR_2 , respectively. $PIR_1=(DA \text{ at } 1740 \text{ cm}^{-1} - a)/(DA \text{ at } 1720 \text{ cm}^{-1} - a)$ $PIR_2=(DA \text{ at } 1740 \text{ cm}^{-1} + b)/(DA \text{ at } 1692 \text{ cm}^{-1} + b)$ a=0.005 and b=0.012 are the baseline adjustmentsDA=derivative absorbance

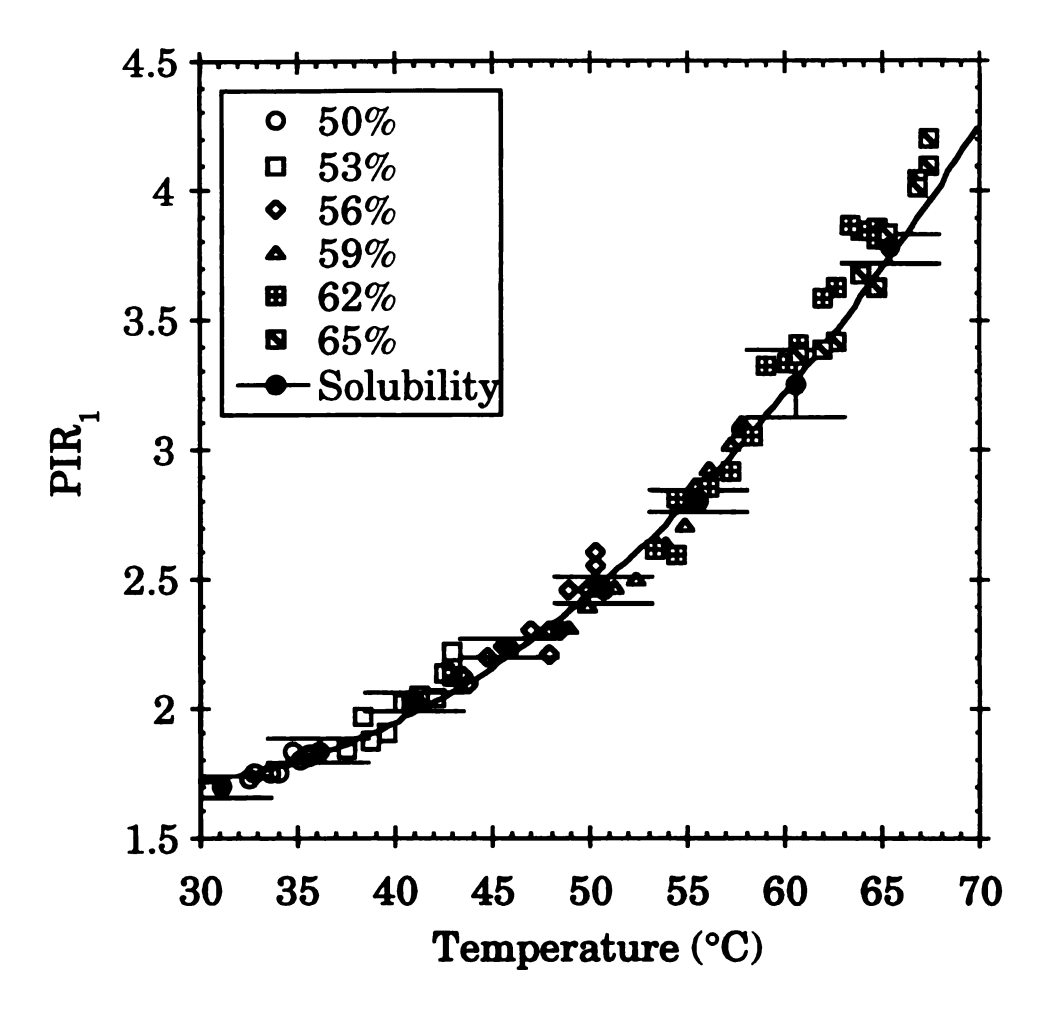


Figure 4.5 Solubility and concentration lines of maleic acid with respect to PIR_1 measured in situ. In addition, solubility was measured in a slurry.

 $PIR_1 = (DA \text{ at } 1740 \text{ cm}^{-1} - a)/(DA \text{ at } 1720 \text{ cm}^{-1} - a)$

DA=derivative absorbance

a=0.005 is the baseline adjustment

between the high frequency side of the v(C=0) peak and that of the low frequency side. The solubility and the concentration lines of maleic acid with respect to PIR_2 measured in situ are given in Figure 4.6. PIR_2 , unlike PIR_1 , is a function of concentration and only slightly dependent on temperature as demonstrated by slightly sloping concentration lines. The fact that PIR_2 is a strong function of concentration renders it a highly suitable candidate for measurement of supersaturation as demonstrated in Figure 4.6.

Previously [16, 18], it has been established that band ratioing techniques such as PIRs or area intensity ratios are the most appropriate for quantitative measurements. This is because ratioing gives rise to an internal standard that effectively eliminates errors due to instrumental drifts. Instrumental drifts usually occur due to energy fluctuations that arise as a result of radiation source instabilities and alignment problems of optical coupling attachments. In many systems, it may be difficult to identify features that can be used for ratioing in the original spectra. Features of infrared spectra of crystallization systems can be masked by the presence of various species such as impurities, byproducts and additives that have strongly absorbing vibrational modes making the identification of features suitable for ratioing difficult. In addition, most solvents have characteristic IR spectra. As demonstrated above, derivative spectroscopy can be successfully used to bring out features that are well suited for rationing. In this case, the v(C=0) peak used for demonstration is devoid of any identifiable feature in the original spectra. Nevertheless, the features that the first derivative profile reveals are quite remarkable. This is ample

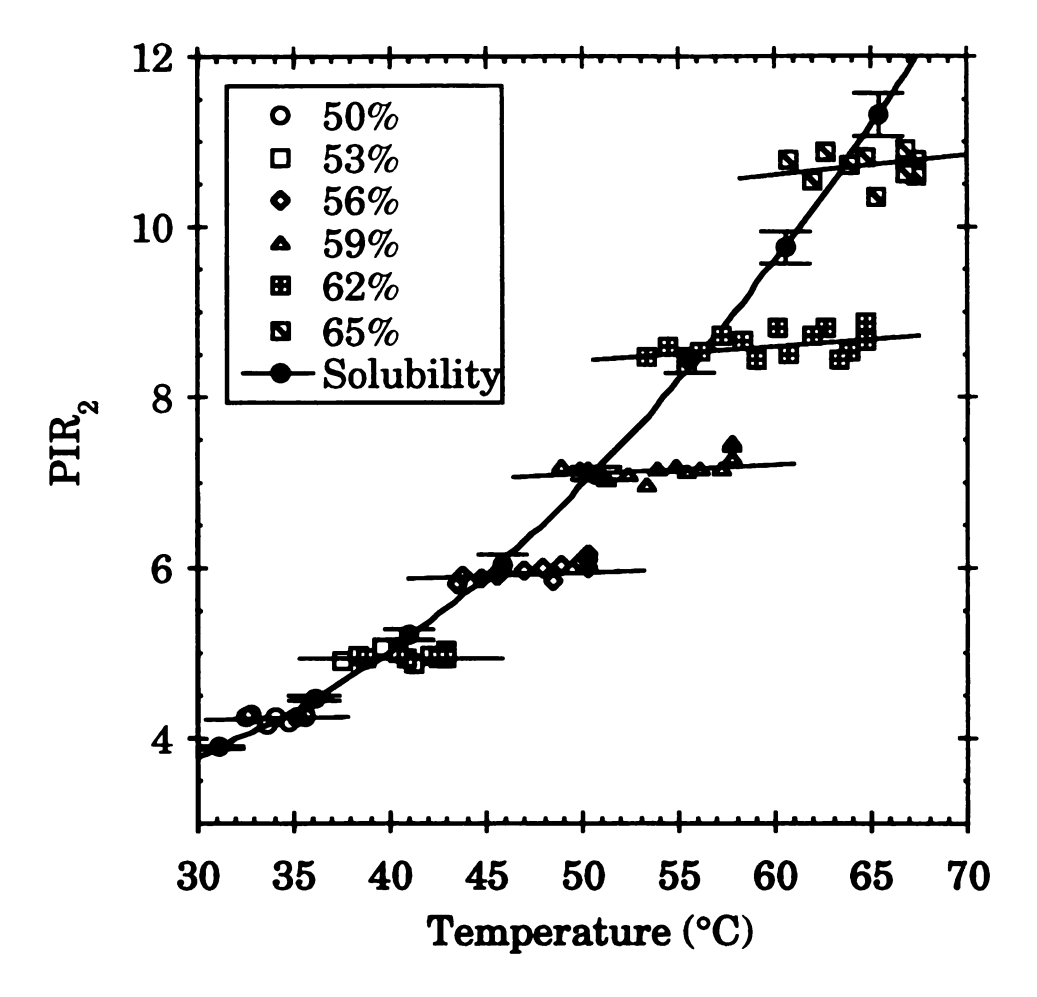


Figure 4.6 Solubility and concentration lines of maleic acid with respect to PIR_2 measured in situ. In addition, solubility was measured in a slurry.

 PIR_2 =(DA at 1740 cm⁻¹ + b)/(DA at 1692 cm⁻¹ + b)

DA=derivative absorbance

b=0.012 is the baseline adjustment

evidence for the power of derivative spectroscopy and in general for the far reaching utility of ATR FTIR spectroscopy for use in measuring and understanding crystallization phenomena.

As illustrated in Figure 4.4, the second derivative profile of a peak generates the inverted peak. It can be used to isolate the individual components of a convoluted band. Consider the v(C-O) peak at 1430 cm⁻¹ that is accompanied by three other shoulder peaks that may be due to vibrational mode coupling or overtones. The second derivative can be used to isolate the v(C-O) peak from the shoulder peaks. The inverted second derivative of the v(C-O) stretch at saturation is given in Figure 4.7. The relative changes of this peak in the original spectrum are identifiable. However, the same changes are more recognizable and convincing in the second derivative profile which is the isolated peak. The changes can readily be used for measurement of crystallization parameters. For example, a PIR between peak intensities at 1430 cm⁻¹ and 1442 cm⁻¹ is suitable.

Parameters discussed thus far for quantitative measurements were based on band ratioing techniques. Although they are highly suitable for quantitative measurements their relationship to solution structure may be ambiguous. A parameter that is suitable for quantitative measurements and capable of providing some insight to the solution structure of crystallizing systems is the peak shift of numerous vibrational modes. Just as H-bonding is responsible for causing the transition of monomeric carboxylic molecules in dilute solutions to associated forms in more concentrated solutions [1, 19], they are responsible for the crystal structure

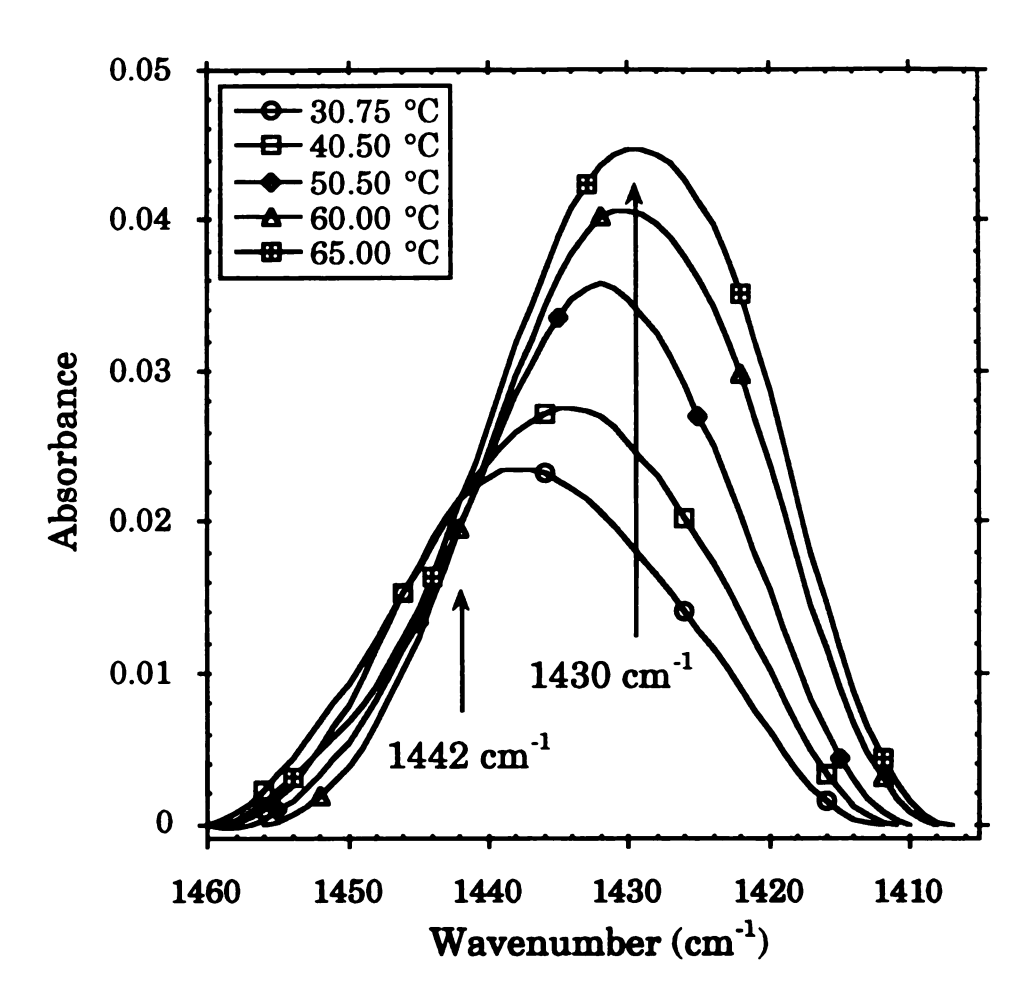


Figure 4.7 Isolated second derivative profiles of the v(C=O) vibrational mode of aqueous maleic acid at saturation.

and the preceding solution structure in supersaturated solutions. As the forces such as H-bonds that are responsible for the organization of molecules in supersaturated solutions gain in strength, the force constants of the vibrational modes adjacent to the site affected by H-bonding are reduced. The consequent reduction in vibrational frequency is reflected in the IR spectrum [3, 4]. Due to the presence of electronic phenomena such as inductive effects and conjugation [1], peripheral vibrational modes may be affected and the resulting structure is reflected in the IR spectrum.

Derivative spectroscopy is a convenient method for extracting peak shift information. The same information can be obtained from the original spectrum. However, the shifts are more discernible in derivative spectra (1st and 3rd derivative). Consider the δ (O-H) in-plane deformation vibration of maleic acid given in Figure 4.3. The red shift of the peak upon increasing saturation temperature conditions is evident. The same shift is more convincingly demonstrated by the derivative profiles of the peaks in Figure 4.8. The parameter Δv denotes the total shift of the peak in going from the solubility condition at 30.75 °C to that at 65 °C. The peak shift information was extracted using the user programmable OBEY programming utility available in the Perkin-Elmer IRDM software. A discussion of the use of maleic acid vibrational modes for the measurement of crystallization parameters of aqueous maleic acid and some insight to the organization of maleic acid in supersaturated solutions follows.

The covalent bond lengths and the interbond angles for maleic acid derived from the crystal structure are shown in Figure 4.9 [20]. The IR peak

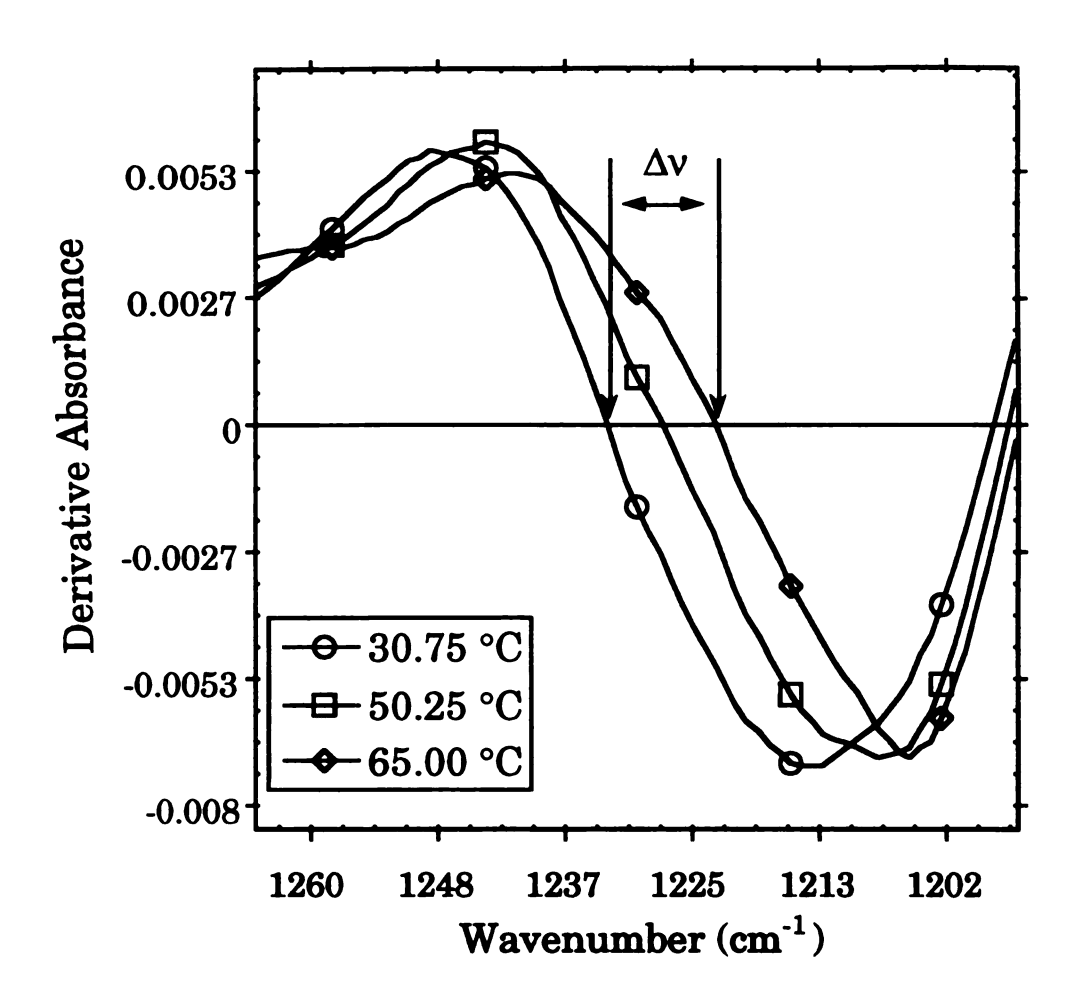


Figure 4.8 First derivative profiles of the δ (O-H) in-plane deformation vibrational mode from Figure 4.3.

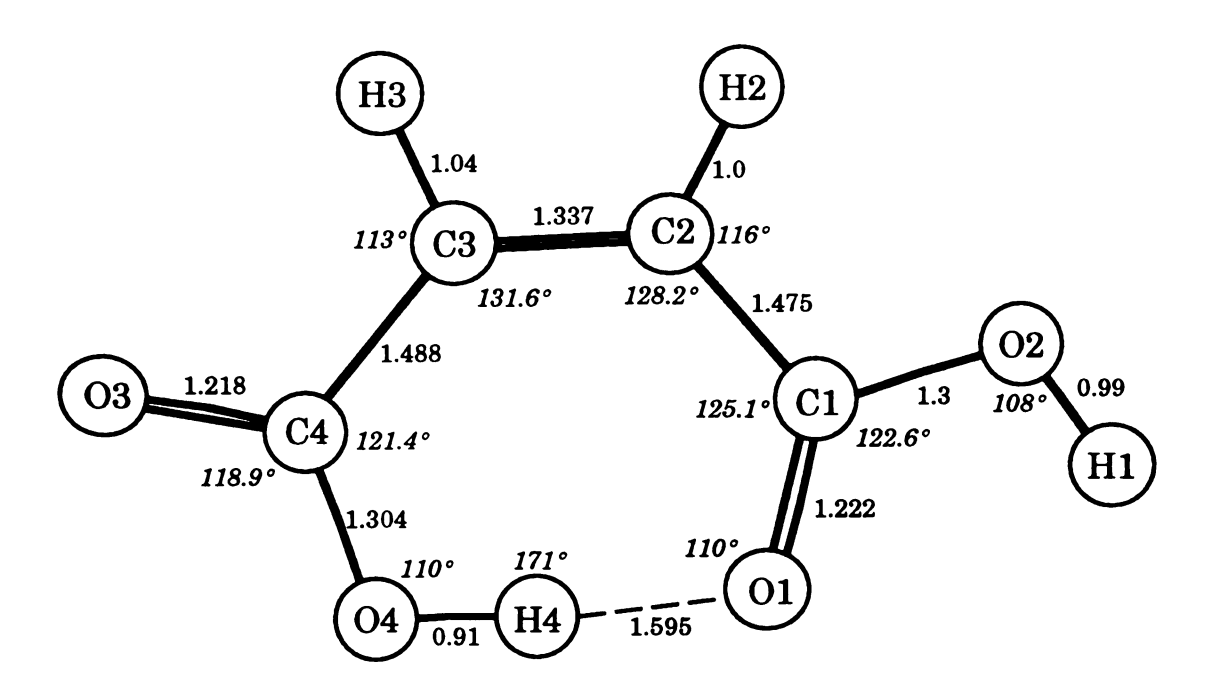


Figure 4.9 Bond distances and angles for the maleic acid molecule. Bond distances are given in Å and the angles are italicized for clarity.

positions of the numerous vibrational modes of crystalline maleic acid are as follows [1, 9, 21]. The v(C=O) stretching mode appears at 1705 cm⁻¹. The v(C-O) stretching mode appears at 1437 cm⁻¹. The v(C=C) stretching mode appears at 1635 cm⁻¹. The v(O-H) stretching vibration appears over the range 2500 - 3000 cm⁻¹. This band is modified by the v(C-H) stretching bands that occur over the 2800 - 3100 cm⁻¹ range. The δ (O-H) in-plane deformation appears at 1272 cm⁻¹. Evidence suggests that the folded structure of the maleic acid molecule in the crystalline state - due to intramolecular H-bonding - stays intact upon dissolution in concentrated solutions (0.3M) [5]. Therefore, it is plausible to expect a high level of similarity between the crystalline state IR spectra and the solution state IR spectra of maleic acid. A close comparison of the two confirms this rationalization. Upon supersaturation of aqueous maleic acid - that is when a solution is cooled and as a consequence it approaches the onset of nucleation - it is also expected that the solution state peaks will approach the solid state peak positions, given the similarity between the solid and solution state molecular structure. An absolute convergence is unlikely due to the higher level of organization in the crystal lattice. The following paragraphs examine the events that are expected to accompany the convergence of solid and solution state structures in terms of peak shifts and the utility of these shifts toward measurement of crystallization parameters.

Solubility and concentration lines of aqueous maleic acid with respect to the peak shift of the v(C=O) vibration measured in situ are shown in Figure 4.10. Solubility, in addition to being measured in situ, was measured in a slurry. When solutions at all concentrations are cooled, the v(C=O) stretching vibration red shifts to lower frequencies. This is clearly indicative of the strengthening H-bond. Upon cooling, H-bonds gains in strength. Consequently, the strength of the adjacent C=O bond or the force constant of the v(C=O) stretching vibration is reduced. This phenomenon is manifested in the IR spectrum as a red shift in the v(C=O) peak as shown in Figure 4.10.

Solubility and concentration lines of aqueous maleic acid with respect to the peak shift of the v(C-O) vibration measured in situ are shown in Figure 4.11. Upon cooling, unlike the v(C=O) peak, the v(C-O) peak demonstrates a blue shift. This is consistent with previous studies on association of carboxylic acids [3, 9]. The complexity of electronic effects such as inductive forces and conjugation that are affected by H-bonding may be responsible for the blue shift of the v(C-O) peak.

Solubility and concentration lines of aqueous maleic acid with respect to the peak shift of the v(C=C) vibration measured in situ are shown in Figure 4.12. When solutions at all concentrations are cooled, the v(C=C) stretching vibration red shifts to lower frequencies. Since most studies on association have been done using saturated carboxylic acids, peak shifts of

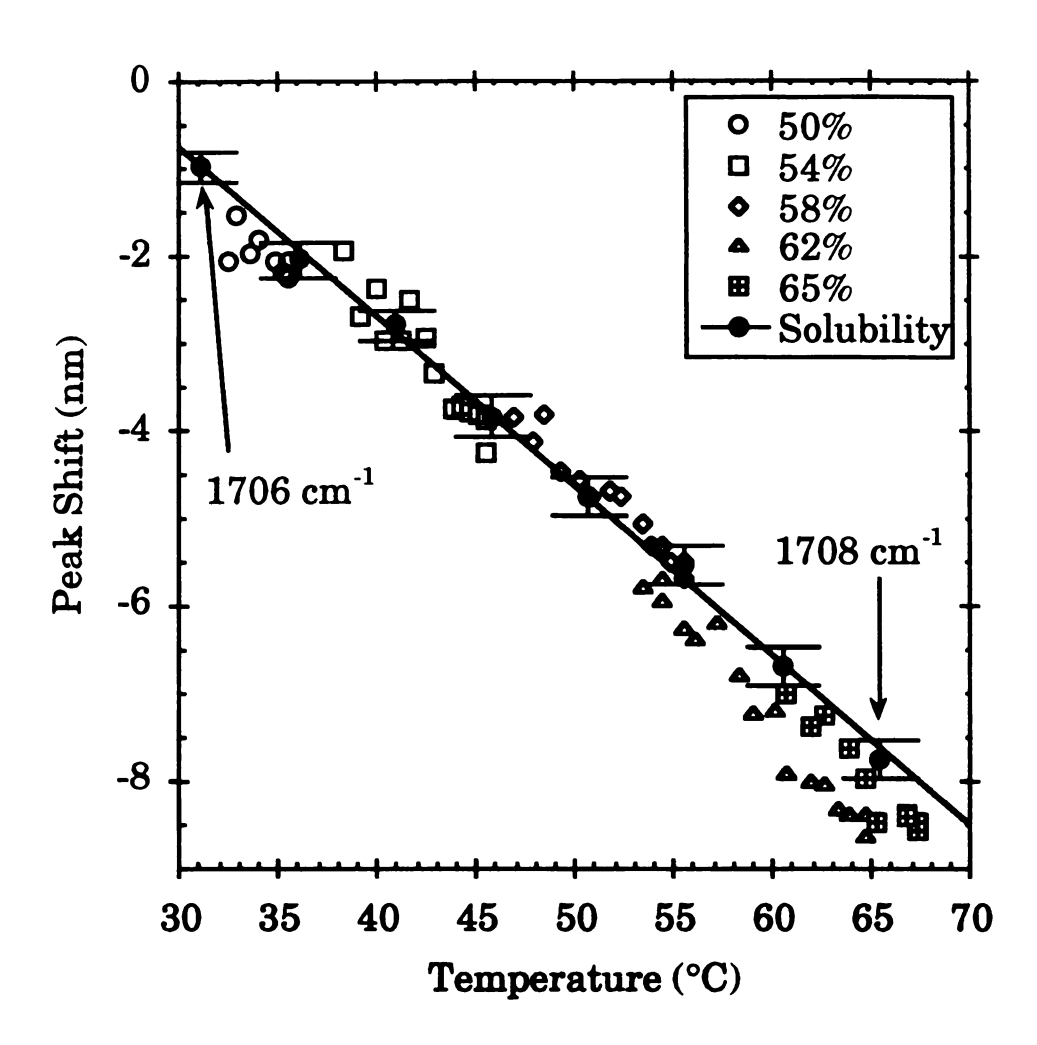


Figure 4.10 Solubility and concentration lines of maleic acid measured with respect to the peak shift of the v(C=0) vibrational mode, in situ. In addition, solubility was measured in a slurry. Absolute peak positions at two conditions are shown for reference purposes.

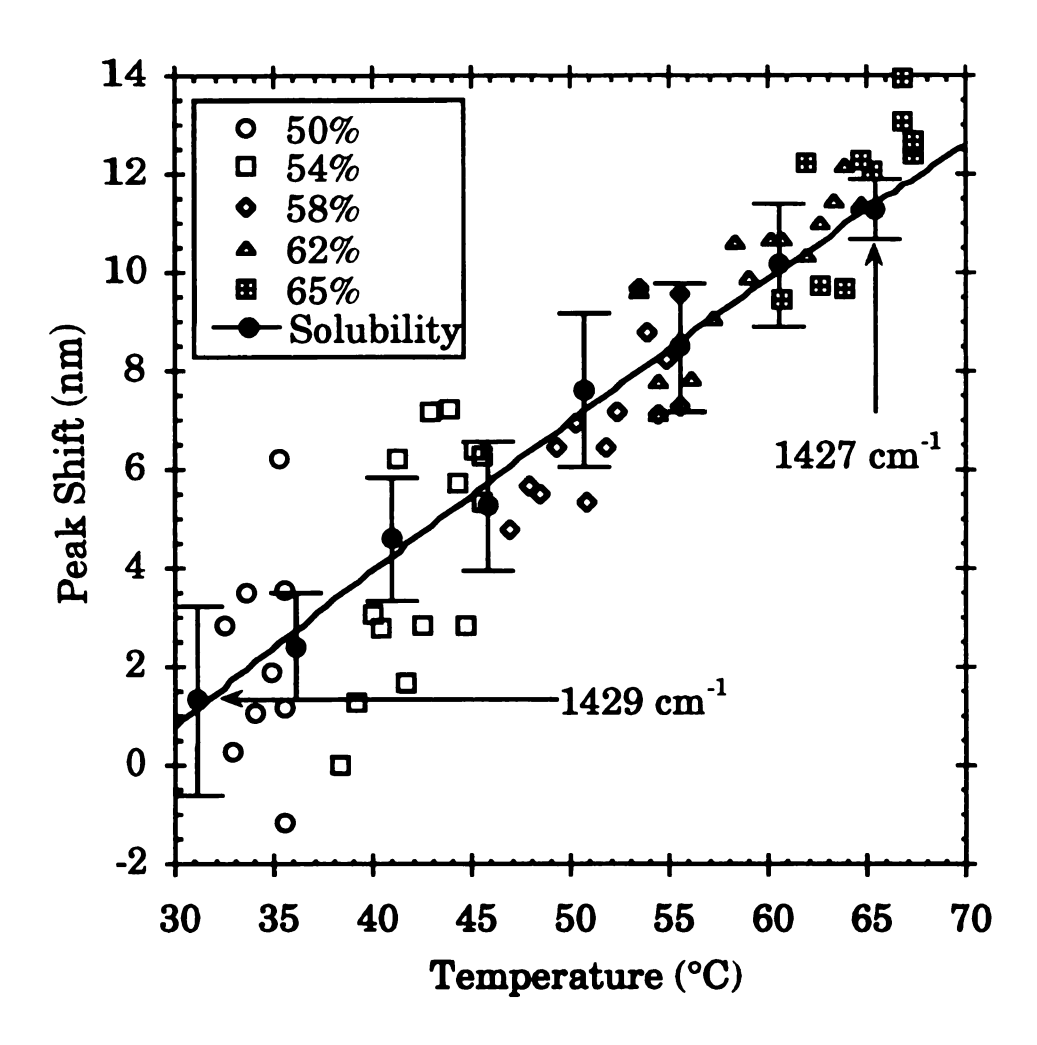


Figure 4.11 Solubility and concentration lines of maleic acid measured with respect to the peak shift of the v(C-O) vibrational mode, in situ.

In addition, solubility was measured in a slurry. Absolute peak positions at two conditions are shown for reference purposes.

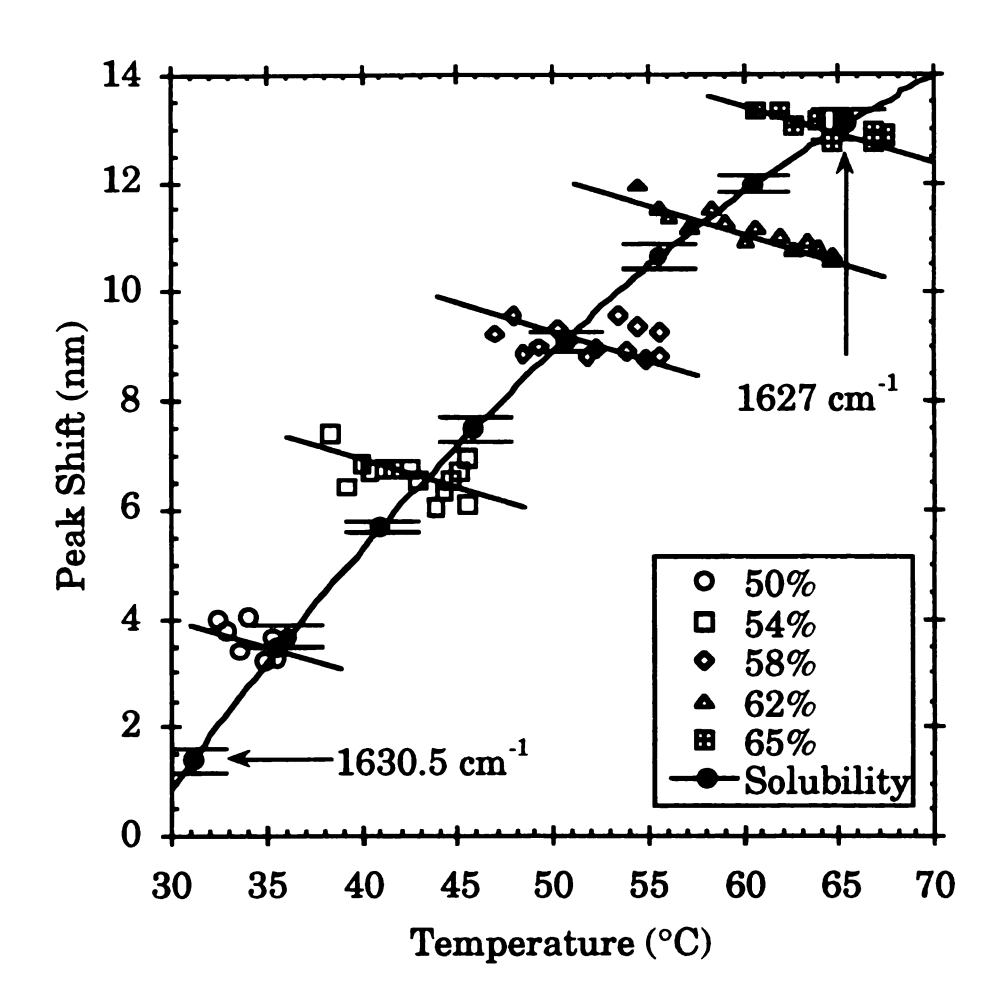


Figure 4.12 Solubility and concentration lines of maleic acid measured with respect to the peak shift of the v(C=C) vibrational mode, in situ. In addition, solubility was measured in a slurry. Absolute peak positions at two conditions are shown for reference purposes.

the $\nu(C=C)$ vibration are not documented. Nevertheless, this data suggest that the strength of the C=C bond or the force constant of the $\nu(C=C)$ stretching vibration is reduced upon approaching the onset of nucleation.

Solubility and concentration lines of aqueous maleic acid with respect to the peak shift of the $\delta(O-H)$ in-plane deformation vibration measured in situ are shown in Figure 4.13. The behavior of the $\delta(O-H)$ peak shift upon approaching conditions that favor a higher degree of association, in this case lower temperatures, is similar to that of the $\nu(C-O)$ peak as has been documented [3, 9]. The $\nu(C-O)$ and the $\delta(O-H)$ modes are mutually coupled and blue shifts upon association via H-bonding [3, 9].

The peak shifts of v(C=O), v(C=O), v(C=C) and δ (O-H) vibrations were isolated using derivative spectroscopy. A common feature of these bands is that they have relatively narrow band widths that give rise to informative derivative profiles. However, the derivative profiles of the highly convoluted, broad v(O-H) stretching vibration region are not conducive to meaningful analysis. In the case of aqueous maleic acid, the v(O-H) stretching region constitutes of contributions from both water and acid. In addition, the v(C-H) stretching mode coincide in this region [9]. The relative changes in this region are shown in Figure 4.14. However, subtle features such as peak shifts are not quite detectable. Isolation of the contributing components via deconvolution of the broad, convoluted band can reveal the concealed information.

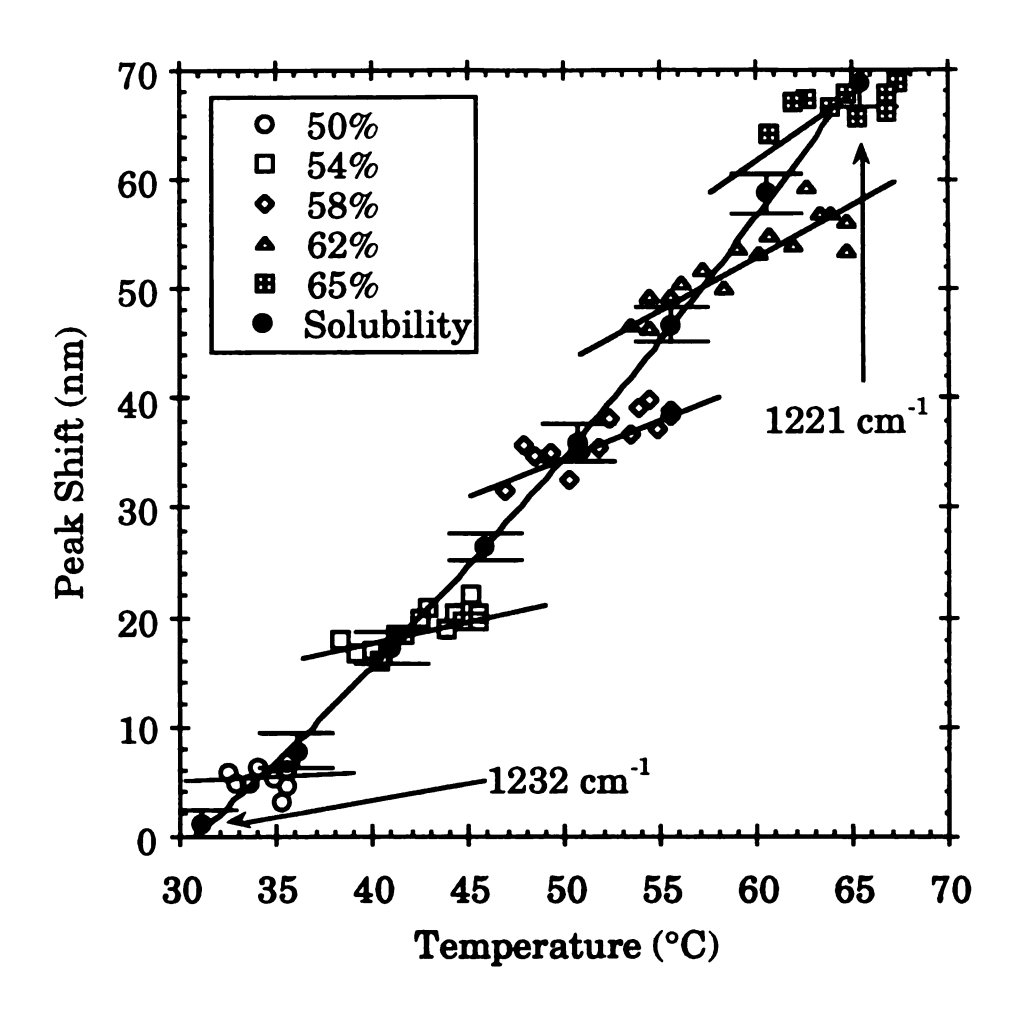


Figure 4.13 Solubility and concentration lines of maleic acid measured with respect to the peak shift of the δ (O-H) vibrational mode, in situ. In addition, solubility was measured in a slurry. Absolute peak positions at two conditions are shown for reference purposes.

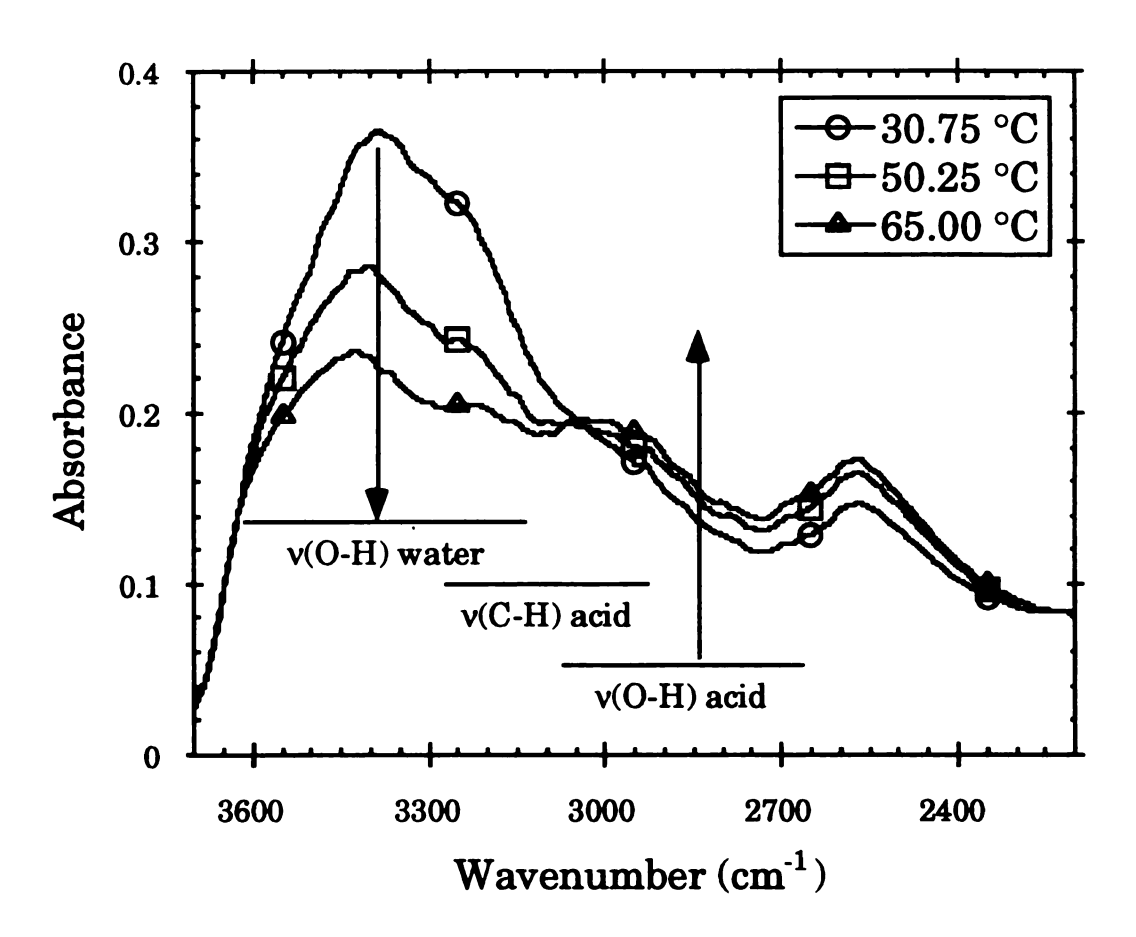


Figure 4.14 In situ, slurry ATR FTIR spectra of aqueous maleic acid at saturation in the high frequency region.

Deconvolution algorithms are available in some FTIR instrument software packages. However, they are designed to enhance existing peaks. They are not adequate for resolving highly convoluted, broad bands. An alternative is to fit the spectral profile in this region to a multicomponent Gaussian function using a least squares minimization algorithm. A rule of thumb that is generally applicable in utilizing this technique is to use the least number of Gaussian components that provide the best fit for the spectral profile. Consider the spectrum at solubility at 30.75 °C over the 2700 - 3700 cm⁻¹ range (Figure 4.14). The normalized and baseline adjusted spectrum was fit to a function consisting of six Gaussian components. The results are given in Figure 4.15. Due to the closeness of the fit, the spectrum and the six component function used for the fit are not distinctly identifiable in the figure. The six isolated components are also shown. The components toward the high frequency side of the band can be loosely assigned to the v(O-H) stretching bands of water. Conversely, the components toward the low frequency side of the band can be loosely assigned to the v(O-H) stretching bands of maleic acid. The assignments are not meant to be definitive because the contributions from the v(C-H)stretching vibration of maleic acid to both v(O-H) stretching band intensities cannot be discounted. However, the general trends of the components can be used within the scope of this investigation. For example, it is reasonable to associate most of the peak shifts observed in individual components to the influence of H-bonding on the v(O-H) stretching vibrations. As a result of

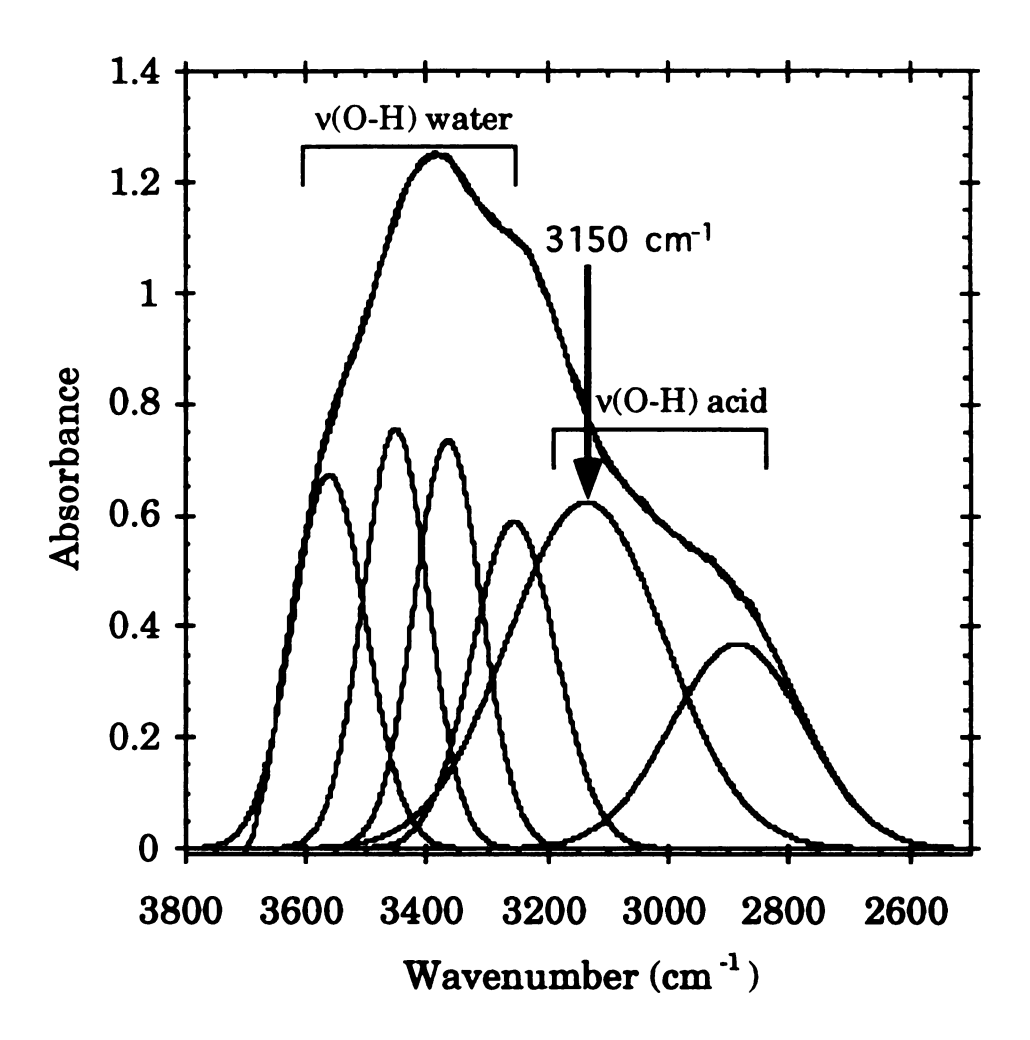


Figure 4.15 Gaussian components of the v(O-H) region. Due to the closeness of the fit the original spectral profile (normalized and baseline corrected spectrum at saturation at 30.75 °C from Figure 4.14) and the six component Gaussian function used for the fit are superimposed.

the transition from the monomeric to the associated form, a large decrease in frequency of the $\nu(O-H)$ vibration of carboxylic acids is observed due to the exceptional strength of hydrogen bonds [3, 4]. The same trend is expected to continue in highly concentrated solutions where strengthening H-bonds play a critical role in the organization of carboxylic acid molecules.

Consider the component identified at 3150 cm⁻¹ in Figure 4.15. Its peak shift is shown in Figure 4.16. As discussed in the previous paragraph, the peak shift was associated with the v(O-H) stretching vibration of maleic acid. The peak shift of the low frequency side of the v(O-H) band is clearly demonstrated by the considered component whereas it is not evident in the original spectra. Solubility and concentration lines of aqueous maleic acid with respect to the peak shift of the v(O-H) vibration measured in situ are shown in Figure 4.17. When solutions at all concentrations are cooled, the v(O-H) stretching vibration is expected to demonstrate a red shift toward lower frequencies under the influence of strengthening H-bonds. The concentration lines appear to have slight negative gradients as expected. However, due to the complexity of this region it is not possible to provide a definitive interpretation.

Overall, all the peaks characteristic of maleic acid shift in the direction that suggests a greater degree of association of the molecules (via H-bonding) upon cooling. These trends observed in supersaturated solutions in approaching the onset of nucleation, is consistent with the trends observed in the transformation from the monomeric form to the associated

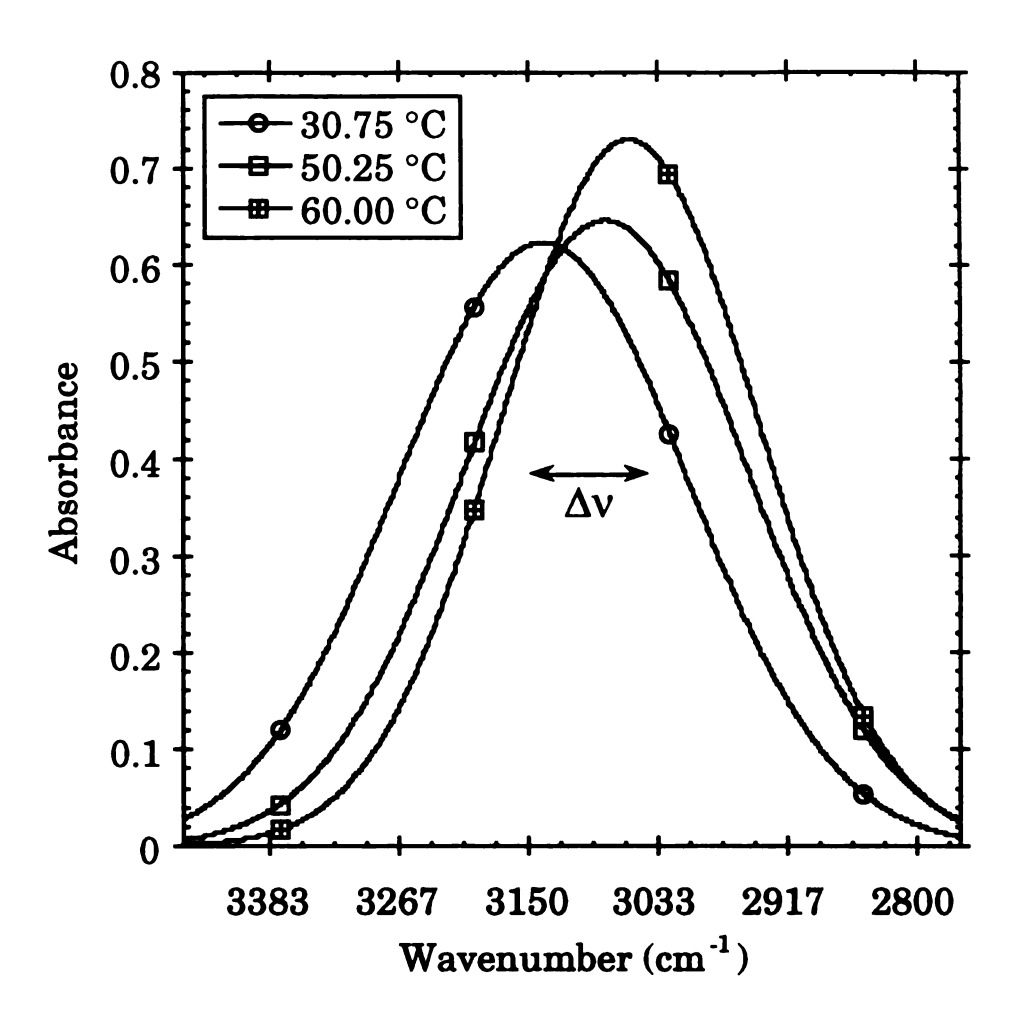


Figure 4.16 Peak shift of the component near 3150 cm⁻¹ from Figure 4.15.

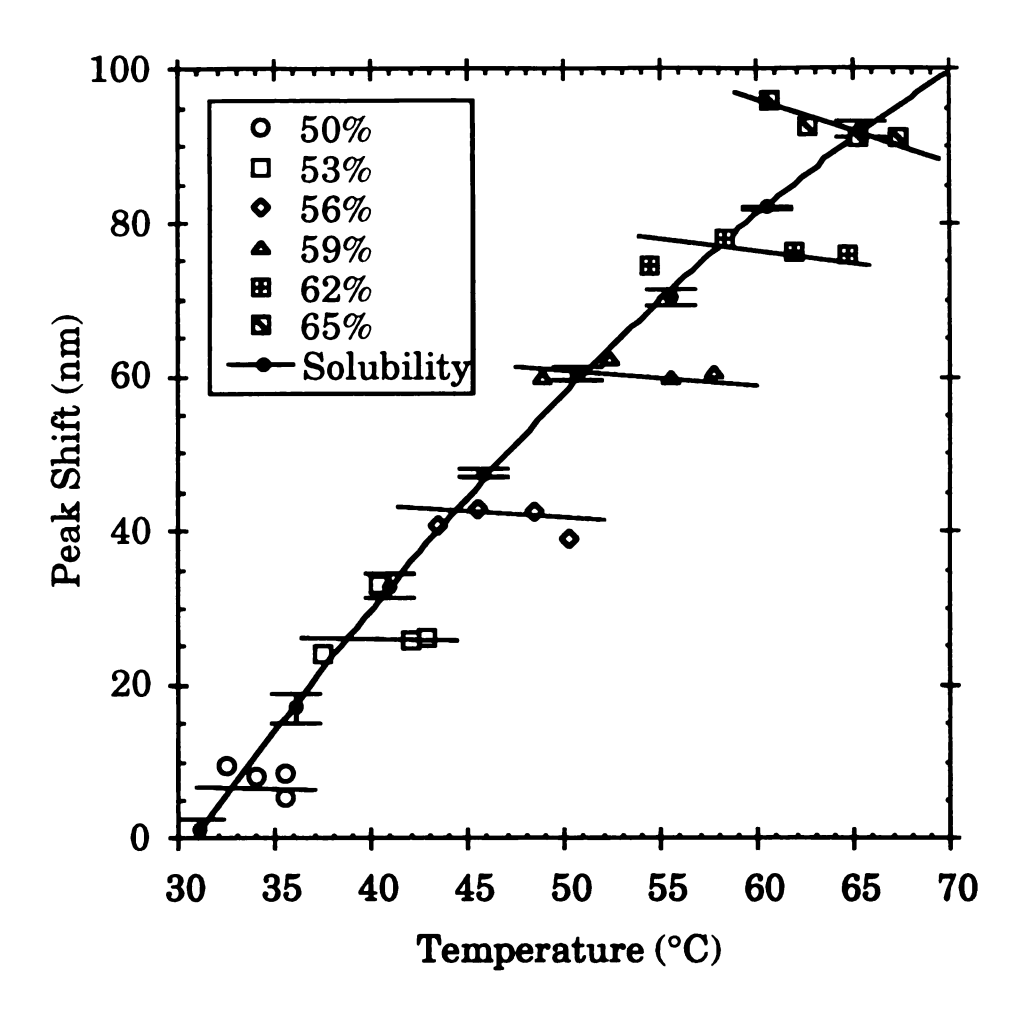


Figure 4.17 Solubility and concentration lines of maleic acid measured with respect to the peak shift of the $\nu(O-H)$ vibrational mode, in situ. In addition, solubility was measured in a slurry.

form in more dilute solutions. In addition, all peaks approach the peak positions of the solid state spectrum. While recognizing that this evidence alone is not sufficient to provide conclusive remarks regarding the similarity of the solid state and the solution (supersaturated) state molecular structure, it is not unreasonable to suggest that the molecular structure in the two states are most likely similar considering the convergence of peak positions and the evidence [5] for the folded configuration of maleic acid in solution.

A concrete analysis on the nature of the solution state structure of aqueous maleic acid in supersaturated solutions is beyond the scope of this investigation. This analysis is a prelude to a more in-depth study that will involve both Raman and NMR spectroscopy in addition to FTIR The different techniques can reveal complementary spectroscopy. information. Further, utilization of the deutero analogues of both water and maleic acid in experiments similar to ones discussed above can provide a host of confirmatory information [10, 11, 22]. The deuteration of a particular bond results in a significant red shift in its vibrational frequencies due to the heavy atom effect. For example, the v(O-D) vibration of the deuterated acetic acid is observed at 2299 cm⁻¹ in comparison to the v(O-H)vibration of acetic acid that occurs at 3140 cm⁻¹ [10]. The δ(O-D) vibration is observed at 1046 cm⁻¹ compared to the δ(O-H) vibration at 1294 cm⁻¹. Consequently, experimentation with selectively deuterated maleic acid and deuterated water in judiciously chosen combinations can help resolve many of the ambiguities of the current analysis. For example, use of maleic acid in heavy water will clear the v(O-H) stretching region of any contribution from the v(O-H) vibration of water thus making it much easier to identify dynamics of the v(O-H) vibration of maleic acid.

Thus far, a discussion of the utility of the peak shifts of maleic acid vibrational modes for the measurement of crystallization parameters of aqueous maleic acid, which incidentally is the primary objective of this investigation, has been neglected. The discussion has been centered on providing some insight to the organization of maleic acid in supersaturated solutions. However, maleic acid vibrational modes suitable for measurement of supersaturation and solubility are quite evident. The $\nu(C=C)$ mode (Figure 4.12), the $\delta(O-H)$ mode (Figure 4.13) and the $\nu(O-H)$ mode (Figure 4.17), that demonstrate a strong dependence on concentration, are the ones suitable for this purpose. The other modes that are independent of concentration, although reflective of the solution structure, are clearly not useful for quantitative measurements.

Between the band ratioing techniques investigated in Chapters 1 and 2 [16, 18] and discussed herein and the peak shifts of numerous vibrational modes, it is anticipated that it will not be a difficult task to identify a parameter appropriate for measurement of crystallization phenomena of most inorganic and organic systems. As indicated above, features of infrared spectra otherwise suitable for quantitative measurements of many other crystallization systems can be masked by the presence of various species such as impurities, byproducts, additives and solvents that have strongly absorbing vibrational modes. Upon encountering such a system,

the techniques discussed herein can be used to help enhance features toward identifying a parameter suitable for measurement of solubility and supersaturation. In the case of maleic acid many options that are equally effective are available. The solubility measured with respect to each of the options discussed above is shown in Figure 4.18. The precision of the data is quite reasonable considering the diversity of the parameters used to extract them.

In Chapter 1, an inconsistency between the solubility data extracted from two different ratios $(RT_1 \text{ and } RT_2)$ was attributed to the optical properties and the material of the ATR configuration of the Micro CIRCLE® Open Boat Cell. It was postulated that the deeper penetration of the evanescent field into the sample at longer wave lengths (RT_2) may have been responsible for this anomaly. It was also pointed out that the depth of penetration can be reduced by using alternate ATR configurations and ATR elements that have higher refractive indices such as AMTIR-1 crystals. In the feasibility study presented in Chapter 1, the ATR element used was a cylindrical, ZnSe rod that has a low refractive index. In addition, the Micro CIRCLE® Open Boat Cell is a sampling device that may allow settling of slurries over the ATR rod leading to inconsistencies in accumulated data. In the studies undertaken subsequently and presented in Chapter 2 and here. the ATR element used was a conical, AMTIR-1 ATR crystal that has a higher refractive index configured for *in situ* measurements. It is very likely that the combination of in situ measurements, the conical ATR configuration and the AMTIR-1 ATR element with a higher refractive index

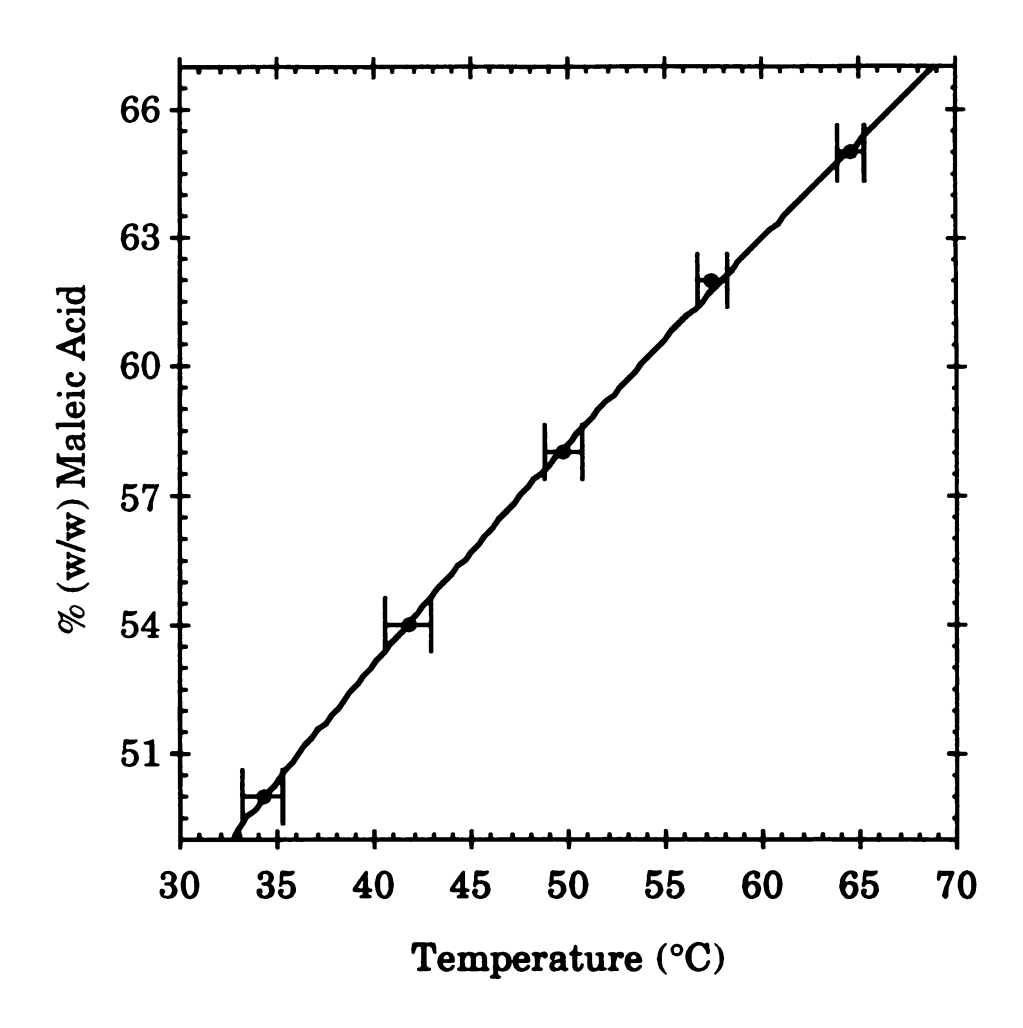


Figure 4.18 Solubility of maleic acid in water with respect to % maleic acid (w/w).

contributed to the consistency of the data extracted from the diverse set of IR parameters.

Not all parameters considered were suitable for measurement of supersaturation as a result of some being independent of concentration. The existence of a clear distinction between parameters in terms of the dependence on concentration may be indicative of the unique structure of aqueous maleic acid. For example, consider PIR₁ and PIR₂ that were extracted from the v(C=0) peak. PIR_1 is independent of concentration. Conversely, PIR₂ is dependent on concentration. This may be indicative of the carbonyl bond being influenced by two types of H-bonds as illustrated in Figure 4.9. Evidence suggests that the folded structure of the maleic acid molecule in the crystalline state - due to intramolecular H-bonding - stays intact upon dissolution in concentrated solutions (0.3M) [5]. Consequently, the two carbonyl bonds of maleic acid in solution are most likely affected by both intramolecular and intermolecular H-bonding. Therefore, it can be postulated that the nature of the carbonyl bonds is manifested in the spectra as two mutually exclusive features, one independent (PIR_1) and the other dependent (PIR_2) on concentration. Again, such phenomena cannot be confirmed without other corroborative evidence by way of Raman and NMR spectroscopic data and experimental data using deuterated analogues of water and maleic acid. However, the broad scope of ATR FTIR spectroscopy for measurement of vital crystallization parameters and understanding crystallization systems is indisputable.

4.4 Conclusions

The primary focus of this paper was to investigate the methods available to identify and isolate subtle features of IR spectra for utilization in measurement of crystallization parameters. Both derivative spectroscopy and deconvolution were successfully used to reveal features otherwise obscured by spectral artifacts. These features were primarily useful for quantitative measurements. The precision of the solubility measurements extracted from numerous IR parameters established the consistency of IR spectroscopy toward measurement of crystallization parameters. It is our firm belief that the techniques discussed herein can be used to help enhance features of many organic or inorganic crystallization systems toward identifying a parameter suitable for measurement of solubility and supersaturation. In addition to the versatility of ATR FTIR spectroscopy as a measurement tool, the spectra can be abundant with information that would provide some insight to the chemical nature of various systems.

4.5 References

- 1. Avram, M., Mateescu, GH. D., "Infrared Spectroscopy:Applications in Organic Chemistry", Wiley-Interscience, New York, New York, (1966), Ch.7.
- 2. Hadzi, D., Bratos, S., in: "The Hydrogen Bond", Eds. Schuster, P., Zundel, G., Sandorfy, C., North-Holland, New York, New York, (1976), Ch. 12.
- 3. Davies, M., Sutherland, G. B. B. M., J. Chem Phys., 6, (1938), 755.
- 4. Hadzi, D., Chimia, 26, (1972), 7.

- 5. Hadzi, D., Novak, A., Spectrochim. Acta., 18, (1962), 1059.
- 6. Lascombe, J., Haurie, M., Josien, M. L., J. Chim. Phys., (1962), 1233.
- 7. Flett, M. St. C., Trans. Faraday Soc., 44, (1948), 767.
- 8. Weltner Jr., W., J. Am. Chem. Soc., 77, (1955), 3941.
- 9. Flett, M. St. C., J. Chem. Soc., (1951), 962.
- 10. Kishida, S., Nakamoto, K., J. Chem. Phys., 41:6, (1964), 1558.
- 11. Fukushima, K., Zwolinski, J., J. Chem. Phys., 50:2, (1969), 737.
- 12. Millikan, R. C., Pitzer, K. S., J. Am. Chem. Soc., 80, (1958), 3515.
- 13. Davies, M., Evans, J. C, J. Chem Phys., 20, (1952), 342.
- 14. Grove, J. F., Williams, H. A., J. Chem. Soc., (1951), 877.
- 15. Hadzi, D., Sheppard, N., Proc. Roy. Soc., London, A216, (1953), 247.
- 16. Dunuwila, D. D., Berglund, K. A., Revised for publication in *Ind. Eng. Chem. Fundamentals*, (1995).
- 17. Perkin Elmer IR Data Manager, User's Manual, (1991).
- 18. Dunuwila, D. D., Carroll II, L. B., Berglund, K. A., *J. Cryst. Growth*, **137**, (1994), 561.
- 19. Badger, R. M., Bauer, S. H., J. Chem. Phys., 5:11, (1937), 839.
- 20. James, M. N. G., Williams, G. J. B., Acta. Cryst., B30, (1974), 1249.
- 21. The Aldrich Library of FT-IR Spectra, Vol. 1, Aldrich Chemical Company, Inc., Milwaukee, USA.
- 22. Bratoz, S., Hadzi, D., Sheppard, N., Spectrochim. Acta., 8, (1956), 249.

CONTINUING INVESTIGATIONS

5.1 Background

5.1.1 Control Strategy

It **Definition of Supersaturation:** has been observed that maintenance of constant supersaturation during a crystallization process leads to improved crystal size distributions [1]. Supersaturation is defined in terms of the fundamental properties of solutions as given in Equation 2.6 of Chapter 2. However, for all practical purposes, supersaturation is approximated by the concentration difference or ratio with respect to the solubility with the underlying assumption of ideality [2]. This assumption is valid for sparingly soluble systems. For highly soluble systems, the approximation can lead to substantial misrepresentation of supersaturation due to increased nonideality of the solution.

Generally, nonideal behavior of concentrated solutions, reflected by the activity coefficient (γ) , is due to extensive intermolecular and intramolecular interactions between the solute and the solvent. These interactions in turn configure the solution structure of the system. Then, it follows that the activity coefficient is reflective of the solution structure at a molecular level. Therefore, a method for determining supersaturation that is reflective of the solution structure would be inherently more accurate. Conventional techniques such as refractometry, interferometry, viscometry

and densitometry, in addition to being unsuitable for in situ measurements, can measure only their respective bulk properties which are not sensitive to solution structure at a molecular level. In addition, conventional methods are not sensitive enough and their use can lead to gross misrepresentation of supersaturation. Conversely, infrared spectroscopy, which probes the vibrational structure of molecules is reflective of the solution structure and therefore is a viable technique to measure supersaturation reflective of solution activity. In Chapter 4, parameters sensitive to solution structure and supersaturation were distinguished from those that were sensitive to solution structure and not supersaturation, highlighting the specificity of IR spectroscopy. Further, the sensitivity of IR parameters (reflected by the signal gain) over a broad operating region was demonstrated in Chapter 4. Therefore, conceivable definitions for supersaturation include;

$$\Delta(P_{IR}) = P_{IR} - P_{IR,sol} \text{ and}$$

$$\delta(P_{IR}) = \frac{P_{IR}}{P_{IR,sol}}$$
(5.1)

where P_{IR} is any parameter discussed in Chapters 2, 3 and 4 in the context of measurement of supersaturation and solubility and $P_{IR,sol}$ is the solubility with respect to P_{IR} . Since P_{IR} is a parameter that reflects the fundamental structure of the solution, $\Delta(P_{IR})$ and $\delta(P_{IR})$ will most likely contribute to a more accurate measurement of supersaturation. The sensitivity and the potential accuracy provided by $\Delta(P_{IR})$ and $\delta(P_{IR})$ is anticipated to contribute toward the performance of a control scheme. It is also a direct measurement of supersaturation that does not require calibrations and therefore more practical. In effect, a set point for a control scheme designed

to obtain a crystal size distribution (CSD) with a large average size can be envisioned as;

$$\Delta(P_{IR}) = \text{constant}, \quad \text{or}$$

$$\delta(P_{IR}) = \text{constant}$$
(5.2)

which is illustrated in Figure 5.1.

One of the primary objectives in controlling a crystallization process is to obtain a specified CSD. Excessive nucleation occurs when the system approaches its metastable limit [3] resulting in CSDs with smaller average sizes. Therefore, if a larger average size is desired, it is imperative that the system is maintained well within the metastable zone; i.e., away from the limit. However, it is counterproductive to operate very close to the solubility line since this does not provide sufficient driving force for growth resulting in unacceptably long batch times.

Closed Loop Batch Crystallizer Control: A simple schematic of a batch crystallizer and the primary components of the envisioned control system is shown in Figure 5.2. The system consists of a jacketed crystallizer where a coolant fluid enters its jacket at temperature T_i and exits at T_o . The flow rate is denoted by w. Supersaturation in the crystallizer measured by in situ ATR FTIR spectroscopy - $\Delta(P_{IR})$ or $\delta(P_{IR})$ - is measured and transmitted to the primary controller, E, which in turn adjusts the heat removal system, B, accordingly. In order to compensate for fluctuations in the heat removal system, a secondary controller, D, is suggested [4]. In this configuration, the heat flux, \dot{H} , from the crystallizer measured by T_i , T_o and w is transmitted to the secondary controller which compensates for the fluctuations. Without a secondary controller, any fluctuation in the heat removal system

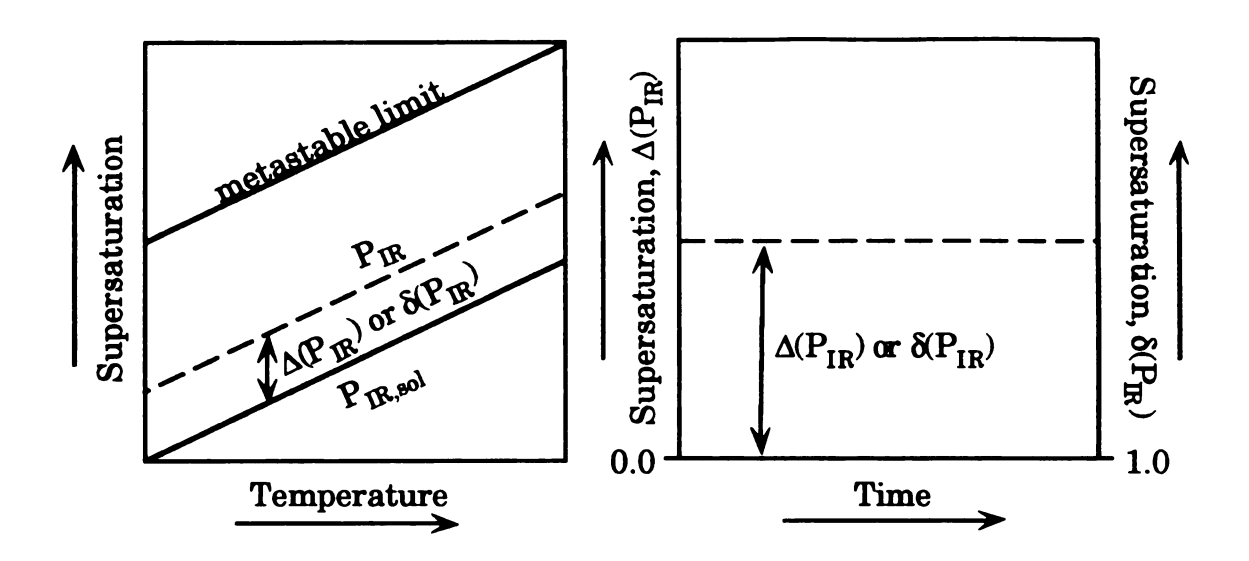


Figure 5.1 Control policy projected to maximize the mean size of a crystal size distribution from a cooling batch crystallization process. The policy is based on maintaining a constant supersaturation defined by the IR parameters given by $\Delta(P_{IR})$ or $\delta(P_{IR})$.

$$\Delta(P_{IR}) = P_{IR} - P_{IR,sol} \text{ and}$$

$$\delta(P_{IR}) = \frac{P_{IR}}{P_{IR,sol}}$$

where P_{IR} is any parameter discussed in Chapters 2, 3 and 4 in the context of measurement of supersaturation and solubility and $P_{IR,sol}$ is the solubility with respect to P_{IR} .

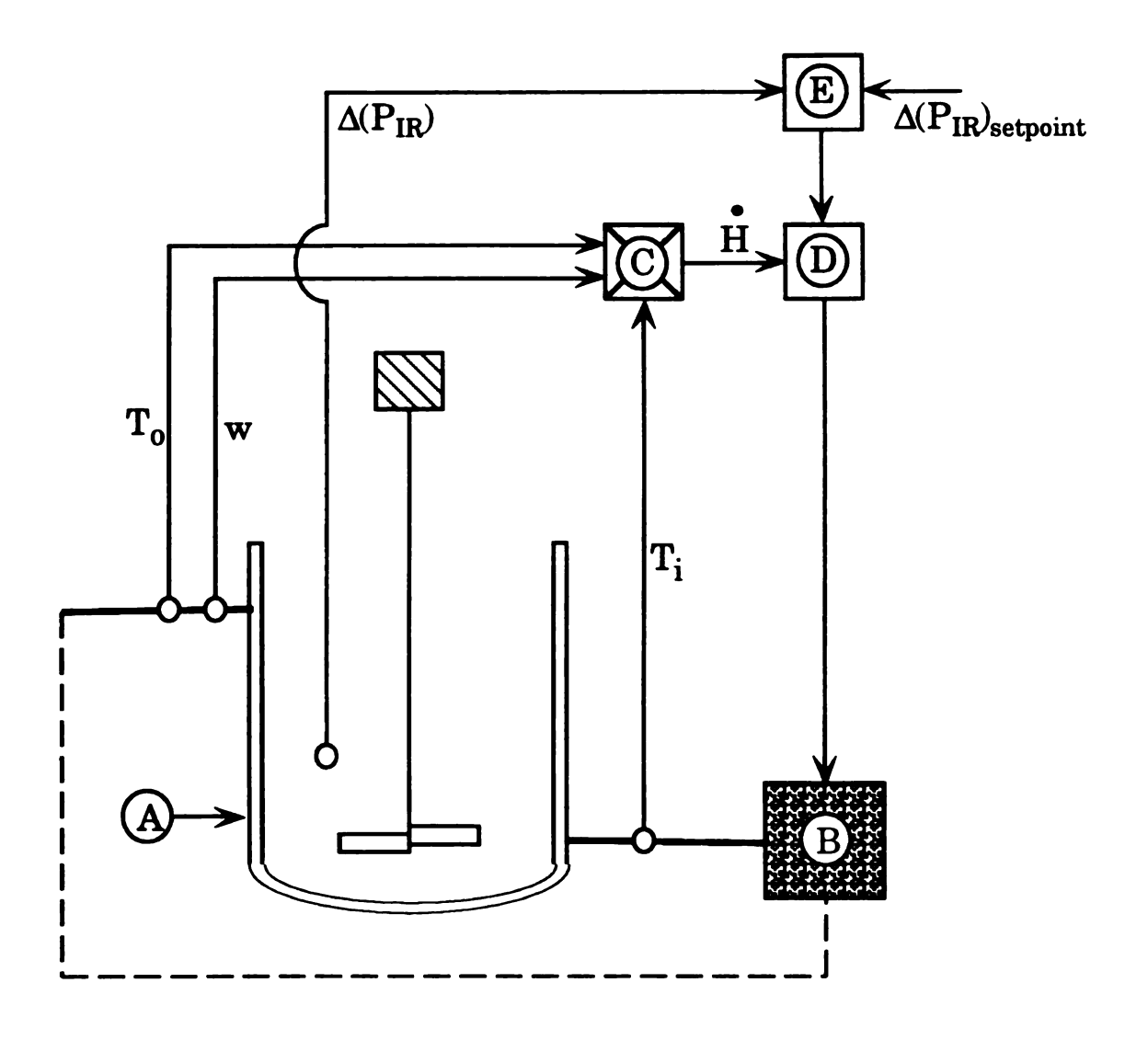


Figure 5.2 A simple schematic of a batch crystallizer and the primary components of the envisioned control system.

 T_i = Inlet coolant temperature of the jacketed crystallizer,

 $T_o = \text{Outlet coolant temperature}, w = \text{Coolant flow rate},$

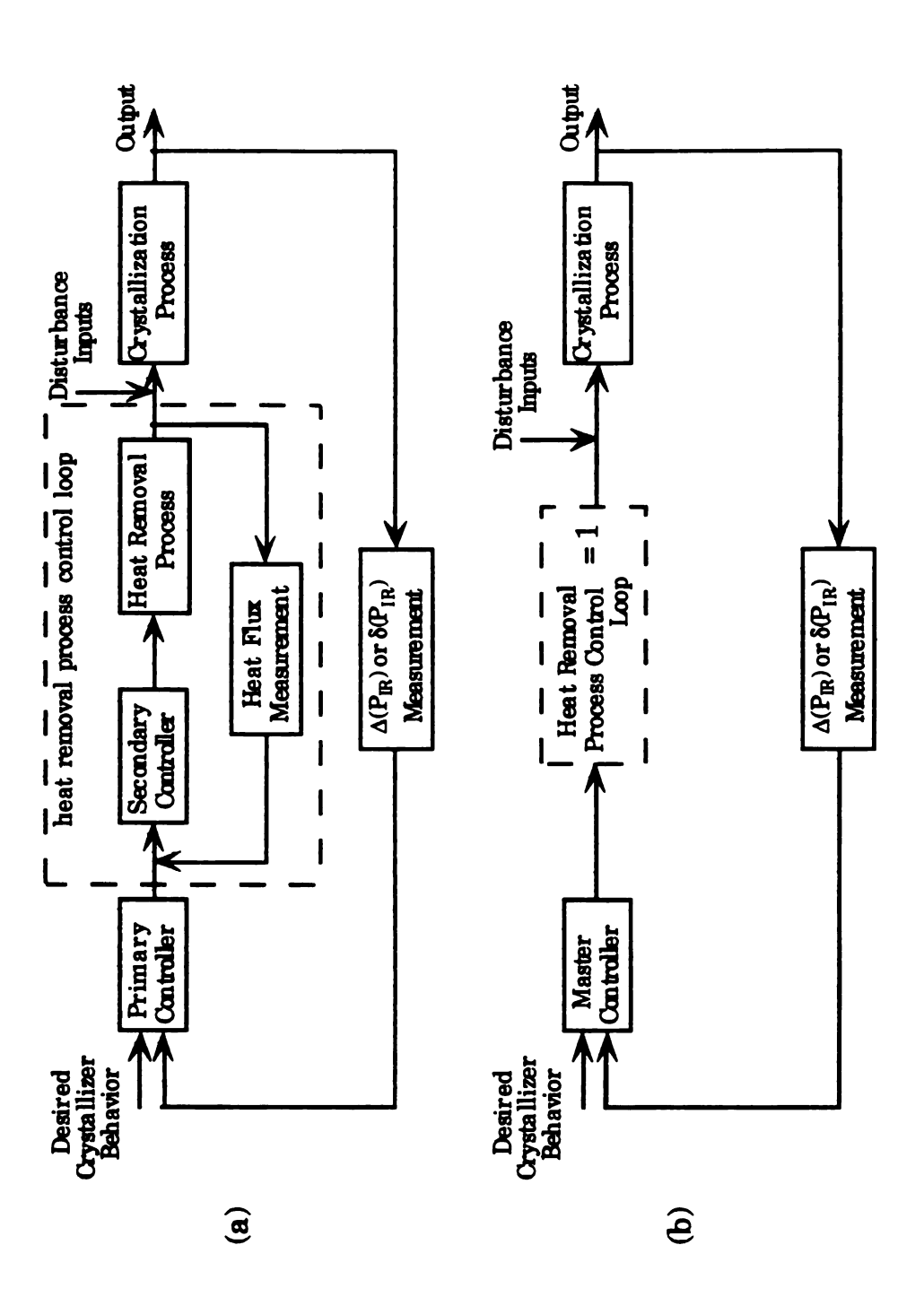
 $\Delta(P_{IR})$ = Supersaturation, E = Primary controller

B = Heat removal system, D = Secondary controller

 $\dot{\mathbf{H}}$ = Heat flux from the crystallizer measured by T_i , T_o and w.

can lead to a prolonged excursion in supersaturation from its setpoint. The reason for this is that the primary controller, without the aid of a secondary controller, does not take any corrective action until the disturbance is transmitted through the system consisting of several resistances. In the secondary control loop, heat flux from the crystallizer is used as the measured variable as opposed to measuring the temperature in the crystallizer since heat flux control has been proven to provide more stable control systems [5]. The block diagram of the cascade control system is given in Figure 5.3 (a).

Although, a good heat removal system is tantamount to the stable operation of the overall control scheme, its design is not expected to be a limiting factor considering the resources available for its design [6]. Therefore, the heat removal system is not specified. The task more substantial in terms of relevancy and more challenging will be the design of the primary loop controlling supersaturation. In order to consummate the goal of designing a stable supersaturation control scheme (primary loop), it is not necessary to know the dynamics of the secondary loop, since the two loops can be analyzed independent of each other. The standard procedure in designing cascade control systems is to first establish the control dynamics for a stable secondary loop. Subsequently, the secondary loop can be normalized to determine the stability of the primary loop. demonstrated between Figures 5.3 (a) and 5.3 (b). However, in this case its reasonable to consider normalizing the secondary loop for heat flux control without specifying the heat removal system taking comfort in the resources available for its design in terms of hardware, literature and specialists.



Block diagrams of the cascade control system. The normalized heat removal secondary loop is illustrated in (b). Figure 5.3

Thus, the hitherto unventured, yet promising aspect of crystallizer design and control, which is design and control based on *in situ* measurement of supersaturation, can be promptly attended to as it is more relevant to and more substantial in the field.

One concern in using in situ ATR FTIR spectroscopy for control of batch crystallization processes may be whether the frequency of measurement would be sufficient for implementation in control of a highly labile process such as batch crystallization. The scan rate of the supersaturation profiles presented in Chapter 3 (Figures 3.5 and 3.7) was 0.05 sec⁻¹. In fact, the desupersaturation of aqueous citric acid, which is one of the fastest growing systems known, was measured with remarkable point to point resolution and is shown in Figure 5.4. Desupersaturation of aqueous citric acid was measured using a protocol similar to that used with maleic acid at a scan rate of 0.008 sec⁻¹. The citric acid solution was not seeded. In view of a control scheme with high performance, a scan rate of 0.1 sec⁻¹ is realizable. Clearly, the data suggest that the frequency of measurement will not be a limiting factor in the development of a control scheme.

Crystallization Model: The particle number-size distribution theory introduced by Randolph and Larson [7] and the fundamental supersaturation balance discussed by Mullin and Nyvlt [8, 9, 10] provide powerful models to evaluate crystallization processes. The model derived from the particle number-size distribution theory is based on the population balance (number of particles per unit volume per length range) and takes nucleation and growth of crystals into account. The fundamental supersaturation balance is derived taking into consideration that the driving

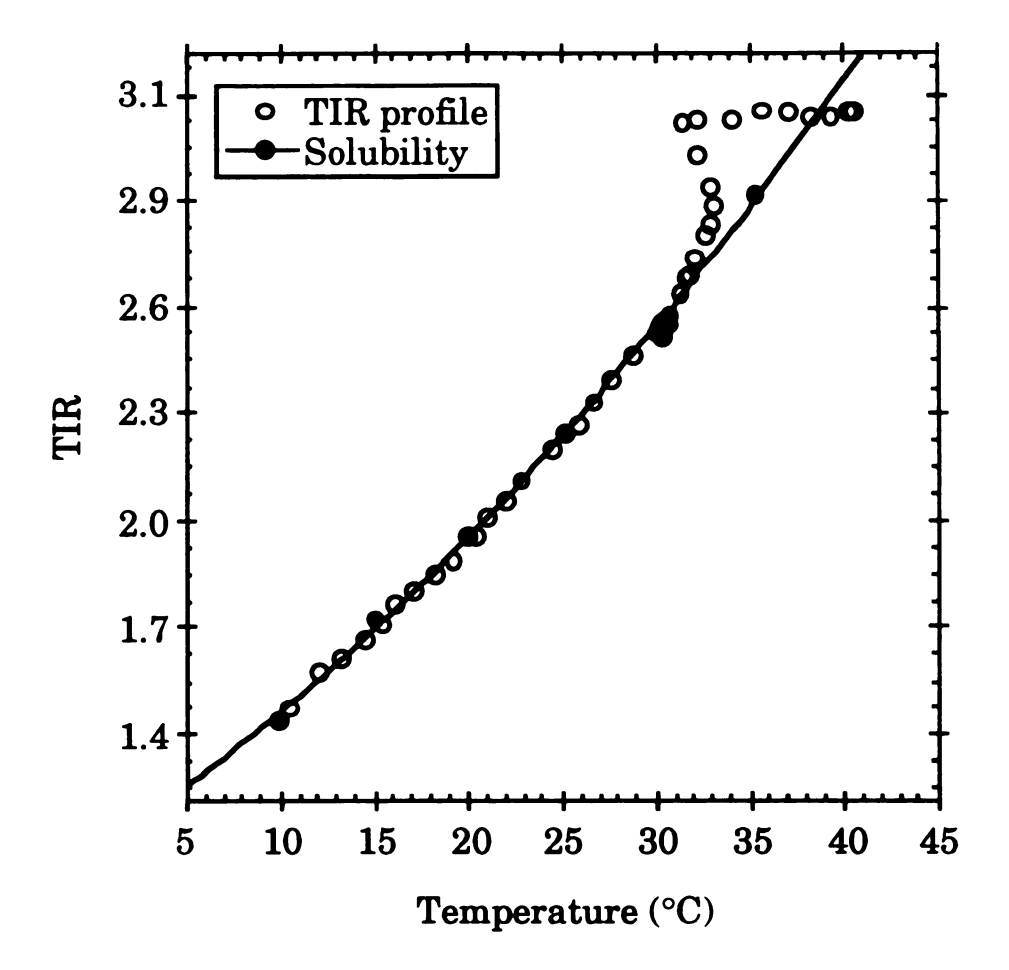


Figure 5.4 A supersaturation profile of aqueous citric acid represented in terms of *TIR*.

 $TIR = \frac{\text{transmittance at 3284 cm}^{-1}}{\text{transmittance at 1190 cm}^{-1}}$

force for all crystallization phenomena such as nucleation and growth is supersaturation. Thus, kinetic parameters for nucleation and growth are nested in these models giving them both predictive and descriptive capabilities. Another valuable set of equations commonly used in crystallization analysis is the moments of the particle number-size distribution [7]. The moments have been utilized to circumvent a basic dimensional incompatibility between the population balance and the transport equations for mass, momentum and energy.

The particle phase space consists of a set of internal coordinates in addition to the three spatial dimensions. This incompatibility complicates the simultaneous solution of the population balance with the transport equations. The most significant internal coordinate in the particle phase space is the particle size. Therefore, the population density distribution is integrated over the particle size internal coordinate reducing the dimensionality of the population balance to that of the transport equations. The moments that give the total particle properties (presented shortly) upon integrating the population balance over the particle size coordinate are given by:

$$m_j(t) = \int_0^\infty n(L, t)L^j dL, \quad j = 0, 1, 2, ...$$
 (5.3)

where n is the population density distribution and L is the particle size.

The application of these models in engineering simulations and process analysis and control has been limited by the unavailability of a reliable and sensitive technique to obtain kinetic data *in situ*. In crystallization processes, *in situ* measurement is extremely important since

the hydrodynamic conditions set by the crystallizer dimensions, flow patterns induced by the propeller and the suspended crystal slurry can significantly alter kinetic parameters from that obtained under controlled laboratory experiments [11]. Theoretically, kinetic parameters can be extracted from the desupersaturation rate of the solution monitored by in situ ATR FTIR spectroscopy. An attempt was made to extract the crystallization kinetic parameters of aqueous maleic acid by least squares minimization between the measured supersaturation profile and the supersaturation profile calculated using the supersaturation balance which has a structure similar to the moment equations. Crystallization is a particulate process where the number of particles generated over the batch time plays a significant role in affecting the course of the process. Therefore, it was extremely difficult to obtain a consistent set of crystallization kinetic parameters using supersaturation alone since it does not provide number related information. It is anticipated that in situ measurement of supersaturation using ATR FTIR spectroscopy and measurement of the transient CSD using a light scattering device in combination will be a more promising approach for the estimation of kinetic parameters. The model most convenient for the extraction of kinetic parameters using supersaturation measurements and CSD measurements is the set of moment equations [7].

The population balance for a well mixed, constant volume batch crystallizer is given by;

$$\frac{\partial n}{\partial t} + \frac{\partial (Gn)}{\partial L} = 0 \tag{5.4}$$

where G is the linear growth rate of crystals. In order to obtain the moments of the distribution, the population balance is integrated over the particle size coordinate as follows;

$$\int_{0}^{\infty} \left[\frac{\partial n}{\partial t} + \frac{\partial (Gn)}{\partial L} = 0 \right] L^{j} dL, \qquad j = 0, 1, 2, \dots$$
 (5.5)

The resulting set of moments are given by;

$$\frac{\mathrm{d}m_j}{\mathrm{d}t} - 0^j B^o = jGm_{j-1}, \quad j = 0, 1, 2, \dots$$
 (5.6)

where 0' = 0 for $j \neq 0$. The time dependent moments are as follows;

$$\frac{dm_0}{dt} = \frac{dN_n}{dt} = B^0$$

$$\frac{dm_1}{dt} = \frac{dL}{dt} = [m_0 + N_s]G$$

$$\frac{dm_2}{dt} = \frac{1}{k_a} \frac{dA}{dt} = 2m_1G$$

$$\frac{dm_3}{dt} = \frac{k_a}{k_v \rho_c} \frac{dM}{dt} = 3m_2G$$

$$\frac{dm_4}{dt} = 4m_3G$$
(5.7)

where the number rate of nucleation, B^{o} , the number of seeds, N_{s} , and the linear crystal growth rate, G, are defined in terms of the frequently used power model as;

$$B^{0} = \frac{1}{k_{\nu}\rho_{c}L_{n,0}^{3}} \left[k_{n,p}\Delta(P_{IR})^{n_{p}} + k_{n,s}M^{m}\Delta(P_{IR})^{n_{s}} \right]$$

$$G = \frac{k_{a}}{3k_{\nu}\rho_{c}} k_{g}\Delta(P_{IR})^{g}$$

$$N_{s} = \frac{W_{s,0}}{k_{\nu}\rho_{c}L_{s,0}^{3}}$$
(5.8)

where N_n is the total number of nuclei, L is the total length of crystals, A is the total area of crystals, M is the total mass of crystals in suspension, k_a is

the area shape factor, k_v is the volume shape factor, ρ_c is the crystal density, $L_{n,0}$ is the size of nuclei at birth, $L_{s,0}$ is the initial size of seed crystals, $W_{s,0}$ is the initial mass of seed crystals, $k_{n,p}$ is the primary nucleation rate constant, $k_{n,s}$ is the secondary nucleation rate constant, k_g is the growth rate constant, n_p is the order of primary nucleation, n_s is the order of secondary nucleation and g is the order of growth. In order to solve the moment equations, the operating conditions should be defined and the mass balance should be specified. The mass balance is specified as:

$$\frac{\mathrm{d}\Delta(P_{IR})}{\mathrm{d}t} = -\frac{\mathrm{d}P_{IR,sol}}{\mathrm{d}t} - \frac{\mathrm{d}M}{\mathrm{d}t}$$
 (5.9)

The time dependent population density distribution can be recovered by the following approximation [7];

$$n(L) = \mathbf{A}^{-1}\mathbf{m} \tag{5.10}$$

where \mathbf{m} is the moment vector and the elements of the matrix \mathbf{A} is given by;

$$a_{jk} = L_k^j \Delta L_k \tag{5.11}$$

where L_k is the midpoint of a size range ΔL_k . It has been shown that four to five moments satisfactorily reproduce an original distribution [7]. The higher moments unduly weight the distributions toward the larger sizes.

Control System Equations; State Variable Form: State variable form is particularly convenient for the description of complicated systems for which a standard, compact notation is especially helpful [12]. The state representation of systems, that uses integrators, is useful not only in control system analysis, but for simulation and analysis of systems of all kinds. A state variable description of an nth-order system, in the Laplace domain,

involves n integrators and the corresponding outputs which are the state variables. The inputs of each of the integrators is given as a linear combination of the state signals, X_n , and the system inputs, R_i ;

$$\begin{split} \mathbf{s}X_{1}(s) &= a_{11}X_{1}(s) + a_{12}X_{2}(s) + \ldots + a_{1n}X_{n}(s) + b_{11}R_{1}(s) + \ldots + b_{1i}R_{i}(s) \\ \mathbf{s}X_{2}(s) &= a_{21}X_{1}(s) + a_{22}X_{2}(s) + \ldots + a_{2n}X_{n}(s) + b_{21}R_{1}(s) + \ldots + b_{2i}R_{i}(s) \\ &\vdots \\ \mathbf{s}X_{n}(s) &= a_{n1}X_{1}(s) + a_{n2}X_{2}(s) + \ldots + a_{nn}X_{n}(s) + b_{n1}R_{1}(s) + \ldots + b_{ni}R_{i}(s) \end{split}$$

$$(5.12)$$

In the time domain these are a set of n first-order linear differential equations;

$$\frac{dx_1}{dt} = a_{11}x_1 + a_{12}x_2 + \dots + a_{1n}x_n + b_{11}r_r + \dots + b_{1i}r_i
\frac{dx_2}{dt} = a_{21}x_1 + a_{22}x_2 + \dots + a_{2n}x_n + b_{21}r_r + \dots + b_{2i}r_i
\vdots
\frac{dx_n}{dt} = a_{n1}x_1 + a_{n2}x_2 + \dots + a_{nn}x_n + b_{n1}r_r + \dots + b_{ni}r_i$$
(5.13)

In matrix notation the state variable can be compiled as;

$$\frac{d}{dt} \begin{bmatrix} x_1 \\ x_2 \\ \vdots \\ x_n \end{bmatrix} = \begin{bmatrix} \dot{x}_1 \\ \dot{x}_2 \\ \vdots \\ \dot{x}_n \end{bmatrix} = \begin{bmatrix} a_{11} & a_{12} & \cdots & a_{1n} \\ a_{21} & a_{22} & \cdots & a_{21} \\ \vdots & \vdots & \ddots & \vdots \\ a_{n1} & a_{n2} & \cdots & a_{nn} \end{bmatrix} \begin{bmatrix} x_1 \\ x_2 \\ \vdots \\ x_n \end{bmatrix} + \begin{bmatrix} b_{11} & \cdots & b_{1i} \\ b_{21} & \cdots & b_{2i} \\ \vdots & \ddots & \vdots \\ b_{n1} & \cdots & b_{ni} \end{bmatrix} \begin{bmatrix} r_1 \\ r_2 \\ \vdots \\ r_i \end{bmatrix}$$
or
$$\frac{d\mathbf{x}}{dt} = \dot{\mathbf{x}} = \mathbf{A}\mathbf{x} + \mathbf{B}\mathbf{r} \tag{5.14}$$

The system outputs are related to the state variables through the output equations;

$$\begin{bmatrix} y_1 \\ \vdots \\ y_m \end{bmatrix} = \begin{bmatrix} c_{11} & c_{12} & \cdots & c_{1n} \\ \vdots & \vdots & \ddots & \vdots \\ c_{m1} & c_{m2} & \cdots & c_{mn} \end{bmatrix} \begin{bmatrix} x_1 \\ \vdots \\ x_n \end{bmatrix}$$
or
$$\mathbf{y} = \mathbf{C}\mathbf{x}$$
(5.15)

The time course of the state variables are described by the state equations. This is a standard form of representing any system described by linear constant-coefficient integrodifferential equations. Often, systems consisting of a mixed collection of simultaneous system equations, some of first order, some of second order, some involving running integrals, etc., are manipulated to place them in this standard form. The primary advantage is that systematic methods of analysis such as frequency response analysis can be implemented on involved problems quite efficiently. For example, it may be desirable to determine the contributions of each of the state variables to the overall process gain of the system. In this exercise, the more significant state variables can be isolated from those that are much less significant. Thus, more insignificant state variable can either be neglected or considered as a disturbance input to the system. The latter scenario is described by the following equation assuming that the contribution of the state variable x_2 is negligible.

$$\begin{bmatrix} \dot{x}_1 \\ \dot{x}_3 \\ \vdots \\ \dot{x}_n \end{bmatrix} = \begin{bmatrix} a_{11} & a_{13} & \cdots & a_{1n} \\ a_{31} & a_{33} & \cdots & a_{31} \\ \vdots & \vdots & \ddots & \vdots \\ a_{n1} & a_{n3} & \cdots & a_{nn} \end{bmatrix} \begin{bmatrix} x_1 \\ x_3 \\ \vdots \\ x_n \end{bmatrix} + \begin{bmatrix} b_{11} & \cdots & b_{1i} \\ b_{31} & \cdots & b_{3i} \\ \vdots & \ddots & \vdots \\ b_{n1} & \cdots & b_{ni} \end{bmatrix} \begin{bmatrix} r_1 \\ r_3 \\ \vdots \\ r_i \end{bmatrix} + \begin{bmatrix} a_{12} \\ a_{22} \\ \vdots \\ a_{n2} \end{bmatrix} x_2 \quad (5.16)$$

This analysis gives process development engineers an insight to the process parameters most important toward design and development.

In crystallization the process state variables include, supersaturation, CSD, slurry density, total crystal surface area, nucleation rate, growth rate and heat flux. State variable analysis briefly outlined above will help identify the relative importance of process parameters related to each of the state variables at various operating conditions. The

relative merits of in situ measurement of supersaturation and in situ measurement of CSD can be analyzed.

The set of equations that describe a well mixed constant volume batch crystallizer is given by Equations 5.7, 5.8, 5.9 and 5.10. differential equations are highly nonlinear. However, a methodology for the systematic characterization of dynamic systems by state variable analysis has been developed only for linear systems as presented above. Thus, the convenience of state variable analysis is significant motivation for approximating nonlinear systems with linear ones. One technique commonly used is linearization around a judiciously chosen operating point using a Taylor series expansion [4]. The success of the linear approximation depends on the deviation of the system from the chosen operating point. The smaller the deviation the better the approximation. Therefore, process simulations will have to be used in aid of choosing the most appropriate operating point. In the rare event that linearization around an operating point fails to provide a reasonable approximation, more difficult methods of nonlinear analysis may have to be used [4].

5.1.2 Solution Structure

In Chapter 4 a reasonable amount of evidence was presented in the context of inferring the solution structure of aqueous maleic acid in supersaturated solutions. The presented evidence suggest that the folded structure of crystalline maleic acid remains intact in highly concentrated solutions. However, a concrete analysis on the nature of the solution state structure of aqueous maleic acid in supersaturated solutions was beyond the scope of the investigation discussed in Chapter 4.

The depth of the investigation can be extended using both Raman and NMR spectroscopy in addition to FTIR spectroscopy. The different techniques can reveal complementary information. Further, utilization of the deutero analogues of both water and maleic acid in experiments similar to those discussed in Chapter 4 can provide a host of confirmatory information [13, 14, 15]. The deuteration of a particular bond results in a significant red shift in its vibrational frequencies due to the heavy atom effect. For example, the v(O-D) vibration of the deuterated acetic acid is observed at 2299 cm⁻¹ in comparison to the v(O-H) vibration of acetic acid that occurs at 3140 cm $^{-1}$ [13]. The δ (O-D) vibration is observed at 1046 cm $^{-1}$ compared to the $\delta(O-H)$ vibration at 1294 cm⁻¹. Consequently, experimentation with selectively deuterated maleic acid and deuterated water in judiciously chosen combinations can help resolve many of the ambiguities of the analysis provided in Chapter 4. For example, use of maleic acid in heavy water will clear the v(O-H) stretching region of any contribution from the v(O-H) vibration of water thus making it much easier to identify dynamics of the v(O-H) vibration of maleic acid.

In Chapter 4, the peak near 1629 cm⁻¹ was assigned to the ν (C=C) stretching mode. However, the strength of the peak is not consistent with the vibrational mode. The strength of the IR active vibrational modes depend on the strength of the permanent dipole moment of the mode. Eventhough the maleic acid molecule is not perfectly symmetric around the

(C=C) bond, its relative symmetry prevents extensive polarization of the (C=C) bond. Therefore, the peak intensity of the v(C=C) mode is expected to be week. In fact, the v(C=C) mode is nonexistent in the IR spectrum of fumaric acid, which is the trans configuration of maleic acid, since it has a center of symmetry around the (C=C) bond. Consequently, the most likely event is that the strong band around 1629 cm⁻¹ is constituted by contributions from the v(C=C) mode and other modes of maleic acid. The other contributors could be overtones of lower frequency modes of maleic acid. The origins of these overtone bands can be scrutinized by experimentation with selectively deuterated maleic acid and deuterated water in judiciously chosen combinations. Separation of this convoluted band using deuterated species can provide additional information toward deducing the solution structure of aqueous maleic acid. **Ambiguities** resulting from band convolution of other identified modes can be resolved in similar fashion. In addition, assignments can be made on unidentified band and shoulders. Studies with complementary spectroscopic techniques such as Raman and NMR can be conducted with deuterated and non-deuterated species adding to the wealth of information available to study the solution structure.

5.1.3 Effect of impurities

In industrial crystallization, solutions invariably contain impurities within detectable limits. In some crystallization schemes, impurities may also be added to instigate desirable conditions. Impurities can significantly alter the solubility characteristics and crystallization kinetics of the

primary solute. In the presence of an impurity one of three situations is likely to arise. The impurity may react with the primary solute and completely alter the nature of the system, both chemically and physically. The presence of an impurity may drive the primary solute into supersaturation and thereby cause the primary solute to precipitate out of solution. Lastly, the presence of an impurity may cause the system to be undersaturated with respect to the primary solute. In the literature, the latter two effects are identified as 'salting-out' and 'salting-in', respectively. In addition, kinetics can be affected by the adsorption of impurity molecules on growing crystal surfaces. In industrial crystallization processes, monitoring of impurity (either contained or added) levels and/or their effects, is crucial for a successful operation.

ATR FTIR spectroscopy, in addition to having the capability to measure solubility and supersaturation, can be used to monitor the presence of additives or impurities and consequent reactions (reactive crystallization schemes included). Infrared spectra, that reflect the vibrational and rotational structure of the analytes, can provide more than one piece of information unlike traditional solubility and supersaturation measurement techniques that measure a single parameter calibrated for the measurement of solubility and supersaturation. The advantage is that necessary information can be obtained simultaneously using the same technique, in situ, without resorting to multiple techniques that are variable specific. The potential for the application of in situ ATR FTIR spectroscopy to study impurity effects remain to be explored.

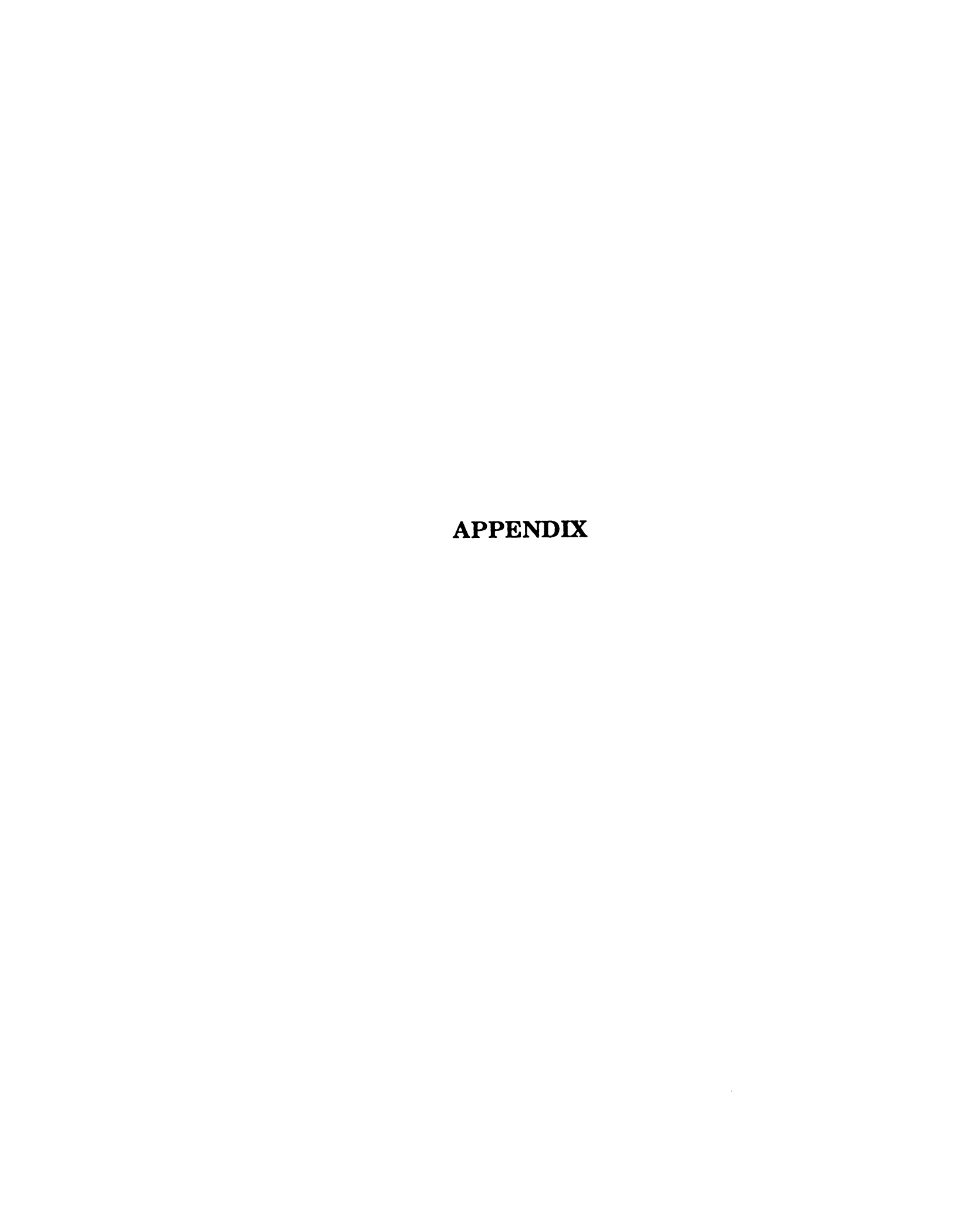
5.2 Conclusions

The utility of in situ ATR FTIR spectroscopy for the measurement of important crystallization parameters such as supersaturation, solubility and metastable limit was demonstrated in the previous chapters. feasibility of the technique toward process development and eventually control of batch crystallization processes that will provide for improved product quality/reproducibility, time savings and cost containment was established. However, its potential for implementation in control of crystallization processes, although promising, remains to be proven. chapter 4 substantial evidence demonstrating the potential of in situ ATR FTIR spectroscopy towards deducing solution structure in supersaturated solutions was presented. Utilization of in situ ATR FTIR spectroscopy in studying the effects of impurities on crystallization systems is yet another avenue remaining to be explored. Therefore, it is recommended that the implementation of control using in situ measurement of supersaturation using ATR FTIR spectroscopy, utilization of IR spectroscopy understanding solution structure in supersaturated solutions and investigation of effects of impurities on crystallizing systems using ATR FTIR spectroscopy be pursued in the future.

5.3 References

- 1. Jones, A. G., Mullin, J. W., Chem. Eng. Sci., 29, (1974), 105.
- 2. Garside, J., Chem. Eng. Sci., 40:1, (1985), 3.
- 3. Mullin, J. W., "Crystallization", Butterworth-Heineman, Oxford, England, (1993).

- 4. Coughanowr, D. R., "Process Systems Analysis and Control", McGraw-Hill, Inc., New York, USA.
- 5. Radcliffe, C., Professor, Mechanical Engineering, Michigan State University.
- 6. Perry, R., Chilton, Perry's Handbook of Chemical Engineering, McGraw Hill, New York, 6th Edition.
- 7. Randolph, A. D., Larson, M. A., "Theory of Particulate Processes", Academic Press, Inc., New York, USA., (1988), ch. 3.
- 8. Mullin, J. W., Nyvlt, J., Chem. Eng. Sci., 26, (1971), 369.
- 9. Nyvlt, J., Colln. Czech. Chem. Commun., 30, (1965), 2269.
- 10. Nyvlt, J., Mullin, J. W., Chem. Eng. Sci., 25, (1970), 131.
- 11. N. S. Tavare, Separation and Purification Methods, 22:2, 93, (1993).
- 12. Hostetter, G. H., Savant, Jr., C. J., Stefani, R. T., "Design of Feedback Control Systems", Holt, Rinehart and Winston, New York, USA, (1982), ch. 7.
- 13. Kishida, S., Nakamoto, K., J. Chem. Phys., 41:6, (1964), 1558.
- 14. Fukushima, K., Zwolinski, J., J. Chem. Phys., 50:2, (1969), 737.
- 15. Bratoz, S., Hadzi, D., Sheppard, N., Spectrochim. Acta., 8, (1956), 249.



APPENDIX

Table A1 Data for Figure 2.4

Temperature (°C)	RT ₁ at 10 °C	Temperature (°C)	RT ₁ at 30 °C
2.27	0.025	2.27	0.036
4.37	0.024	4.37	0.037
13.31	0.035	13.31	0.053
22.16	0.043	15.02	0.053
23.54	0.040	22.16	0.075
26.95	0.084	23.54	0.078
29.35	0.068	29.35	0.104
30.48	0.077	30.48	0.104
33.12	0.107	34.42	0.155
35.75	0.105	41.77	0.201
35.75	0.100	44.84	0.233
35.75	0.107	44.84	0.245
38.51	0.135	47.65	0.246
40.79	0.127	48.67	0.281
40.79	0.148	50.18	0.285
40.79	0.126	50.18	0.297
43.07	0.165	51.85	0.305
44.87	0.156	52.36	0.288
44.87	0.157	54.51	0.338
44.87	0.173	54.51	0.327
47.07	0.199	54.72	0.355
48.66	0.200	56.45	0.343
48.66	0.196	57.24	0.386
48.66	0.188	58.21	0.388
50.48	0.230	58.21	0.384
51.87	0.221	59.50	0.413
51.87	0.220	59.79	0.392
51.87	0.239	61.30	0.421
53.48	0.258	61.30	0.431
54.65	0.261	61.54	0.443
54.65	0.257	62.65	0.423
56.16	0.287	63.43	0.475
57.18	0.307	63.98	0.467
57.18	0.280	63.98	0.468
59.51	0.319	65.07	0.500
59.51	0.348	65.20	0.458
61.53	0.370	66.28	0.493
61.53	0.348	66.29	0.508
		68.36	0.535

Table A2 Data for Figures 2.5 and 2.6

Temperature (°C)	RT₁ at 10 °C	Temperature (°C)	RT ₁ at 30 °C
2.27	0.043	2.27	0.056
4.37	0.051	4.37	0.064
13.31	0.089	13.31	0.117
22.16	0.160	15.02	0.127
23.54	0.113	22.16	0.239
26.95	0.277	23.54	0.289
29.35	0.328	29.35	0.405
30.48	0.403	30.48	0.472
33.12	0.436	34.42	0.641
35.75	0.547	41.77	1.069
35.75	0.528	44.84	1.483
35.75	0.551	44.84	1.301
38.51	0.675	47.65	1.632
40.79	0.888	48.67	1.719
40.79	0.927	50.18	2.165
40.79	0.853	50.18	1.900
43.07	0.983	51.85	2.006
44.87	1.284	52.36	2.316
44.87	1.265	54.51	2.501
44.87	1.289	54.51	2.974
47.07	1.380	54.72	2.559
48.66	1.768	56.45	3.047
48.66	1.847	57.24	3.043
48.66	1.803	58.21	3.336
50.48	1.821	58.21	3.946
51.87	2.405	59.50	3.568
51.87	2.333	59.79	3.826
51.87	2.390	61.30	4.642
53.48	2.321	61.30	4.091
54.65	2.965	61.54	4.255
54.65	3.031	62.65	4.527
56.16	2.797	63.43	4.791
57.18	3.915	63.98	5.611
57.18	3.771	63.98	4.792
59.51	4.871	65.07	5.326
59.51	4.801	65.20	5.454
61.53	5.512	66.28	6.482
61.53	5.589	66.29	5.451
	1.00	68.36	6.491

Table A3 Data for Figures 2.7 and 2.8

Temperature (°C)	RT ₁	stdev in RT ₁	RT ₂	stdev in RT ₂
10	0.266	0.007	3.410	0.143
15	0.319	0.009	4.317	0.215
20	0.382	0.009	5.305	0.328
25	0.429	0.008	6.735	0.454
30	0.484	0.009	8.271	0.739
35	0.532	0.012	9.597	1.074

Table A4 Data for Figures 3.3 and 3.5

Temperature (°C)	T _R Solubility	Temperature	T _R Supersaturation profile	Temperature (°C)	T _R Supersaturation profile continued
52.70	4.821	66.50	7.508	62.21	7.296
56.60	5.611	66.44	7.425	62.05	7.378
60.51	6.443	66.38	7.529	61.90	7.252
64.51	7.408	66.32	7.611	61.74	7.345
66.47	7.874	66.24	7.501	61.59	7.332
	T _R	66.16	7.459	61.44	7.239
Temperature		66.08	7.531	61.29	7.354
(°C)	Limit	65.98	7.495	61.15	7.357
60.13	7.28	65.89	7.515	61.00	7.269
58.26	6.72	65.78	7.352	60.85	7.239
54.59	5.92	65.68	7.532	60.70	7.210
53.68	5.51	65.57	7.471	60.55	7.250
50.67	5.03	65.45	7.452	60.40	7.180
50.01	0.00	65.33	7.537	60.30	7.240
		65.20	7.449	60.15	7.210
		65.07	7.441	60.00	7.270
		64.94	7.414	59.75	7.240
		64.81	7.495	59.60	7.200
		64.67	7.353	59.45	7.250
		64.53	7.349	59.34	7.202
		64.38	7.394	59.69	7.326
		64.23	7.461	60.32	6.976
		64.09	7.475	60.60	6.960
		63.93	7.508	60.64	6.997
		63.78	7.280	60.64	6.774
		63.63	7.504	60.64	6.771
		63.47	7.378	60.57	6.836
		63.32	7.474	60.57	6.716
		63.16	7.275	60.55	6.676
		63.00	7.316	60.27	6.605
		62.84	7.425	60.23	6.582
		62.68	7.273	60.35	6.621
		62.53	7.440	59.94	7.130
		62.37	7.345	60.15	7.100

Table A5 Data for Figure 3.6

		1	Temperature		i		
	Temperature		(°C)		Temperature		Temperature
	(°C)	ļ	Parabolic		(°C)		(°C)
Time	Parabolic	Time	cooling	Time	Int. parabolic	Time	Linear
(sec)	cooling	(sec)	continued	(sec)	cooling	(sec)	cooling
0	63.04	1400	58.69	0	63.56	0	62.68
40	63.04	1440	58.42	40	63.45	20	62.26
80	63.03	1480	58.15	80	63.34	40	61.83
120	63.03	1520	57.86	120	63.21	60	61.40
160	63.02	1560	57.56	160	63.08	80	60.97
200	63.00	1600	57.26	200	62.94	100	60.54
240	62.98	1640	56.95	240	62.79	120	60.11
280	62.94	1680	56.63	280	62.64	140	59.68
320	62.90	1720	56.30	320	62.47	160	59.25
360	62.85			360	62.30	180	58.81
400	62.79]		400	62.12	200	58.38
440	62.73			440	61.93	220	57.95
480	62.65	Ì		480	61.73	240	57.51
520	62.57			520	61.53	260	57.08
560	62.48			560	61.31	280	56.64
600	62.38			600	61.09	300	56.21
640	62.27	ł		640	60.86	1	
680	62.16			680	60.62		
720	62.04			720	60.38		
760	61.90			760	60.12		
800	61.76			800	59.86		
840	61.62			840	59.59		
880	61.46			880	59.31		
920	61.30			920	59.02	Ì	
960	61.13			960	58.72		
1000	60.95			1000	58.42	1	
1040	60.76			1040	58.10		
1080	60.56			1080	57.78		
1120	60.36			1120	57.45	ŀ	
1160	60.14			1160	57.11	l	
1200	59.92			1200	56.77	l	
1240	59.69			1240	56.41		
1280	59.46			1280	56.05	1	
1320	59.21	Ī		1320	55.68		
1360	58.96			1360	55.30		

Table A6 Data for Figure 3.7

Temperature (°C)	T _R Supersaturation Profile	Temperature (°C)	T _R Supersaturation Profile continued
56.13	5.526	61.54	6.988
56.30	5.609	61.62	6.954
56.47	5.667	61.69	6.931
56.63	5.716	61.76	6.837
56.79	5.714	61.84	6.922
56.95	5.730	61.90	6.970
57.11	5.809	61.97	6.854
57.26	5.758	62.04	6.960
57.41	5.823	62.10	7.048
57.56	5.826	62.16	6.944
57.71	5.918	62.22	7.070
57.86	5.926	62.27	7.065
58.00	5.926	62.33	7.070
58.15	6.033	62.38	7.089
58.29	6.039	62.43	7.079
58.42	6.021	62.48	7.099
58.56	6.079	62.52	7.201
58.69	6.190	62.57	7.036
58.83	6.195	62.61	7.191
58.96	6.212	62.65	7.159
59.09	6.270	62.69	7.137
59.21	6.255	62.73	7.261
59.33	6.309	62.76	7.203
59.46	6.312	62.79	7.160
59.58	6.386	62.82	7.210
59.69	6.347	62.85	7.226
59.81	6.501	62.88	7.307
59.92	6.517	62.90	7.287
60.03	6.486	62.92	7.312
60.14	6.517	62.94	7.286
60.25	6.522	62.96	7.114
60.36	6.447	62.98	7.194
60.46	6.482	62.99	7.366
60.56	6.707	63.00	7.278
60.66	6.599	63.01	7.340
60.76	6.619	63.02	7.215
60.76	6.729	63.02	7.215
60.95	6.770	63.03 63.03	7.316
61.04	6.753	63.03	7.282
61.13	6.858 6.757	63.03	7.294
61.21 61.30		63.03	7.289
	6.883		7.322
61.38	6.765	63.04	7.270
61.46	6.910	63.04	7.228

Table A7 Data for Figure 3.8

Temperature (°C)	T _R Supersaturation Profile	Temperature (°C)	T _R Supersaturation Profile continued
			كالشار والمراج
55.296	5.3865	60.744	6.6312
55.487	5.4195	60.862	6.7642
55.677	5.5388	60.978	6.8338
55.864	5.4821	61.092	6.7956
56.049	5.5299	61.204	6.8988
56.232	5.6675	61.314	6.8647
56.412	5.658	61.422	6.8572
56.591	5.7099	61.528	6.8928
56.767	5.7356	61.631	6.7263
56.942	5.7091	61.733	6.946
57.114	5.7315	61.833	7.1089
57.285	5.801	61.93	7.1234
57.453	5.8375	62.026	7.1212
57.619	5.8934	62.119	7.1956
57.783	5.9689	62.211	7.15
57.945	5.8844	62.3	7.196
58.104	6.0924	62.387	7.1268
58.262	6.0357	62.472	7.1791
58.418	5.9942	62.556	7.1612
58.571	6.1303	62.637	7.0954
58.722	6.0929	62.716	7.1826
58.872	6.1093	62.793	7.2122
59.019	6.1969	62.868	7.2826
59.164	6.3091	62.941	7.3143
59.307	6.3879	63.011	7.1401
59.448	6.336	63.08	7.1582
59.587	6.262	63.147	7.1531
59.724	6.3609	63.212	7.1343
59.859	6.4884	63.274	7.1327
59.991	6.4618	63.335	7.1691
60.122	6.4843	63.394	7.0479
60.25	6.4718	63.45	7.235
60.377	6.58	63.505	7.1843
60.501	6.5267	63.557	7.2077
60.624	6.6256		

Table A8 Data for Figure 3

 $\label{eq:TR} \textbf{Temperature Supersaturation}$

i emperature	Supersaturation
(°C)	Profile
56.207	5.6364
56.643	5.7073
57.078	5.7531
57.513	5.7942
57.947	5.9737
58.38	6.1093
58.813	6.1557
59.246	6.4522
59.677	6.4576
60.108	6.7233
60.539	6.7861
60.969	7.0622
61.398	7.1281
61.827	7.0984
62.255	7.1642
62.682	7.2312

Data for Figure 3.10 Table A9

CSD (%weight) CSD (%weight) Intermediate CSD (%weight)

Size (microns)	Parabolic cooling profile	parabolic cooling profi le	Linear cooling profile
180	0.00	0.52	0.44
265	0.40	1.40	2.08
373	4.10	13.16	45.84
463	4.90	9.58	15.88
550	9.20	14.80	14.78
655	13.10	13.62	5.28
780	23.70	21.84	1.90
925	18.00	12.88	0.00
1000	13.30	5.14	0.00

Table A10.1 Data for Figure 3.11

Temperature	T _R Concentration line 60 % w/w	Temperature	T _R Concentration line 60 % w/w
56.89	4.827	56.90	4.795
56.86	4.778	56.86	4.833
56.82	4.764	56.81	4.811
56.76	4.838	56.76	4.856
56.71	4.801	56.70	4.853
56.64	4.807	56.64	4.882
56.57	4.774	56.57	4.864
56.50	4.772	56.50	4.822
56.42	4.750	56.43	4.784
56.33	4.762	56.35	4.758
56.24	4.694	56.27	4.794
56.15	4.739	56.19	4.839
56.05	4.762	56.10	4.790
55.95	4.783	56.01	4.785
55.84	4.714	55.91	4.773
55.74	4.772	55.81	4.850
55.63	4.768	55.71	4.735
55.52	4.738	55.61	4.770
55.41	4.795	55.50	4.738
55.29	4.744	55.39	4.791
55.18	4.779	55.28	4.840
55.06	4.729	55.16	4.859
54.94	4.823	55.04	4.814
54.82	4.830	54.92	4.792
54.70	4.761	54.80	4.779
54.58	4.774	54.68	4.745
54.46	4.727	54.55	4.738
54.34	4.753	54.42	4.813
54.22	4.790	54.29	4.705
54.09	4.787	54.16	4.672
53.97	4.706	54.03	4.798
53.84	4.770	53.89	4.736
53.71	4.797	53.76	4.736
53.59	4.780	53.62	4.753
53.46	4.685	53.48	4.806
53.33	4.682	53.34	4.729
53.20	4.751	53.20	4.705
53.06	4.712	53.06	4.693
52.93	4.739	52.91	4.736
52.79	4.703	52.77	4.745
52.65	4.826	52.62	4.710
52.51	4.698	52.47	4.715
52.36	4.760	52.33	4.761
52.21	4.701	52.18	4.727
52.06	4.686	52.03	4.749
51.90	4.715	51.88	4.728

Table A10.2 Data for Figure 3.11

Temperature (°C)	T _R Concentration line 61 % w/w	Temperature	T _R Concentration line 61 % w/w
58.52	5.200	58.54	5.266
58.52	5.228	58.53	5.387
58.51	5.283	58.51	5.270
58.48	5.250	58.49	5.167
58.45	5.221	58.46	5.184
58.42	5.252	58.42	5.303
58.37	5.314	58.38	5.258
58.32	5.224	58.33	5.224
58.26	5.299	58.28	5.221
58.20	5.207	58.23	5.307
58.13	5.196	58.17	5.246
58.05	5.238	58.10	5.251
57.97	5.247	58.03	5.217
57.89	5.313	57.96	5.198
57.80	5.291	57.88	5.245
57.70	5.288	57.80	5.234
57.60	5.184	57.71	5.202
57.50	5.169	57.62	5.191
57.39	5.221	57.53	5.260
57.28	5.153	57.43	5.248
57.16	5.188	57.33	5.094
57.04	5.271	57.23	5.239
56.92	5.243	57.12	5.255
56.80	5.142	57.01	5.168
56.67	5.137	56.89	5.278
56.55	5.131	56.78	5.228
56.41	5.180	56.66	5.211
56.28	5.149	56.53	5.183
56.15	5.226	56.41	5.161
56.01	5.211	56.28	5.224
55.87	5.148	56.15	5.242
55.73	5.180	56.01	5.201
55.59	5.181	55.88	5.156
55.45	5.197	55.74	5.180
55.31	5.163	55.60	5.177
55.16	5.163	55.46	5.194
55.02	5.195	55.32	5.191
54.87	5.182	55.17	5.152
54.73	5.140	55.03	5.104
54.78	5.075	54.88	5.173
54.43	5.182	54.73	5.173
54.28	5.181	54.58	5.203
54.13	5.106	54.43	5.219
53.99	5.121	54.28	5.116
53.84	5.127	54.13	5.200

Table A10.3 Data for Figure 3.11

	T _R Concentration		T _R Concentration
Temperature	line	Temperature	line
(°C)	62 % w/w	(°C)	62 % w/w
60.34	5.685	60.29	5.832
60.33	5.703	60.32	5.768
60.32	5.730	60.33	5.704
60.30	5.754	60.33	5.786
60.27	5.710	60.32	5.760
60.24	5.777	60.30	5.756
60.20	5.795	60.27	5.719
60.15	5.655	60.24	5.681
60.10	5.751	60.19	5.709
60.04	5.716	60.14	5.690
59.97	5.759	60.09	5.681
59.90	5.670	60.02	5.710
59.83	5.637	59.95	5.712
59.75	5.622	59.87	5.751
59.66	5.696	59.79	5.661
59.57	5.712	59.70	5.772
59.47	5.656	59.61	5.614
59.37	5.573	59.51	5.759
59.27	5.730	59.40	5.734
59.16	5.707	59.30	5.734
59.04	5.700	59.18	5.725
58.93	5.691	59.07	5.634
58.81	5.699	58.94	5.682
58.68	5.765	58.82	5.594
58.55	5.666	58.69	5.639
58.42	5.675	58.56	5.720
58.29	5.670	58.43	5.661
58.16	5.613	58.29	5.677
58.02	5.654	58.15	5.692
57.88	5.596	58.01	5.640
57.74	5.651	57.87	5.608
57.59	5.554	57.72	5.655
57.45	5.625	57.58	5.719
57.30	5.568	57.43	5.721
57.15	5.673	57.28	5.644
57.00	5.640	57.13	5.584
56.85	5.538	56.98	5.529
56.70	5.506	56.83	5.577
56.55	5.634	56.67	5.613
56.39	5.577	56.52	5.551
56.24	5.626	56.36	5.581
56.09	5.561	56.21	5.536
55.94	5.598	56.05	5.632
55.79	5.565	55.90	5.541
55.63	5.565	55.74	5.612
55.48	5.498	55.59	5.489

Table A10.4 Data for Figure 3.11

Temperature	T _R Concentration line 63 % w/w	Temperature (°C)	T _R Concentration line 63 % w/w
	6.059	62.22	6.138
62.20 62.21	6.269	62.22	6.211
62.21	6.269	62.22	6.247
62.21	6.195	62.22	6.247
62.19 62.16	6.068 6.180	62.19 62.16	6.287 6.141
62.13	6.108	62.10	6.134
62.08	6.216	62.07	6.084
62.03	6.205	62.01	6.153
61.97	6.141	61.95	6.141
61.91	6.173	61.88	6.181
61.83	6.134	61.80	6.193
61.75	6.123	61.72	6.063
61.66	6.139	61.63	6.190
61.57	6.145	61.53	6.122
61.47	6.060	61.43	6.106
61.37	6.139	61.33	6.087
61.26	6.045	61.22	6.231
61.15	6.146	61.10	6.163
61.03	6.265	60.99	6.153
60.91	6.130	60.86	6.089
60.78	6.144	60.74	6.216
60.65	6.117	60.61	6.107
60.51	6.075	60.48	6.252
60.38	6.143	60.35	6.148
60.24	6.114	60.21	6.164
60.09	6.158	60.07	6.185
59.95	6.198	59.94	6.098
59.80	6.082	59.79	6.173
59.65	6.049	59.65	6.095
59.49	6.056	59.51	6.063
59.34	6.100	59.36	6.028
59.18	6.050	59.22	6.126
59.03	6.014	59.07	6.041
58.87	6.140	58.92	6.106
58.71	6.091	58.77	6.038
58.55	6.038	58.62	6.002
58.38	6.026	58.47	5.990
58.22	6.062	58.32	6.036
58.06	5.930	58.17	6.029
57.90	5.974	58.02	5.952
57.90 57.73	6.023	57.87	5.952 6.043
57.57	6.090	57.71	6.052
57.40	5.980	57.56	6.045
57.24	5.930	57.41	6.003
57.08	5.954	57.26	6.057

Table A10.5 Data for Figure 3.11

Temperature	T _R Concentration line 64 % w/w	Temperature	T _R Concentration line 64 % w/w
64.94	6.699	65.57	6.965
64.95	6.753	65.54	7.016
64.95	6.801	65.51	6.932
64.95	6.741	65.46	6.925
64.93	6.780	65.40	6.919
64.90	6.683	65.34	7.044
64.87	6.881	65.27	6.957
64.83	6.746	65.19	6.848
64.78	6.636	65.11	6.924
64.72	6.952	65.02	6.859
64.66	6.811	64.92	6.836
64.59	6.796	64.82	6.967
64.51	6.927	64.71	6.878
64.42	7.053	64.60	6.980
64.33	6.696	64.48	6.969
64.24	6.886	64.36	6.960
64.14	6.843	64.24	6.901
64.03	6.680	64.11	6.845
63.92	6.786	63.98	6.945
63.80	6.794	63.85	6.894
63.68	6.811	63.71	6.925
63.55	6.639	63.58	
			6.968
63.42 63.28	6.756 6.719	63.44 63.29	6.811 6.787
63.15			
63.00	6.949 6.740	63.15 63.01	6.916 6.878
62.86			
	6.806	62.86	6.930
62.71	6.850	62.71	6.929
62.56	6.702	62.56	6.889
62.41	6.756	62.41	6.864
62.25	6.700	62.26	6.903
62.10	6.836	62.11	6.797
61.94	6.983	61.95	6.904
61.78	6.595	61.80	6.838
61.62	6.964	61.64	6.712
61.46	6.913	61.48	6.791
61.30	6.568	61.33	6.905
61.14	6.806	61.17	6.865
60.98	6.717	61.01	6.856
60.81	7.370	60.84	6.852
60.65	6.733	60.68	6.848
60.49	6.772	60.51	6.830
60.33	6.526	60.35	6.850
60.17	6.528	60.18	6.722
60.02	6.673	60.00	6.771
59.86	6.711	59.83	6.857

Table A10.6 Data for Figure 3.11

Temperature	T _R Concentration line 65 % w/w	Temperature	T _R Concentration line 65 % w/w
66.30	7.508	66.34	7.519
66.31	7.425	66.33	7.395
66.31	7.529	66.31	7.526
66.29	7.611	66.28	7.471
66.26	7.501	66.24	7.619
66.22	7.459	66.19	7.524
66.17	7.531	66.14	7.533
66.10	7.495	66.08	7.581
66.03	7.515	66.01	7.440
65.95	7.352	65.93	7.381
65.86	7.533	65.85	7.609
65.76	7.471	65.76	7.535
65.66	7.452	65.67	7.477
65.55	7.537	65.57	7.514
65.44	7.449	65.46	7.401
65.32	7.441	65.35	7.456
65.19	7.414	65.24	7.537
65.07	7.414	65.12	7.501
64.94	7.353	64.99	7.593
64.80	7.349	64.86	7.587
64.67	7.394	64.73	7.483
64.53	7.461	64.59	7.405
64.39	7.475	64.45	7.480
64.24	7.508	64.31	7.465
64.10	7.280	64.17	7.391
63.95	7.504	64.02	7.473
63.81	7.378	63.86	7.507
63.66	7.474	63.71	7.268
63.51	7.275	63.55	7.477
63.36	7.316	63.39	
			7.323
63.21 63.06	7.425 7.273	63.23 63.07	7.432
62.90	7.440	62.90	7.418 7.339
	7.345		
62.75		62.74	7.313
62.59 62.43	7.296 7.378	62.57 62.40	7.342 7.381
62.27	7.252	62.23	7.339
62.11	7.345	62.05	7.342
61.95	7.332	61.88	7.344
61.78	7.239	61.71	7.357
61.61	7.354	61.53	7.297
61.44	7.357	61.36	7.395
61.26	7.269	61.18	7.324
61.07	7.295	61.00	7.434
60.89	7.120	60.83	7.348
60.69	7.245	60.65	7.359

Table A11 Data for Figure 4.5

Temperature Iline S0 % w/w C°C S3 % w/w C°C S3 % w/w C°C S6 % w/w S5 % w/w C°C S5 % w/w C°C S6 % w/w S5 % w/w S		PIR ₁ Concentration		PIR ₁ Concentration		PIR ₁ Concentration
(°C) 50 % w/w (°C) 53 % w/w (°C) 56 % w/w 35.55 1.810 42.98 2.221 50.33 2.602 35.55 1.808 42.98 2.156 50.33 2.480 35.55 1.808 42.98 2.125 50.33 2.480 35.20 1.797 42.51 2.136 49.84 2.459 34.79 1.827 42.10 2.042 48.88 2.462 34.02 1.748 41.29 2.056 48.42 2.301 33.66 1.751 40.80 2.021 47.91 2.301 32.86 1.746 40.38 2.016 46.96 2.306 32.51 1.723 39.55 1.904 47.91 2.206 38.77 1.871 45.58 2.237 37.53 1.846 43.82 2.091 43.44 2.123 75.75 3.105 64.65 3.852 67.35 4.200 57	Temperature		Temperature		Temperature	
35.55			•	-	•	
35.55		1.810		2.221	50.33	2.602
35.55					50.33	
34.79			42.98	2.125	50.33	2.480
34.02	35.20	1.797	42.51	2.136	49.84	2.459
33.66 1.751 40.80 2.021 47.91 2.301 32.86 1.746 40.38 2.016 46.96 2.306 32.51 1.723 39.55 1.904 47.91 2.206 38.77 1.871 45.58 2.237 38.38 1.972 44.72 2.194 37.53 1.846 43.82 2.091 PIR₁ Concentration Temperature (°C) 59 % w/w (°C) 62 % w/w (°C) 65 % w/w 57.75 3.105 64.65 3.852 67.35 4.200 57.75 3.090 64.65 3.813 67.35 4.099 57.75 3.074 63.91 3.849 66.82 4.043 57.18 3.018 63.31 3.869 66.82 4.043 57.18 3.018 63.31 3.869 66.82 4.015 56.10 2.931 62.63 3.628 65.27 3.833 55.48 2.861 61.95 3.581 64.65 3.628 54.89 2.707 60.75 3.406 63.91 3.674 53.89 2.634 60.13 3.339 62.63 3.420 53.41 2.641 59.00 3.328 61.95 3.388 52.40 2.501 58.32 3.055 60.75 3.362 51.26 2.472 57.18 2.922 50.33 2.454 56.10 2.858 49.84 2.391 55.48 2.806 48.88 2.311 54.46 2.811 53.41 2.618	34.79	1.827	42.10	2.042	48.88	2.462
32.86 1.746 40.38 2.016 46.96 2.306 32.51 1.723 39.55 1.904 47.91 2.206 38.77 1.871 45.58 2.237 38.38 1.972 44.72 2.194 37.53 1.846 43.82 2.091 43.44 2.123	34.02	1.748	41.29	2.056	48.42	2.301
32.51 1.723 39.55 1.904 47.91 2.206 38.77 1.871 45.58 2.237 38.38 1.972 44.72 2.194 37.53 1.846 43.82 2.091 PIR1	33.66	1.751	40.80	2.021	47.91	2.301
38.77 1.871 45.58 2.237 38.38 1.972 44.72 2.194 37.53 1.846 43.82 2.091 43.44 2.123	32.86	1.746	40.38	2.016	46.96	2.306
38.38 1.972 44.72 2.194 37.53 1.846 43.82 2.091 43.44 2.123	32.51	1.723	39.55	1.904	47.91	2.206
PiR1 Concentration Temperature (°C) E3 % w/w Final Concentration Iine F59 % w/w Final Concentration Iine Final Final Concentration Iine Final			38.77	1.871	45.58	2.237
PiR1 Concentration Temperature (°C) E3 % w/w Concentration Iine F7.75 3.105 64.65 3.852 67.35 4.200			38.38	1.972	44.72	2.194
PiR1 Concentration Temperature (°C) S9 % w/w (°C) (°C			37.53	1.846	43.82	2.091
Temperature (°C) Concentration line Temperature (°C) Concentration line Temperature (°C) Concentration line (°C) Concentration line (°C) Temperature (°C) Concentration line (°C) Example (°C) Second					43.44	2.123
Temperature (°C) line (°C) tine (°C)		-				•
(°C) 59 % w/w (°C) 62 % w/w (°C) 65 % w/w 57.75 3.105 64.65 3.852 67.35 4.200 57.75 3.090 64.65 3.813 67.35 4.099 57.75 3.074 63.91 3.849 66.82 4.043 57.18 3.018 63.31 3.869 66.82 4.015 56.10 2.931 62.63 3.628 65.27 3.833 55.48 2.861 61.95 3.581 64.65 3.628 54.89 2.707 60.75 3.406 63.91 3.674 53.89 2.634 60.13 3.339 62.63 3.420 53.41 2.641 59.00 3.328 61.95 3.388 52.40 2.501 58.32 3.055 60.75 3.362 51.26 2.472 57.18 2.922 50.33 2.454 56.10 2.858 49.84 2.391 54.46 <td< th=""><th></th><th></th><th></th><th></th><th></th><th></th></td<>						
57.75 3.105 64.65 3.852 67.35 4.200 57.75 3.090 64.65 3.813 67.35 4.099 57.75 3.074 63.91 3.849 66.82 4.043 57.18 3.018 63.31 3.869 66.82 4.015 56.10 2.931 62.63 3.628 65.27 3.833 55.48 2.861 61.95 3.581 64.65 3.628 54.89 2.707 60.75 3.406 63.91 3.674 53.89 2.634 60.13 3.339 62.63 3.420 53.41 2.641 59.00 3.328 61.95 3.388 52.40 2.501 58.32 3.055 60.75 3.362 51.26 2.472 57.18 2.922 50.33 2.454 56.10 2.858 49.84 2.391 55.48 2.806 48.88 2.311 54.46 2.811 53.41 <th></th> <th></th> <th></th> <th></th> <th></th> <th></th>						
57.75 3.090 64.65 3.813 67.35 4.099 57.75 3.074 63.91 3.849 66.82 4.043 57.18 3.018 63.31 3.869 66.82 4.015 56.10 2.931 62.63 3.628 65.27 3.833 55.48 2.861 61.95 3.581 64.65 3.628 54.89 2.707 60.75 3.406 63.91 3.674 53.89 2.634 60.13 3.339 62.63 3.420 53.41 2.641 59.00 3.328 61.95 3.388 52.40 2.501 58.32 3.055 60.75 3.362 51.26 2.472 57.18 2.922 50.33 2.454 56.10 2.858 49.84 2.391 55.48 2.806 48.88 2.311 54.46 2.811 53.41 2.618 2.618	(°C)	59 % w/w	(℃)	62 % w/w	(°C)	65 % w/w
57.75 3.074 63.91 3.849 66.82 4.043 57.18 3.018 63.31 3.869 66.82 4.015 56.10 2.931 62.63 3.628 65.27 3.833 55.48 2.861 61.95 3.581 64.65 3.628 54.89 2.707 60.75 3.406 63.91 3.674 53.89 2.634 60.13 3.339 62.63 3.420 53.41 2.641 59.00 3.328 61.95 3.388 52.40 2.501 58.32 3.055 60.75 3.362 51.26 2.472 57.18 2.922 50.33 2.454 56.10 2.858 49.84 2.391 55.48 2.806 48.88 2.311 54.46 2.811 53.41 2.618	57.75	3.105	64.65	3.852	67.35	4.200
57.18 3.018 63.31 3.869 66.82 4.015 56.10 2.931 62.63 3.628 65.27 3.833 55.48 2.861 61.95 3.581 64.65 3.628 54.89 2.707 60.75 3.406 63.91 3.674 53.89 2.634 60.13 3.339 62.63 3.420 53.41 2.641 59.00 3.328 61.95 3.388 52.40 2.501 58.32 3.055 60.75 3.362 51.26 2.472 57.18 2.922 50.33 2.454 56.10 2.858 49.84 2.391 55.48 2.806 48.88 2.311 54.46 2.811 53.41 2.618	57.75	3.090	64.65	3.813	67.35	4.099
56.10 2.931 62.63 3.628 65.27 3.833 55.48 2.861 61.95 3.581 64.65 3.628 54.89 2.707 60.75 3.406 63.91 3.674 53.89 2.634 60.13 3.339 62.63 3.420 53.41 2.641 59.00 3.328 61.95 3.388 52.40 2.501 58.32 3.055 60.75 3.362 51.26 2.472 57.18 2.922 50.33 2.454 56.10 2.858 49.84 2.391 55.48 2.806 48.88 2.311 54.46 2.811 53.41 2.618	57.75	3.074	63.91	3.849	66.82	4.043
55.48 2.861 61.95 3.581 64.65 3.628 54.89 2.707 60.75 3.406 63.91 3.674 53.89 2.634 60.13 3.339 62.63 3.420 53.41 2.641 59.00 3.328 61.95 3.388 52.40 2.501 58.32 3.055 60.75 3.362 51.26 2.472 57.18 2.922 60.75 3.362 50.33 2.454 56.10 2.858 2.806 49.84 2.391 55.48 2.806 48.88 2.311 54.46 2.811 53.41 2.618	57.18	3.018	63.31	3.869	66.82	4.015
54.89 2.707 60.75 3.406 63.91 3.674 53.89 2.634 60.13 3.339 62.63 3.420 53.41 2.641 59.00 3.328 61.95 3.388 52.40 2.501 58.32 3.055 60.75 3.362 51.26 2.472 57.18 2.922 50.33 2.454 56.10 2.858 49.84 2.391 55.48 2.806 48.88 2.311 54.46 2.811 53.41 2.618	56.10	2.931	62.63	3.628	65.27	3.833
53.89 2.634 60.13 3.339 62.63 3.420 53.41 2.641 59.00 3.328 61.95 3.388 52.40 2.501 58.32 3.055 60.75 3.362 51.26 2.472 57.18 2.922 60.75 3.362 50.33 2.454 56.10 2.858 2.806 48.88 2.311 54.46 2.811 2.618	55.48				64.65	3.628
53.41 2.641 59.00 3.328 61.95 3.388 52.40 2.501 58.32 3.055 60.75 3.362 51.26 2.472 57.18 2.922 50.33 2.454 56.10 2.858 49.84 2.391 55.48 2.806 48.88 2.311 54.46 2.811 53.41 2.618					63.91	3.674
52.40 2.501 58.32 3.055 60.75 3.362 51.26 2.472 57.18 2.922 50.33 2.454 56.10 2.858 49.84 2.391 55.48 2.806 48.88 2.311 54.46 2.811 53.41 2.618				3.339		3.420
51.26 2.472 57.18 2.922 50.33 2.454 56.10 2.858 49.84 2.391 55.48 2.806 48.88 2.311 54.46 2.811 53.41 2.618				3.328		3.388
50.33 2.454 56.10 2.858 49.84 2.391 55.48 2.806 48.88 2.311 54.46 2.811 53.41 2.618		2.501		3.055	60.75	3.362
49.84 2.391 55.48 2.806 48.88 2.311 54.46 2.811 53.41 2.618						
48.88 2.311 54.46 2.811 53.41 2.618		2 454	56.10			
53.41 2.618	10 81					
		2.391				
54.46 2.596		2.391	54.46	2.811		
		2.391	54.46 53.41	2.811 2.618		

PIR₁ **Temperature** PIR₁ Solubility (°C) **Solubility** stdev 31.09 1.696 0.043 36.07 1.835 0.044 40.99 2.027 0.036 45.88 2.231 0.038 50.73 2.461 0.053 55.57 2.805 0.042 60.53 3.253 0.128 65.43 3.778 0.058

Table A12 Data for Figure 4.6

	PIR₁ Concentration		PIR ₁ Concentration		PIR ₁ Concentration
Temperature	line	Temperature	line	Temperature	line
(°C)	50 % w/w	(℃)	53 % w/w	(°C)	56 % w/w
35.55	4.269	42.98	4.990	50.33	6.157
35.55	4.251	42.98	5.031	50.33	6.097
35.55	4.246	42.98	4.927	50.33	5.984
35.20	4.255	42.51	4.930	49.84	6.070
34.79	4.175	42.10	4.962	48.88	6.015
34.02	4.250	41.29	4.886	48.42	5.847
33.66	4.163	40.80	4.938	47.91	5.986
32.86	4.272	40.38	4.998	46.96	5.976
32.51	4.231	39.55	5.047	47.91	5.991
		38.77	4.946	45.58	5.917
		38.38	4.978	44.72	5.869
		37.53	4.892	43.82	5.899
				43.44	5.827
	PIR₁		PIR₁		PIR ₁
	Concentration		Concentration		Concentration
Temperature	line	Temperature	line	Temperature	line
(°C)	59 % w/w	(℃)	62 % w/w	(°C)	65 % w/w
57.75	7.443	64.65	8.669	67.35	10.606
57.75	7.484	64.65	8.863	67.35	10.793
57.75	7.290	63.91	8.526	66.82	10.639
57.18	7.174	00 04			
56.10		63.31	8.435	66.82	10.904
	7.163	62.63	8.808	65.27	10.358
55.48	7.163 7.121	62.63 61.95	8.808 8.709	65.27 64.65	10.358 10.814
55.48 54.89	7.163 7.121 7.185	62.63 61.95 60.75	8.808 8.709 8.509	65.27 64.65 63.91	10.358 10.814 10.715
55.48 54.89 53.89	7.163 7.121 7.185 7.169	62.63 61.95 60.75 60.13	8.808 8.709 8.509 8.831	65.27 64.65 63.91 62.63	10.358 10.814 10.715 10.885
55.48 54.89 53.89 53.41	7.163 7.121 7.185 7.169 6.962	62.63 61.95 60.75 60.13 59.00	8.808 8.709 8.509 8.831 8.450	65.27 64.65 63.91 62.63 61.95	10.358 10.814 10.715 10.885 10.530
55.48 54.89 53.89 53.41 52.40	7.163 7.121 7.185 7.169 6.962 7.104	62.63 61.95 60.75 60.13 59.00 58.32	8.808 8.709 8.509 8.831 8.450 8.661	65.27 64.65 63.91 62.63	10.358 10.814 10.715 10.885
55.48 54.89 53.89 53.41 52.40 51.26	7.163 7.121 7.185 7.169 6.962 7.104 7.041	62.63 61.95 60.75 60.13 59.00 58.32 57.18	8.808 8.709 8.509 8.831 8.450 8.661 8.735	65.27 64.65 63.91 62.63 61.95	10.358 10.814 10.715 10.885 10.530
55.48 54.89 53.89 53.41 52.40 51.26 50.33	7.163 7.121 7.185 7.169 6.962 7.104 7.041 7.161	62.63 61.95 60.75 60.13 59.00 58.32 57.18 56.10	8.808 8.709 8.509 8.831 8.450 8.661 8.735 8.540	65.27 64.65 63.91 62.63 61.95	10.358 10.814 10.715 10.885 10.530
55.48 54.89 53.89 53.41 52.40 51.26 50.33 49.84	7.163 7.121 7.185 7.169 6.962 7.104 7.041 7.161 7.160	62.63 61.95 60.75 60.13 59.00 58.32 57.18 56.10 55.48	8.808 8.709 8.509 8.831 8.450 8.661 8.735 8.540 8.367	65.27 64.65 63.91 62.63 61.95	10.358 10.814 10.715 10.885 10.530
55.48 54.89 53.89 53.41 52.40 51.26 50.33	7.163 7.121 7.185 7.169 6.962 7.104 7.041 7.161	62.63 61.95 60.75 60.13 59.00 58.32 57.18 56.10 55.48 54.46	8.808 8.709 8.509 8.831 8.450 8.661 8.735 8.540 8.367 8.588	65.27 64.65 63.91 62.63 61.95	10.358 10.814 10.715 10.885 10.530
55.48 54.89 53.89 53.41 52.40 51.26 50.33 49.84	7.163 7.121 7.185 7.169 6.962 7.104 7.041 7.161 7.160	62.63 61.95 60.75 60.13 59.00 58.32 57.18 56.10 55.48 54.46 53.41	8.808 8.709 8.509 8.831 8.450 8.661 8.735 8.540 8.367 8.588 8.470	65.27 64.65 63.91 62.63 61.95	10.358 10.814 10.715 10.885 10.530
55.48 54.89 53.89 53.41 52.40 51.26 50.33 49.84	7.163 7.121 7.185 7.169 6.962 7.104 7.041 7.161 7.160	62.63 61.95 60.75 60.13 59.00 58.32 57.18 56.10 55.48 54.46	8.808 8.709 8.509 8.831 8.450 8.661 8.735 8.540 8.367 8.588	65.27 64.65 63.91 62.63 61.95	10.358 10.814 10.715 10.885 10.530

Temperature (°C)	PIR₁ Solubility	PIR ₁ Solubility stdev
31.09	3.888	0.025
36.07	4.463	0.040
40.99	5.213	0.054
45.88	6.042	0.108
50.73	7.106	0.071
55.57	8.431	0.144
60.53	9.753	0.191
65.43	11.327	0.255

Table A13 Data for Figure 4.10

Temperature (°C)	Peak shift relative to 5862 nm. 50 % w/w	Temperature (°C)	Peak shift relative to 5862 nm. 54 % w/w	Temperature (°C)	Peak shift relative to 5862 nm. 58 % w/w	
35.55	-2.248	45.58	-4.249	55.48	-5.501	
35.55	-2.053	45.58	-3.881	55.48	-5.701	
35.55	-2.213	45.17	-3.826	54.89	<i>-</i> 5.520	
35.20	-2.186	44.72	-3.774	54.46	-5.329	
34.79	-2.073	44.32	-3.725	53.89	-5.312	
34.02	-1.806	43.82	-3.757	53.41	- 5.062	
33.66	-1.960	42.98	-3.340	52.40	-4.741	
32.86	-1.523	42.51	-2.938	51.86	-4 .682	
32.51	-2.053	41.65	-2.503	50.82	-4.740	
		41.29	-2.981	50.33	-4 .575	
		40.38	-2.961	49.36	-4.474	
		40.01	- 2.370	48.42	-3.824	
		39.18	-2.695	47.91	-4.114	
		38.38	-1.953	46.96	-3.862	
	Peak shift		Peak shift	•	Peak shift	
	I van siiit		reak Sillit	1	reak sniit	
	relative to		relative to		relative to	
Temperature		Temperature		Temperature		Solubility
Temperature (°C)	relative to	Temperature (°C)	relative to	Temperature (°C)	relative to	Solubility stdev
	relative to 5862 nm.		relative to 5862 nm.		relative to 5862 nm.	
(°C)	relative to 5862 nm. 62 % w/w	(°C)	relative to 5862 nm. 65 % w/w	(°C)	relative to 5862 nm. Solubility	stdev
(°C)	relative to 5862 nm. 62 % w/w	(°C)	relative to 5862 nm. 65 % w/w -8.489	(°C) 31.09	relative to 5862 nm. Solubility	stdev 0.169
(°C) 64.65 64.65	relative to 5862 nm. 62 % w/w -8.398 -8.617	(°C) 67.35 67.35	relative to 5862 nm. 65 % w/w -8.489 -8.561	(°C) 31.09 36.07	relative to 5862 nm. Solubility -0.977 -2.043	0.169 0.202
(°C) 64.65 64.65 63.91	relative to 5862 nm. 62 % w/w -8.398 -8.617 -8.396	(°C) 67.35 67.35 66.82	relative to 5862 nm. 65 % w/w -8.489 -8.561 -8.368	(°C) 31.09 36.07 40.99	relative to 5862 nm. Solubility -0.977 -2.043 -2.794	0.169 0.202 0.170
64.65 64.65 63.91 63.31	relative to 5862 nm. 62 % w/w -8.398 -8.617 -8.396 -8.330	(°C) 67.35 67.35 66.82 66.82	relative to 5862 nm. 65 % w/w -8.489 -8.561 -8.368 -8.415	(°C) 31.09 36.07 40.99 45.88	relative to 5862 nm. Solubility -0.977 -2.043 -2.794 -3.838	0.169 0.202 0.170 0.239
64.65 64.65 63.91 63.31 62.63 61.95 60.75	relative to 5862 nm. 62 % w/w -8.398 -8.617 -8.396 -8.330 -8.047 -7.995 -7.905	(°C) 67.35 67.35 66.82 66.82 65.27 64.65 63.91	relative to 5862 nm. 65 % w/w -8.489 -8.561 -8.368 -8.415 -8.477 -7.981 -7.617	(°C) 31.09 36.07 40.99 45.88 50.73 55.57 60.53	relative to 5862 nm. Solubility -0.977 -2.043 -2.794 -3.838 -4.749 -5.529 -6.688	0.169 0.202 0.170 0.239 0.209 0.223 0.228
64.65 64.65 63.91 63.31 62.63 61.95 60.75 60.13	relative to 5862 nm. 62 % w/w -8.398 -8.617 -8.396 -8.330 -8.047 -7.995 -7.905 -7.179	(°C) 67.35 67.35 66.82 66.82 65.27 64.65 63.91 62.63	relative to 5862 nm. 65 % w/w -8.489 -8.561 -8.368 -8.415 -8.477 -7.981	(°C) 31.09 36.07 40.99 45.88 50.73 55.57	relative to 5862 nm. Solubility -0.977 -2.043 -2.794 -3.838 -4.749 -5.529	0.169 0.202 0.170 0.239 0.209 0.223
64.65 64.65 63.91 63.31 62.63 61.95 60.75 60.13 59.00	relative to 5862 nm. 62 % w/w -8.398 -8.617 -8.396 -8.330 -8.047 -7.995 -7.905 -7.179 -7.213	67.35 67.35 66.82 66.82 65.27 64.65 63.91 62.63 61.95	relative to 5862 nm. 65 % w/w -8.489 -8.561 -8.368 -8.415 -8.477 -7.981 -7.617 -7.243 -7.372	(°C) 31.09 36.07 40.99 45.88 50.73 55.57 60.53	relative to 5862 nm. Solubility -0.977 -2.043 -2.794 -3.838 -4.749 -5.529 -6.688	0.169 0.202 0.170 0.239 0.209 0.223 0.228
64.65 64.65 63.91 63.31 62.63 61.95 60.75 60.13 59.00 58.32	relative to 5862 nm. 62 % w/w -8.398 -8.617 -8.396 -8.330 -8.047 -7.995 -7.179 -7.213 -6.801	(°C) 67.35 67.35 66.82 66.82 65.27 64.65 63.91 62.63	relative to 5862 nm. 65 % w/w -8.489 -8.561 -8.368 -8.415 -8.477 -7.981 -7.617 -7.243	(°C) 31.09 36.07 40.99 45.88 50.73 55.57 60.53	relative to 5862 nm. Solubility -0.977 -2.043 -2.794 -3.838 -4.749 -5.529 -6.688	0.169 0.202 0.170 0.239 0.209 0.223 0.228
64.65 64.65 63.91 63.31 62.63 61.95 60.75 60.13 59.00 58.32 57.18	relative to 5862 nm. 62 % w/w -8.398 -8.617 -8.396 -8.330 -8.047 -7.995 -7.905 -7.179 -7.213 -6.801 -6.181	67.35 67.35 66.82 66.82 65.27 64.65 63.91 62.63 61.95	relative to 5862 nm. 65 % w/w -8.489 -8.561 -8.368 -8.415 -8.477 -7.981 -7.617 -7.243 -7.372	(°C) 31.09 36.07 40.99 45.88 50.73 55.57 60.53	relative to 5862 nm. Solubility -0.977 -2.043 -2.794 -3.838 -4.749 -5.529 -6.688	0.169 0.202 0.170 0.239 0.209 0.223 0.228
64.65 64.65 63.91 63.31 62.63 61.95 60.75 60.13 59.00 58.32 57.18 56.10	relative to 5862 nm. 62 % w/w -8.398 -8.617 -8.396 -8.330 -8.047 -7.995 -7.905 -7.179 -7.213 -6.801 -6.181 -6.394	67.35 67.35 66.82 66.82 65.27 64.65 63.91 62.63 61.95	relative to 5862 nm. 65 % w/w -8.489 -8.561 -8.368 -8.415 -8.477 -7.981 -7.617 -7.243 -7.372	(°C) 31.09 36.07 40.99 45.88 50.73 55.57 60.53	relative to 5862 nm. Solubility -0.977 -2.043 -2.794 -3.838 -4.749 -5.529 -6.688	0.169 0.202 0.170 0.239 0.209 0.223 0.228
64.65 64.65 63.91 63.31 62.63 61.95 60.75 60.13 59.00 58.32 57.18 56.10 55.48	relative to 5862 nm. 62 % w/w -8.398 -8.617 -8.396 -8.330 -8.047 -7.995 -7.905 -7.179 -7.213 -6.801 -6.181 -6.394 -6.249	67.35 67.35 66.82 66.82 65.27 64.65 63.91 62.63 61.95	relative to 5862 nm. 65 % w/w -8.489 -8.561 -8.368 -8.415 -8.477 -7.981 -7.617 -7.243 -7.372	(°C) 31.09 36.07 40.99 45.88 50.73 55.57 60.53	relative to 5862 nm. Solubility -0.977 -2.043 -2.794 -3.838 -4.749 -5.529 -6.688	0.169 0.202 0.170 0.239 0.209 0.223 0.228
64.65 64.65 63.91 63.31 62.63 61.95 60.75 60.13 59.00 58.32 57.18 56.10 55.48 54.46	relative to 5862 nm. 62 % w/w -8.398 -8.617 -8.396 -8.330 -8.047 -7.995 -7.905 -7.179 -7.213 -6.801 -6.181 -6.394 -6.249 -5.699	67.35 67.35 66.82 66.82 65.27 64.65 63.91 62.63 61.95	relative to 5862 nm. 65 % w/w -8.489 -8.561 -8.368 -8.415 -8.477 -7.981 -7.617 -7.243 -7.372	(°C) 31.09 36.07 40.99 45.88 50.73 55.57 60.53	relative to 5862 nm. Solubility -0.977 -2.043 -2.794 -3.838 -4.749 -5.529 -6.688	0.169 0.202 0.170 0.239 0.209 0.223 0.228
64.65 64.65 63.91 63.31 62.63 61.95 60.75 60.13 59.00 58.32 57.18 56.10 55.48	relative to 5862 nm. 62 % w/w -8.398 -8.617 -8.396 -8.330 -8.047 -7.995 -7.905 -7.179 -7.213 -6.801 -6.181 -6.394 -6.249	67.35 67.35 66.82 66.82 65.27 64.65 63.91 62.63 61.95	relative to 5862 nm. 65 % w/w -8.489 -8.561 -8.368 -8.415 -8.477 -7.981 -7.617 -7.243 -7.372	(°C) 31.09 36.07 40.99 45.88 50.73 55.57 60.53	relative to 5862 nm. Solubility -0.977 -2.043 -2.794 -3.838 -4.749 -5.529 -6.688	0.169 0.202 0.170 0.239 0.209 0.223 0.228

Table A14 Data for Figure 4.11

Temperature (°C)	Peak shift relative to 6996 nm. 50 % w/w	Temperature (°C)	Peak shift relative to 6996 nm. 54 % w/w	Temperature (°C)	Peak shift relative to 6996 nm. 58 % w/w	
35.55	-1.151	45.58	6.328	55.48	9.552	•
35.55	3.566	45.58	5.331	55.48	7.308	
35.55	1.166	45.17	6.405	54.89	8.231	
35.20	6.267	44.72	2.868	54.46	7.141	
34.79	1.903	44.32	5.754	53.89	8.816	
34.02	1.086	43.82	7.244	53.41	9.692	
33.66	3.527	42.98	7.188	52.40	7.168	
32.86	0.290	42.51	2.859	51.86	6.497	
32.51	2.845	41.65	1.680	50.82	5.362	
		41.29	6.264	50.33	6.958	
		40.38	2.811	49.36	6.468	
		40.01	3.072	48.42	5.502	
		39.18	1.297	47.91	5.693	
		38.38	0.036	46.96	4.811	
	Peak shift		Peak shift		Peak shift	
	I Our Jillic		reak siiiit		reak siilit	
	relative to		relative to		relative to	
Temperature		Temperature		Temperature		Solubility
Temperature (°C)	relative to	Temperature (°C)	relative to	Temperature (°C)	relative to	Solubility stdev
•	relative to 6996 nm.	•	relative to 6996 nm.	•	relative to 6996 nm.	•
(°C)	relative to 6996 nm. 62 % w/w	(°C)	relative to 6996 nm. 65 % w/w	(°C)	relative to 6996 nm. Solubility	stdev
(°C)	relative to 6996 nm. 62 % w/w	(°C) 67.35	relative to 6996 nm. 65 % w/w	(°C)	relative to 6996 nm. Solubility	1.9211
(°C) 64.65 64.65	relative to 6996 nm. 62 % w/w 11.394 11.345	(°C) 67.35 67.35	relative to 6996 nm. 65 % w/w 12.417 12.668	(°C) 31.09 36.07	relative to 6996 nm. Solubility 1.335 2.425	1.9211 1.0928
(°C) 64.65 64.65 63.91	relative to 6996 nm. 62 % w/w 11.394 11.345 12.179	(°C) 67.35 67.35 66.82	relative to 6996 nm. 65 % w/w 12.417 12.668 13.988	(°C) 31.09 36.07 40.99	relative to 6996 nm. Solubility 1.335 2.425 4.618	1.9211 1.0928 1.2584
64.65 64.65 63.91 63.31	relative to 6996 nm. 62 % w/w 11.394 11.345 12.179 11.454	(°C) 67.35 67.35 66.82 66.82	relative to 6996 nm. 65 % w/w 12.417 12.668 13.988 13.071	(°C) 31.09 36.07 40.99 45.88	relative to 6996 nm. Solubility 1.335 2.425 4.618 5.289	1.9211 1.0928 1.2584 1.2916
64.65 64.65 63.91 63.31 62.63	relative to 6996 nm. 62 % w/w 11.394 11.345 12.179 11.454 11.045	(°C) 67.35 67.35 66.82 66.82 65.27	relative to 6996 nm. 65 % w/w 12.417 12.668 13.988 13.071 12.056	(°C) 31.09 36.07 40.99 45.88 50.73	relative to 6996 nm. Solubility 1.335 2.425 4.618 5.289 7.644	1.9211 1.0928 1.2584 1.2916 1.56
64.65 64.65 63.91 63.31 62.63 61.95	relative to 6996 nm. 62 % w/w 11.394 11.345 12.179 11.454 11.045 10.350	(°C) 67.35 67.35 66.82 66.82 65.27 64.65	relative to 6996 nm. 65 % w/w 12.417 12.668 13.988 13.071 12.056 12.310	(°C) 31.09 36.07 40.99 45.88 50.73 55.57	1.335 2.425 4.618 5.289 7.644 8.506	1.9211 1.0928 1.2584 1.2916 1.56 1.2934
64.65 64.65 63.91 63.31 62.63 61.95 60.75	relative to 6996 nm. 62 % w/w 11.394 11.345 12.179 11.454 11.045 10.350 10.703	67.35 67.35 66.82 66.82 65.27 64.65 63.91	relative to 6996 nm. 65 % w/w 12.417 12.668 13.988 13.071 12.056 12.310 9.703	(°C) 31.09 36.07 40.99 45.88 50.73 55.57 60.53	relative to 6996 nm. Solubility 1.335 2.425 4.618 5.289 7.644 8.506 10.167	1.9211 1.0928 1.2584 1.2916 1.56 1.2934 1.2655
64.65 64.65 63.91 63.31 62.63 61.95 60.75 60.13 59.00 58.32	relative to 6996 nm. 62 % w/w 11.394 11.345 12.179 11.454 11.045 10.350 10.703 10.673 9.926 10.654	67.35 67.35 66.82 66.82 65.27 64.65 63.91 62.63	relative to 6996 nm. 65 % w/w 12.417 12.668 13.988 13.071 12.056 12.310 9.703 9.761	(°C) 31.09 36.07 40.99 45.88 50.73 55.57 60.53	relative to 6996 nm. Solubility 1.335 2.425 4.618 5.289 7.644 8.506 10.167	1.9211 1.0928 1.2584 1.2916 1.56 1.2934 1.2655
64.65 64.65 63.91 63.31 62.63 61.95 60.75 60.13 59.00 58.32 57.18	relative to 6996 nm. 62 % w/w 11.394 11.345 12.179 11.454 11.045 10.350 10.703 10.673 9.926 10.654 9.074	(°C) 67.35 67.35 66.82 66.82 65.27 64.65 63.91 62.63 61.95	relative to 6996 nm. 65 % w/w 12.417 12.668 13.988 13.071 12.056 12.310 9.703 9.761 12.237	(°C) 31.09 36.07 40.99 45.88 50.73 55.57 60.53	relative to 6996 nm. Solubility 1.335 2.425 4.618 5.289 7.644 8.506 10.167	1.9211 1.0928 1.2584 1.2916 1.56 1.2934 1.2655
64.65 64.65 63.91 63.31 62.63 61.95 60.75 60.13 59.00 58.32 57.18 56.10	relative to 6996 nm. 62 % w/w 11.394 11.345 12.179 11.454 11.045 10.350 10.703 10.673 9.926 10.654 9.074 7.857	(°C) 67.35 67.35 66.82 66.82 65.27 64.65 63.91 62.63 61.95	relative to 6996 nm. 65 % w/w 12.417 12.668 13.988 13.071 12.056 12.310 9.703 9.761 12.237	(°C) 31.09 36.07 40.99 45.88 50.73 55.57 60.53	relative to 6996 nm. Solubility 1.335 2.425 4.618 5.289 7.644 8.506 10.167	1.9211 1.0928 1.2584 1.2916 1.56 1.2934 1.2655
64.65 64.65 63.91 63.31 62.63 61.95 60.75 60.13 59.00 58.32 57.18 56.10 55.48	relative to 6996 nm. 62 % w/w 11.394 11.345 12.179 11.454 11.045 10.350 10.703 10.673 9.926 10.654 9.074 7.857 8.644	(°C) 67.35 67.35 66.82 66.82 65.27 64.65 63.91 62.63 61.95	relative to 6996 nm. 65 % w/w 12.417 12.668 13.988 13.071 12.056 12.310 9.703 9.761 12.237	(°C) 31.09 36.07 40.99 45.88 50.73 55.57 60.53	relative to 6996 nm. Solubility 1.335 2.425 4.618 5.289 7.644 8.506 10.167	1.9211 1.0928 1.2584 1.2916 1.56 1.2934 1.2655
64.65 64.65 63.91 63.31 62.63 61.95 60.75 60.13 59.00 58.32 57.18 56.10 55.48 54.46	relative to 6996 nm. 62 % w/w 11.394 11.345 12.179 11.454 11.045 10.350 10.703 10.673 9.926 10.654 9.074 7.857 8.644 7.821	(°C) 67.35 67.35 66.82 66.82 65.27 64.65 63.91 62.63 61.95	relative to 6996 nm. 65 % w/w 12.417 12.668 13.988 13.071 12.056 12.310 9.703 9.761 12.237	(°C) 31.09 36.07 40.99 45.88 50.73 55.57 60.53	relative to 6996 nm. Solubility 1.335 2.425 4.618 5.289 7.644 8.506 10.167	1.9211 1.0928 1.2584 1.2916 1.56 1.2934 1.2655
64.65 64.65 63.91 63.31 62.63 61.95 60.75 60.13 59.00 58.32 57.18 56.10 55.48	relative to 6996 nm. 62 % w/w 11.394 11.345 12.179 11.454 11.045 10.350 10.703 10.673 9.926 10.654 9.074 7.857 8.644	(°C) 67.35 67.35 66.82 66.82 65.27 64.65 63.91 62.63 61.95	relative to 6996 nm. 65 % w/w 12.417 12.668 13.988 13.071 12.056 12.310 9.703 9.761 12.237	(°C) 31.09 36.07 40.99 45.88 50.73 55.57 60.53	relative to 6996 nm. Solubility 1.335 2.425 4.618 5.289 7.644 8.506 10.167	1.9211 1.0928 1.2584 1.2916 1.56 1.2934 1.2655

Table A15 Data for Figure 4.12

Temperature (°C)	Peak shift relative to 6132 nm. 50 % w/w	Temperature (°C)	Peak shift relative to 6132 nm. 54 % w/w	Temperature (°C)	Peak shift relative to 6132 nm. 58 % w/w	
35.55	3.512	45.58	6.967	55.48	8.809	•
35.55	3.270	45.58	6.081	55.48	9.298	
35.55	3.474	45.17	6.719	54.89	8.744	
35.20	3.635	44.72	6.585	54.46	9.384	
34.79	3.208	44.32	6.328	53.89	8.879	
34.02	4.041	43.82	6.019	53.41	9.561	
33.66	3.417	42.98	6.549	52.40	8.947	
32.86	3.791	42.51	6.761	51.86	8.811	
32.51	4.005	41.65	6.757	50.82	9.127	
		41.29	6.761	50.33	9.322	
		40.38	6.696	49.36	9.013	
		40.01	6.841	48.42	8.825	
		39.18	6.416	47.91	9.564	
		38.38	7.409	46.96	9.219	
-	Peak shift		Peak shift		Peak shift	
	Peak shift relative to		Peak shift relative to		Peak shift relative to	
Temperature	relative to 6132 nm.	Temperature	relative to 6132 nm.	Temperature	relative to 6132 nm.	Solubility
Temperature (°C)	relative to	Temperature (°C)	relative to	Temperature (°C)	relative to	Solubility stdev
	relative to 6132 nm.		relative to 6132 nm.		relative to 6132 nm.	•
(°C)	relative to 6132 nm. 62 % w/w	(°C)	relative to 6132 nm. 65 % w/w	(°C)	relative to 6132 nm. Solubility	stdev
(°C) 64.65	relative to 6132 nm. 62 % w/w 10.544	(°C)	relative to 6132 nm. 65 % w/w 12.824	(°C)	relative to 6132 nm. Solubility	stdev 0.231
(°C) 64.65 64.65	relative to 6132 nm. 62 % w/w 10.544 10.705	(°C) 67.35 67.35	relative to 6132 nm. 65 % w/w 12.824 12.900	(°C) 31.09 36.07	relative to 6132 nm. Solubility 1.393 3.661	0.231 0.213
(°C) 64.65 64.65 63.91	relative to 6132 nm. 62 % w/w 10.544 10.705 10.863	(°C) 67.35 67.35 66.82	relative to 6132 nm. 65 % w/w 12.824 12.900 12.952	(°C) 31.09 36.07 40.99	relative to 6132 nm. Solubility 1.393 3.661 5.703	0.231 0.213 0.095
(°C) 64.65 64.65 63.91 63.31	relative to 6132 nm. 62 % w/w 10.544 10.705 10.863 10.920	(°C) 67.35 67.35 66.82 66.82	relative to 6132 nm. 65 % w/w 12.824 12.900 12.952 12.732	(°C) 31.09 36.07 40.99 45.88	1.393 3.661 5.703 7.477	0.231 0.213 0.095 0.224
(°C) 64.65 64.65 63.91 63.31 62.63	relative to 6132 nm. 62 % w/w 10.544 10.705 10.863 10.920 10.782	67.35 67.35 66.82 66.82 65.27	relative to 6132 nm. 65 % w/w 12.824 12.900 12.952 12.732 13.160	(°C) 31.09 36.07 40.99 45.88 50.73	relative to 6132 nm. Solubility 1.393 3.661 5.703 7.477 9.106	0.231 0.213 0.095 0.224 0.195
(°C) 64.65 64.65 63.91 63.31 62.63 61.95	relative to 6132 nm. 62 % w/w 10.544 10.705 10.863 10.920 10.782 11.048	67.35 67.35 66.82 66.82 65.27 64.65	relative to 6132 nm. 65 % w/w 12.824 12.900 12.952 12.732 13.160 12.741	(°C) 31.09 36.07 40.99 45.88 50.73 55.57	relative to 6132 nm. Solubility 1.393 3.661 5.703 7.477 9.106 10.655	0.231 0.213 0.095 0.224 0.195 0.233
(°C) 64.65 64.65 63.91 63.31 62.63 61.95 60.75 60.13 59.00	10.544 10.705 10.863 10.920 10.782 11.048 11.201 10.920 11.285	67.35 67.35 66.82 66.82 65.27 64.65 63.91	relative to 6132 nm. 65 % w/w 12.824 12.900 12.952 12.732 13.160 12.741 13.125	(°C) 31.09 36.07 40.99 45.88 50.73 55.57 60.53	1.393 3.661 5.703 7.477 9.106 10.655 11.975	0.231 0.213 0.095 0.224 0.195 0.233 0.170
(°C) 64.65 64.65 63.91 63.31 62.63 61.95 60.75 60.13 59.00 58.32	10.544 10.705 10.863 10.920 10.782 11.048 11.201 10.920	67.35 67.35 66.82 66.82 65.27 64.65 63.91 62.63	relative to 6132 nm. 65 % w/w 12.824 12.900 12.952 12.732 13.160 12.741 13.125 13.044	(°C) 31.09 36.07 40.99 45.88 50.73 55.57 60.53	1.393 3.661 5.703 7.477 9.106 10.655 11.975	0.231 0.213 0.095 0.224 0.195 0.233 0.170
(°C) 64.65 64.65 63.91 63.31 62.63 61.95 60.75 60.13 59.00 58.32 57.18	relative to 6132 nm. 62 % w/w 10.544 10.705 10.863 10.920 10.782 11.048 11.201 10.920 11.285 11.498 11.163	67.35 67.35 66.82 66.82 65.27 64.65 63.91 62.63 61.95	relative to 6132 nm. 65 % w/w 12.824 12.900 12.952 12.732 13.160 12.741 13.125 13.044 13.320	(°C) 31.09 36.07 40.99 45.88 50.73 55.57 60.53	1.393 3.661 5.703 7.477 9.106 10.655 11.975	0.231 0.213 0.095 0.224 0.195 0.233 0.170
(°C) 64.65 64.65 63.91 63.31 62.63 61.95 60.75 60.13 59.00 58.32 57.18 56.10	relative to 6132 nm. 62 % w/w 10.544 10.705 10.863 10.920 10.782 11.048 11.201 10.920 11.285 11.498 11.163 11.381	67.35 67.35 66.82 66.82 65.27 64.65 63.91 62.63 61.95	relative to 6132 nm. 65 % w/w 12.824 12.900 12.952 12.732 13.160 12.741 13.125 13.044 13.320	(°C) 31.09 36.07 40.99 45.88 50.73 55.57 60.53	1.393 3.661 5.703 7.477 9.106 10.655 11.975	0.231 0.213 0.095 0.224 0.195 0.233 0.170
(°C) 64.65 64.65 63.91 63.31 62.63 61.95 60.75 60.13 59.00 58.32 57.18	relative to 6132 nm. 62 % w/w 10.544 10.705 10.863 10.920 10.782 11.048 11.201 10.920 11.285 11.498 11.163	67.35 67.35 66.82 66.82 65.27 64.65 63.91 62.63 61.95	relative to 6132 nm. 65 % w/w 12.824 12.900 12.952 12.732 13.160 12.741 13.125 13.044 13.320	(°C) 31.09 36.07 40.99 45.88 50.73 55.57 60.53	1.393 3.661 5.703 7.477 9.106 10.655 11.975	0.231 0.213 0.095 0.224 0.195 0.233 0.170

Table A16 Data for Figure 4.13

Temperature (°C)	Peak shift relative to 8116 nm. 50 % w/w	Temperature (°C)	Peak shift relative to 8116 nm. 54 % w/w	Temperature (°C)	Peak shift relative to 8116 nm. 58 % w/w	
35.55	6.819	45.58	20.491	55.48	38.830	•
35.55	4.485	45.58	19.741	55.48	38.320	
35.55	5.930	45.17	22.158	54.89	37.229	
35.20	3.135	44.72	19.635	54.46	39.925	
34.79	5.184	44.32	20.274	53.89	39.178	
34.02	6.295	43.82	18.960	53.41	36.583	
33.66	4.825	42.98	20.863	52.40	38.129	
32.86	4.792	42.51	19.793	51.86	35.421	
32.51	5.742	41.65	18.537	50.82	34.888	
		41.29	18.327	50.33	32.548	
		40.38	15.997	49.36	34.933	
		40.01	16.935	48.42	34.745	
		39.18	16.618	47.91	35.662	
		38.38	17.829	46.96	31.451	
	Peak shift		Peak shift		Peak shift	
	relative to		relative to		relative to	
Temperature	8116 nm.	Temperature	8116 nm.	Temperature	relative to 8116 nm.	Solubility
Temperature (°C)		Temperature (°C)		Temperature (°C)	relative to	Solubility stdev
•	8116 nm.		8116 nm.		relative to 8116 nm.	•
(°C)	8116 nm. 62 % w/w	(°C)	8116 nm. 65 % w/w	(°C)	relative to 8116 nm. Solubility	stdev
(°C)	8116 nm. 62 % w/w 53.528	(°C) 67.35	8116 nm. 65 % w/w 69.036	(°C)	relative to 8116 nm. Solubility	1.136
(°C) 64.65 64.65	8116 nm. 62 % w/w 53.528 56.172	(°C) 67.35 67.35	8116 nm. 65 % w/w 69.036 68.751	(°C) 31.09 36.07	relative to 8116 nm. Solubility 1.131 7.816	1.136 1.636
(°C) 64.65 64.65 63.91	8116 nm. 62 % w/w 53.528 56.172 56.863	(°C) 67.35 67.35 66.82	8116 nm. 65 % w/w 69.036 68.751 67.874	(°C) 31.09 36.07 40.99	relative to 8116 nm. Solubility 1.131 7.816 17.108	1.136 1.636 1.437
(°C) 64.65 64.65 63.91 63.31 62.63 61.95	8116 nm. 62 % w/w 53.528 56.172 56.863 56.867 59.180 54.014	67.35 67.35 66.82 66.82 65.27 64.65	8116 nm. 65 % w/w 69.036 68.751 67.874 66.194 65.671 67.824	(°C) 31.09 36.07 40.99 45.88 50.73 55.57	1.131 7.816 17.108 26.476	1.136 1.636 1.437 1.253
64.65 64.65 63.91 63.31 62.63 61.95 60.75	8116 nm. 62 % w/w 53.528 56.172 56.863 56.867 59.180 54.014 54.919	67.35 67.35 66.82 66.82 65.27 64.65 63.91	8116 nm. 65 % w/w 69.036 68.751 67.874 66.194 65.671	(°C) 31.09 36.07 40.99 45.88 50.73	relative to 8116 nm. Solubility 1.131 7.816 17.108 26.476 35.933	1.136 1.636 1.437 1.253 1.640
64.65 64.65 63.91 63.31 62.63 61.95 60.75 60.13	8116 nm. 62 % w/w 53.528 56.172 56.863 56.867 59.180 54.014 54.919 53.250	67.35 67.35 66.82 66.82 65.27 64.65 63.91 62.63	8116 nm. 65 % w/w 69.036 68.751 67.874 66.194 65.671 67.824 66.519 67.325	(°C) 31.09 36.07 40.99 45.88 50.73 55.57	1.131 7.816 17.108 26.476 35.933 46.750	1.136 1.636 1.437 1.253 1.640 1.564
(°C) 64.65 64.65 63.91 63.31 62.63 61.95 60.75 60.13 59.00	8116 nm. 62 % w/w 53.528 56.172 56.863 56.867 59.180 54.014 54.919 53.250 53.760	(°C) 67.35 67.35 66.82 66.82 65.27 64.65 63.91 62.63 61.95	8116 nm. 65 % w/w 69.036 68.751 67.874 66.194 65.671 67.824 66.519 67.325 67.160	31.09 36.07 40.99 45.88 50.73 55.57 60.53	relative to 8116 nm. Solubility 1.131 7.816 17.108 26.476 35.933 46.750 58.742	1.136 1.636 1.437 1.253 1.640 1.564 1.904
(°C) 64.65 64.65 63.91 63.31 62.63 61.95 60.75 60.13 59.00 58.32	53.528 56.172 56.863 56.867 59.180 54.014 54.919 53.250 53.760 49.954	67.35 67.35 66.82 66.82 65.27 64.65 63.91 62.63	8116 nm. 65 % w/w 69.036 68.751 67.874 66.194 65.671 67.824 66.519 67.325	31.09 36.07 40.99 45.88 50.73 55.57 60.53	relative to 8116 nm. Solubility 1.131 7.816 17.108 26.476 35.933 46.750 58.742	1.136 1.636 1.437 1.253 1.640 1.564 1.904
(°C) 64.65 64.65 63.91 63.31 62.63 61.95 60.75 60.13 59.00 58.32 57.18	8116 nm. 62 % w/w 53.528 56.172 56.863 56.867 59.180 54.014 54.919 53.250 53.760 49.954 51.815	(°C) 67.35 67.35 66.82 66.82 65.27 64.65 63.91 62.63 61.95	8116 nm. 65 % w/w 69.036 68.751 67.874 66.194 65.671 67.824 66.519 67.325 67.160	31.09 36.07 40.99 45.88 50.73 55.57 60.53	relative to 8116 nm. Solubility 1.131 7.816 17.108 26.476 35.933 46.750 58.742	1.136 1.636 1.437 1.253 1.640 1.564 1.904
(°C) 64.65 64.65 63.91 63.31 62.63 61.95 60.75 60.13 59.00 58.32 57.18 56.10	8116 nm. 62 % w/w 53.528 56.172 56.863 56.867 59.180 54.014 54.919 53.250 53.760 49.954 51.815 50.560	(°C) 67.35 67.35 66.82 66.82 65.27 64.65 63.91 62.63 61.95	8116 nm. 65 % w/w 69.036 68.751 67.874 66.194 65.671 67.824 66.519 67.325 67.160	31.09 36.07 40.99 45.88 50.73 55.57 60.53	relative to 8116 nm. Solubility 1.131 7.816 17.108 26.476 35.933 46.750 58.742	1.136 1.636 1.437 1.253 1.640 1.564 1.904
(°C) 64.65 64.65 63.91 63.31 62.63 61.95 60.75 60.13 59.00 58.32 57.18 56.10 55.48	8116 nm. 62 % w/w 53.528 56.172 56.863 56.867 59.180 54.014 54.919 53.250 53.760 49.954 51.815 50.560 49.358	(°C) 67.35 67.35 66.82 66.82 65.27 64.65 63.91 62.63 61.95	8116 nm. 65 % w/w 69.036 68.751 67.874 66.194 65.671 67.824 66.519 67.325 67.160	31.09 36.07 40.99 45.88 50.73 55.57 60.53	relative to 8116 nm. Solubility 1.131 7.816 17.108 26.476 35.933 46.750 58.742	1.136 1.636 1.437 1.253 1.640 1.564 1.904
(°C) 64.65 64.65 63.91 63.31 62.63 61.95 60.75 60.13 59.00 58.32 57.18 56.10 55.48 54.46	8116 nm. 62 % w/w 53.528 56.172 56.863 56.867 59.180 54.014 54.919 53.250 53.760 49.954 51.815 50.560 49.358 49.290	(°C) 67.35 67.35 66.82 66.82 65.27 64.65 63.91 62.63 61.95	8116 nm. 65 % w/w 69.036 68.751 67.874 66.194 65.671 67.824 66.519 67.325 67.160	31.09 36.07 40.99 45.88 50.73 55.57 60.53	relative to 8116 nm. Solubility 1.131 7.816 17.108 26.476 35.933 46.750 58.742	1.136 1.636 1.437 1.253 1.640 1.564 1.904
(°C) 64.65 64.65 63.91 63.31 62.63 61.95 60.75 60.13 59.00 58.32 57.18 56.10 55.48	8116 nm. 62 % w/w 53.528 56.172 56.863 56.867 59.180 54.014 54.919 53.250 53.760 49.954 51.815 50.560 49.358	(°C) 67.35 67.35 66.82 66.82 65.27 64.65 63.91 62.63 61.95	8116 nm. 65 % w/w 69.036 68.751 67.874 66.194 65.671 67.824 66.519 67.325 67.160	31.09 36.07 40.99 45.88 50.73 55.57 60.53	relative to 8116 nm. Solubility 1.131 7.816 17.108 26.476 35.933 46.750 58.742	1.136 1.636 1.437 1.253 1.640 1.564 1.904

Table A17 Data for Figure 4.17

Temperature (°C)	Peak shift relative to 3188 nm. 50 % w/w	Temperature (°C)	Peak shift relative to 3188 nm. 53 % w/w	Temperature (°C)	Peak shift relative to 3188 nm. 56 % w/w
35.55	5.395	42.98	26.090	50.33	39.107
35.55	8.497	42.10	26.010	48.42	42.479
34.02	8.100	40.38	33.027	45.58	42.938
32.51	9.511	37.53	24.272	43.44	40.883
Temperature	Peak shift relative to 3188 nm. 59 % w/w	Temperature	Peak shift relative to 3188 nm. 62 % w/w	Temperature	Peak shift relative to 3188 nm. 65 % w/w
(0)	39 % W/W	(°C)	02 /0 W/W	(0)	UJ /6 W/W
57.75	60.487	64.65	75.847	67.35	91.172
. ,		1 ' '			
57.75	60.487	64.65	75.847	67.35	91.172

Peak shift relative to Temperature 3188 nm. Solubility (°C) Solubility stdev 31.09 1.148 1.361 36.07 17.060 1.901 40.99 32.854 1.604 45.88 47,478 0.577 50.73 60.335 0.954 70.284 0.990 55.57 60.53 82.058 0.212 65.43 92.158 1.026

Table A18 Data for Figure 4.18

Concentration (% w/w)	at solubility	Temperature (°C) at solubility from Figure 4.13.	at solubility	at solubility
50	35.56	34.02	33.10	34.30
54	43.30	42.06	40.60	41.20
58	50.93	50.10	48.90	48.99
62	57.94	57.42	57.93	56.28
65	64.74	64.84	65.25	63.56

Average Temperature (°C)	Temperature (°C) stdev		
34.25	1.02		
41.79	1.17		
49.73	0.97		
57.39	0.78		
64.60	0.73		

THE PERSON NAMED IN COLUMN TWO IS NOT THE PERSON NAMED IN COLUMN TWO IS NAM

Table A19 Data for Figure 5.4

	TIR	l	
	Supersaturation		TIR
Temperature (°C)	profile.	Temperature (°C)	
		35.30	2.869
40.56	3.088		2.509
40.38	3.093	30.26	
39.39	3.074	25.17	2.229
38.22 37.10	3.078 3.090	20.05 15.01	1.956 1.738
37.10 35.78	3.096	9.92	1.738
34.04	3.069	9.92	1.400
32.22	3.070		
31.47	3.061		
32.32	2.982		
32.95	2.891		
33.07	2.840		
32.93	2.790		
32.71	2.763		
32.20	2.699		
31.82	2.655		
31.56	2.648		
31.25	2.604		
30.77	2.552		
30.56	2.524		
30.46	2.537		
30.40	2.500		
30.35	2.503		
30.33	2.509		
30.32	2.487		
30.32	2.495		
30.31	2.528		
30.31	2.525		
30.31	2.523		
30.00	2.498		
28.86	2.435		
27.74	2.378		
26.79	2.311		
25.89	2.251		
24.55	2.191		
22.88	2.103		
22.00	2.047		
21.06	2.004		
20.43	1.958		
19.17	1.892		
18.20	1.852		
17.17	1.814	·	
16.15	1.774		
15.50	1.720		
14.57	1.682		
13.32	1.628		
12.18	1.595		
10.47	1.498		

MICHIGAN STATE UNIV. LI 312930140563